Technical University of Munich
TUM School of Engineering and Design

Numerical Investigation of Stator Hub Configurations in Multi-Stage Axial Flow Compressors

Ilaria De Dominicis

Vollständiger Abdruck der von der TUM School of Engineering and Design der Technischen Universität München zur Erlangung des akademischen Grades einer

Doktorin der Ingenieurwissenschaften (Dr.-Ing.)

genehmigten Dissertation.

Vorsitz:	Prof. Dr. phil. Ilkay Yavrucuk
Prüfer der Dissertation:	1. Prof. Dr.-Ing. Volker Gümmer 2. Prof. Dr.-Ing. habil. Ronald Mailach

Die Dissertation wurde am 21.03.2024 bei der Technischen Universität München eingereicht und durch die TUM School of Engineering and Design am 08.10.2024 angenommen.

Dedicated to my family.

Abstract

Keywords: axial compressor design, hub leakage flows, aerodynamic losses

Choosing the stator hub design is one of the most important decisions in the early design phase of an axial compressor. Two different designs have been successfully employed over the last decades: cantilevered and shrouded. They strongly affect the flow field and produce losses in different ways. In this study, a thoughtful analysis of the impact of the stator hub configurations on the aerodynamic performance for two different multi-stage subsonic axial compressors is carried out: a 4-stage low-speed and a 5.5-stage high-speed one. Both compressors have been studied when equipped with both cantilevered and shrouded vanes. The two main goals are to better understand the impact of the stator hub architecture in a multi-stage axial configuration and indicate how to achieve an optimum machine featuring shrouded stators.

For the 4-stage low-speed compressor, for which experimental data was already available, the analysis focused on the stage matching and aerodynamic loss generation and propagation when the third stator hub configuration was locally changed from cantilevered to shrouded. The results showed, that when the design of the fourth rotor is kept unchanged and not tailored to the exit flow of the upstream stator, the impact of the third stator hub configuration on the aerodynamic performance is drastically high for the downstream fourth rotor and unexpectedly low for the downstream fourth stator.

For the 5.5-stage high-speed compressor, the design of the first four stators was changed from cantilevered to shrouded. For both configurations, first the regions of higher losses and the stall mechanisms were investigated. Then a sensitivity analysis was performed on a reduced model to assess how the losses depend on some selected design parameters: clearances, degree of reaction, and stator hub camber line style in the hub region. The results of the sensitivity study were used to design two improved configurations featuring shrouded stators: one with a greater stall margin and one with reduced sensitivity to radial clearances. Additionally, generic recommendations were derived, that designers can use to identify an optimum configuration of a multi-stage axial compressor featuring shrouded stators.

Acknowledgments

I would like to express the most sincere gratitude to my supervisor Prof. Dr.-Ing. Volker Gümmer for offering me the opportunity to work on this engaging project and his constant support throughout the project.

I would like to thank Prof. Dr. phil. Ilkay Yavrucuk for chairing the thesis evaluation and Prof. Dr.-Ing. habil. Ronald Mailach for being the second examiner.

The PhD project would not have been possible without the financial support of Siemens Energy AG and the Bundesministerium für Wirtschaft und Technologie in the framework of AG Turbo. My sincere gratefulness goes to Dr.-Ing. Sebastian Robens and Dr.-Ing. Christian Cornelius for the guidance provided and the long hours of insightful talks about compressor aerodynamics. I really enjoyed working with you.

My appreciation extends to all colleagues at the Chair of Turbomachinery and Flight Propulsion of the TUM as well as the students that have contributed to the success of the project. In particular many thanks to Lucrezia Veggi, Dr.-Ing Nikolaos Perakis, Mattia Straccia, Samuele Giannini, Simona Rocchi, Robin Stiegele and Antonija Šimunović.

I would also like to express my appreciation to Dr.-Ing. Nina Wolfrum and Dr.-Ing. Sungho Yoon for the very insightful discussions during the past years. I am also grateful to my mentor, Prof. Dr.-Ing. Alberto Guardone, my former manager Dr.-Ing. Nadir Ince and my master thesis supervisor Prof. Dr.-Ing. Maurizio Quadrio. Their encouragements and advices have been invaluable, especially in the frustrating moments the course of a PhD program sometimes involves.

Finally, I would like to thank my family, in particular my husband Andrea and my parents, for having always been there to listen to me, to support me in every possible way and to help me to see the world from different perspectives. Many thanks also to my colleagues at MTU Aero Engines and my friends Floriana and Gabriel for their precious advices.

Content

List of Figures

List of Tables

List of symbols

Latin symbols

C	cantilevered configuration
c	chord
$\overrightarrow{c}$	absolute velocity
c_p	specific heat capacity at constant pressure
E	specific relative total energy, entire
e	specific internal energy density
$\hat{F}, \hat{G}, \hat{H}$	inviscid fluxes
$\hat{F}_\nu, \hat{G}_\nu, \hat{H}_\nu$	viscous fluxes
h	enthalpy
I	increased clearances
J	transformation Jacobian
k	turbulent kinetic energy
L	large clearances
m	parameter to define the camber line distribution
$\dot{m}$	mass flow
N	nominal clearances
n	grid number
$O1$	shrouded configuration with baseline degree of reaction and circular-arc stator near-endwall profile style, reduced model
$O2$	shrouded configuration with moderate increase of degree of reaction and circular-arc stator near-endwall profile style, reduced model
P_{ht}	power output
Pr_t	turbulent Prandtl number
p	pressure
$\hat{Q}$	solution vector
$\langle Q \rangle$	mean of Q
R	rotor, grid refinement factor, gas constant, reduced clearances, reduced model
r	radius
S	stator, shrouded configuration, Sutherland's constant

$\hat{S}$	source term
s	span
s_{ij}	fluctuating rate-of-strain tensor
T	temperature, time interval
t	time
u, v, w	Cartesian velocity components
$\overrightarrow{u}$	blade velocity
u_t	friction velocity
$V1$	aerofoil wake
$V2$	clearance vortex
$V3$	three-dimensional corner separation
v	velocity in a frame of reference fixed to the blade
$\overrightarrow{w}$	relative velocity
x, y, z	Cartesian axis
y^+	distance from the wall normalized by the viscous length scale

Greek symbols

α	absolute swirl angle
β	relative swirl angle
γ	specific heat ratio
δ	angle variation
δ_{ij}	Kronecker delta
ε	numerical error
ϵ	rate of dissipation of turbulent kinetic energy
ξ	loss coefficient
ξ, ν, ζ	curvilinear axis
η	isentropic efficiency
θ	circumferential coordinate
Λ	degree of reaction
μ	viscosity
ν	kinematic viscosity
ν_t	turbulent viscosity
π	absolute total pressure ratio

ρ	density
σ	solidity
τ	clearance
τ_w	wall shear stress
ω	angular speed, turbulent frequency

Subscripts

ax	axial
dyn	dynamic
in	inlet
is	isentropic
out	outlet
ref	reference
t	total

Superscripts

$\overline{}$	pitch-wise averaged value
$\bar{\ }$	Reynolds averaged
$\tilde{\ }$	Favre averaged
$'$	turbulent fluctuation

Abbreviation

CAM1	shrouded configuration with circular-arc stator near-endwall profile style and nominal clearances, reduced model
CAM2	shrouded configuration with moderately rear-loaded stator near-endwall profile style and nominal clearances, reduced model
CAM3	shrouded configuration with highly rear-loaded stator near-endwall profile style and nominal clearances, reduced model
CFD	computational fluid dynamics
CFL	Courant–Friedrichs–Lewy

CIR	cantilevered configuration with increased clearances, reduced model
CLE	cantilevered configuration with large clearances, entire model
CLR	cantilevered configuration with large clearances, reduced model
CNE	cantilevered configuration with nominal clearances, entire model
CNR	cantilevered configuration with nominal clearances, reduced model
CRE	cantilevered configuration with reduced clearances, entire model
CRR	cantilevered configuration with reduced clearances, reduced model
DF	diffusion factor
DLR	Deutsches Zentrum für Luft- und Raumfahrt (German Aerospace Center)
DOR1	shrouded configuration with large increase of degree of reaction and nominal clearances, reduced model
DOR2	shrouded configuration with moderate increase of degree of reaction and nominal clearances, reduced model
DOR3	shrouded configuration with reduced degree of reaction and nominal clearances, reduced model
DP	design point
EXP	experimental
GCI	grid convergence index
HALO	hydrostatic advanced low leakage seal
HSC	high-speed compressor
IGV	inlet guide vane
LE	leading edge
LSRC	low-speed research compressor
MS	midspan
NS	near-stall point
OGV	outlet guide vane

OPT1	shrouded configuration with baseline degree of reaction, circular-arc stator near-endwall profile style and with reduced clearances, reduced model
OPT2	shrouded configuration with moderate increase of degree of reaction, circular-arc stator near-endwall profile style and with reduced clearances, reduced model
PS	pressure side
RANS	Reynolds-averaged Navier-Stokes
SIE	shrouded configuration with increased clearances, entire model
SIR	shrouded configuration with increased clearances, reduced model
SLE	shrouded configuration with large clearances, entire model
SLR	shrouded configuration with large clearances, reduced model
SNE	shrouded configuration with nominal clearances, entire model
SNR	shrouded configuration with nominal clearances, reduced model
SRE	shrouded configuration with reduced clearances, entire model
SRR	shrouded configuration with reduced clearances, reduced model
SS	suction side
SST	shear stress transport
TE	trailing edge
TRACE	turbomachinery research aerodynamics computational environment
TS	towards-stall point: operational point located between the design point and the near-stall point

1 Introduction

Gas turbines play a major role in generating secure, affordable, and environmentally sustainable power. They are extensively used for a wide spectrum of applications, which include aircraft and ship propulsion, and electric power generation for land and offshore platforms. Gas turbines are able to match the specific requirements of efficiency, reliability, quick start-up, flexibility, and environmental compatibility for each of these applications.

The design of a gas turbine needs to take into account different engineering fields, such as aerodynamics, heat transfer, solid mechanics, vibration, system control, rotordynamics, and combustion. Over the last decades, the introduction of high speed computers and modern numerical methods of calculation have facilitated the improvement of the understanding of the flow physics underlying the gas turbines, thus allowing the design of more efficient gas turbines. One major advantage of numerical studies in comparison with experimental investigations is that they allow quick and cheap modifications of the geometry. The understanding of the flow phenomena in the compressors has been fundamental to obtaining a sufficiently high pressure ratio, which is of significant importance in the performance cycle and plays a major role as the temperature at the exit of the combustion chamber does.

As stated by Schobeiri [2], the major aerodynamic losses in a turbomachine are profile loss, secondary flow loss, exit loss, loss due to trailing edge thickness, and loss due to the trailing edge mixing in cooled gas turbine blades. Nowadays, one of the main challenges in compressor design is the reduction of the losses in the endwall regions, which are the most important but unfortunately the least well understood parts of compressor flow [3]. For the stator hub configuration, there are two endwall designs that have been used over the last years in industry: shrouded and cantilevered. Both configurations work efficiently, each having its merits and disadvantages depending on design requirements and choice of aerodynamic loading within the compressor. The aerodynamic characteristic of the machine is strongly affected by the stator hub configuration. The studies of the aerodynamic performance carried out by Jefferson and Turner [4], Freeman [5], Heidegger *et al.* [6], Swoboda *et al.* [7] and Yoon *et al.* [8] showed, that the effect of the stator hub configuration strongly depends on the flow details of the specific case, which may be determined by gas path geometry, blading style or even compressor physical size. The choice between shrouded and cantilevered stator hub configuration has to be made during the preliminary design of a compressor in order to set the mechanical arrangement within the overall component design process. Indeed, this choice is generally based on mechanical considerations [9]. Additional factors such as weight, life, and cost play a role in determining the stator hub configuration choice for a specific compressor design. A cost reduction of up to 12% for each stage can be gained by using cantilevered stators, as estimated by Campobasso *et al.* [10]. Beyond this, it may be required to implement cantilevered stators in one section of a compressor and shrouded stators in another adjacent section. A significant advantage of the shrouded stator is, that vibration problems can be more easily reduced or eliminated [3]. Furthermore, the performance of the shrouded configurations strongly depends on the seal used and, in recent years, different kinds of seal technology have been developed, such as the hydrostatic advanced low leakage (HALO) seals [11], which allow designers to strongly reduce the amount of leakage flow.

In the present study, two multi-stage subsonic axial compressors, a low-speed and a high-speed, were investigated. For both machines, a configuration with cantilevered stators and one featuring at least one shrouded stator were considered. Firstly, the effects of the two stator hub configurations on the aerodynamic performance, in terms of loss and efficiency, were deeply investigated using these two multi-stage arrangements. Additionally, for the high-speed compressor, a sensitivity analysis was performed to quantify the impact of selected geometric parameters, which are the clearance size, the degree of reaction, and the camber line style in the stator hub region. The results were used to design two enhanced shrouded configurations with improved aerodynamic performance compared to the original cantilevered configuration and to derive indications for axial compressor designers.

The structure of the work is the following: chapter 2 introduces the state-of-the-art of the stator hub designs. Chapter 3 deals with the numerical and experimental investigation of the low-speed research compressor (LSRC), aimed at analysing the impact of the stator hub flow leakage in a section of the machine featuring a change of stator hub configuration. Chapter 4 is entirely dedicated to the high-speed compressor (HSC). Firstly, the entire 5.5-stage model is numerically investigated by considering the baseline cantilevered configuration and two shrouded configurations, achieved by changing the stator hub design of the first four vanes. The two shrouded configurations differ because of the clearance level used for the stators. Successively, the best parameters of the machine are determined starting from a parametric analysis performed on a reduced model. The results of the parametric study are used to design two improved shrouded configurations and to provide recommendations for identifying the optimum design parameters of a multi-stage axial compressor. In conclusion, chapter 5 gives a summary and overview of the work.

The results presented in this work originated from a three-years research project of collaboration between Siemens Energy AG and the Department of Turbomachinery and Flight Propulsion of the Technische Universität München as part of the joint research Flexi Verdi in the framework of AG Turbo. The work was supported by the "Bundesministerium für Wirtschaft und Technologie".

2 Literature review

This chapter provides a review of the current understanding of the impact of the stator hub architecture on the aerodynamic performance of a multi-stage axial compressor. Firstly, the key role of the efficiency and the evaluation of the losses in turbomachinery are introduced. Then, the leakage flows associated with the two stator hub configurations, cantilevered and shrouded, and their state-of-art are reviewed. In conclusion, the motivation for the work is illustrated.

2.1 Losses in turbomachinery

Efficiency is one of the most important parameters for most turbomachines, in particular for gas turbine engines, since a small change in efficiency causes a large proportional change in power output and/or fuel burn. Increasing the efficiency of a turbomachine is extremely complex, as many factors play a role. The origin and effects of loss of efficiency in turbomachinery have been intensively studied over the last years. Denton [12] has highlighted the importance of focusing on the identification of the physical origin of the losses rather than using prediction methods. Indeed, nowadays the loss mechanisms in some regions of the machine, such as the endwall regions, are still not fully understood [3], and in practical applications the performance predictions are very often based on correlations, which are empirically tuned by each manufacturer to match the predictions of existing machines.

Over the last decades, different loss coefficients have been defined. They result in the same value if the relative Mach number is lower than 0.3 [12] and there are no moving endwalls relative to the aerofoil, i.e. the casing moves relative to the rotor and the hub moves relative to the stator. For a higher relative Mach number, or when the configuration includes rotating endwalls, the loss coefficients can be expected to show a different trend.

The loss coefficient based on the stagnation pressure, defined as:

$$\xi_{pressure} = \frac{(p_{t,in} - p_{t,out})}{(p_{t,in} - p_{in})}, \tag{2.1}$$

is probably the most conventional loss coefficient as well as the easiest to calculate. Despite that, the entropy change based loss coefficient is a more accurate loss coefficient for adiabatic machines. A change of isentropic efficiency can indeed be caused by both heat transfer across temperature differences and irreversible flow processes, such as viscous friction in the boundary layers of mixing processes, or non-equilibrium processes, e.g. shock waves. Since turbomachinery can be mostly approximated as adiabatic, the change of isentropic efficiency is directly proportional to the entropy generated by every irreversible process in the machine. The entropy change based loss coefficient is defined by Yoon *et al.* [8] as:

$$\xi_{entropy} = 1 - e^{-((c_p ln \frac{T_{t,out}}{T_{t,in}} - R ln \frac{p_{t,out}}{p_{t,in}})/R)}. \tag{2.2}$$

Since the entropy is independent of the reference system, the change of entropy for each row can be summed up to calculate the entropy change of the whole machine.

The choice of the most suitable loss coefficient is very important and, if inaccurate, may result in misleading conclusions as pointed out by Yoon *et al.* [8]. They numerically investigated, through detailed 3D Reynolds-Averaged Navier-Stokes (RANS) calculations, in which the rotating surfaces of the leakage path were fully resolved, a cantilevered and a shrouded stator vane with the same level of clearances by considering both the stagnation pressure based loss coefficient and the entropy change based loss coefficient. They observed that the two loss coefficients give opposite results, the cantilevered design being the one with reduced stagnation pressure loss, and the shrouded design being the one with lower entropy based losses. This is because the entropy change based loss coefficient includes the work input and takes into account the energy added by the rotating surfaces, which is different for the two stator hub configurations. The relative rotation between the stator and the hub imparts energy to the hub flow for the cantilevered stators, whereas the rotating inner leakage surface imparts energy to the seal cavity leakage flow for shrouded stators. When performing 3D RANS calculations, in which the leakage paths and the associated rotating surfaces are modelled, it is essential to take into account the different impact of the rotating surfaces for the two stator vane designs.

2.2 Stator hub designs

In the preliminary design of an axial compressor, one of the key decisions to be made is the stator hub architecture. In Figure 2.1, a schematic sketch of the two stator hub configurations is given. For the cantilevered stator hub configuration, shown in Figure 2.1(a), the vane tip is extended toward the hub while maintaining a reasonable gap between rotating and stationary parts. The leakage flow is driven by the circumferential pressure difference between the pressure side (PS) and the suction side (SS) of the stator vane, in the gap between the stationary vane and the rotating hub. For the shrouded design, shown in Figure 2.1(b), an inner shroud is attached to the stator vanes to ensure a better seal of this gap with a corresponding increase of aerodynamic efficiency. Due to increasing pressure in the axial direction, the leakage flow recirculates through the seal leakage path.

The cantilevered design normally requires an increased level of clearance or hub surface roughness in comparison to the shrouded stator design to prevent damages to the stator caused by the rotor spool [8]. For the cantilevered stator design there is indeed generally more concern, in terms of possibility to have contact between the stationary and the rotating part. The effect of having larger clearances or roughness

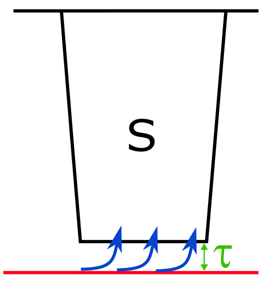

a) Cantilevered

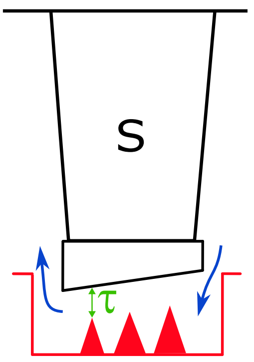

b) Shrouded

Figure 2.1: Stator hub configurations

is negative in terms of efficiency but, on the other hand, the cantilevered design allows smaller axial gaps between the rows. This has a positive impact on efficiency, as it reduces the wetted surface, allows shorter and lighter compressors, and may recover some of the wake region losses as demonstrated by Smith [13]. The shrouded design allows reduced radial clearances in comparison with the cantilevered one; however, additional leakage flow may occur in the circumferential segments. Further advantages for the shrouded design are that the pinned hub reduces the risk of vibrations, thereby allowing the aerofoils to be thinner than their cantilevered counterparts.

As the cantilevered stator vane is easier to manufacture, the cost is generally lower. Campobasso *et al.* [10] observed that the stage cost is reduced by circa 12% if cantilevered stators are used. For the shrouded design, not only the manufacturing costs per vane are increased, but also the weight and the radius of the stator vane.

Sealing technology

The kinds of sealing used for the shrouded design can be very different. Traditionally, labyrinth seals and flexible brush seals have been used in turbomachinery, whereas HALO seals are a more recent and innovative sealing technology.

The first studies on labyrinth seals, schematically shown in Figure 2.1(b), were conducted starting from the 1940s and 1950s. More recently, Denecke *et al.* [14] experimentally investigated the performance of labyrinth seals, concluding that they are inexpensive and robust against changes in the flow field [11]. The main disadvantage of labyrinth seals is the requirement for a certain gap between the seal and the rotating counter-part to prevent rubbing and structural damage. The gap can, therefore, not be chosen to be arbitrarily small, which limits its ability to reduce leakage. A possible solution is to apply comparably soft liners as the honeycombs, which not only reduces the damage caused by the rotating part during rubbing, but also the heat input [15].

A different kind of seal is the flexible brush seal. Flexible brush seals consist of a flexible bristle package placed between a backing plate and a front plate. They have the advantage of requiring only a very small gap between the bristle package and the rotor, thus allowing a reduced leakage mass flow. This small gap can be achieved without severe risk of detrimental deterioration in case of rubbing due to the radial flexibility of the bristles. Additional advantages are reduced weight, reduced axial mounting space [16], and improved rotor dynamic characteristics. The rubbing that is tolerated, however, increases the local heat in the rotor structure, which leads to wear and increases the drag torque. To reduce these negative effects, Delgrado *et al.* [17] and Andrés *et al.* [18] used a hybrid brush called "floating shoes".

In recent years, novel adaptive seal designs have been developed, called HALO seals, to reduce the leakage mass flow significantly, especially during part-load operations. Both axial and radial movements, triggered by the pressure ratio, can be achieved without any wear, ensuring superior seal performance for various operating conditions maintained over a long life-time [11].

2.3 State-of-the-art of the stator hub configurations

The effect of the stator hub configuration on aerodynamic performance has been the focus of many studies over the last decades. Jefferson and Turner [4], in 1958, conducted one of the fist studies, which highlighted the influence of the shroud leakage in multi-stage axial compressors. They experimentally investigated a six-stage compressor ring equipped with shrouded and cantilevered stator hub configurations. Their results showed that the shrouded configuration had lower efficiency and a reduced stall margin in comparison to the cantilevered one. However, the designs used for the stator and for the cavity are not representative of a typical design employed nowadays.

In the 80s, two important studies were published on this topic. In 1985, Freeman [5] pointed out that the optimum design depends on the ratio of clearance and flow area. His measurements led to the conclusion that, for a specific blading, the shrouded design has improved performance with respect to the cantilevered one if the leakage area is larger than 2.5 % of the flow area. Wisler [9], in 1988, observed that the aerodynamic performance of well-designed shrouded and cantilevered stators are comparable, and that the decision about the stator hub design has to be based on mechanical considerations rather than aerodynamic ones. Despite that, in the middle of the 90s, two major studies were conducted by Heidegger *et al.* [6] and Wellborn and Okiishi [19] to further analyse the effect of the two stator designs on the aerodynamic performance.

In the work of Heidegger *et al.* [6], the flow through an axial compressor inner banded stator seal cavity was numerically investigated when the seal cavity flow path and the main path were simulated simultaneously. One of the most significant discoveries made through this study was that the tangential velocity and the total temperature for the leakage flow through the seal cavity greatly increased. Due to the fact that the leakage flow exiting the cavity re-enters the main path, immediately upstream of the stator aerofoil leading edge, with a higher tangential velocity than the main flow, the flow incidence of the stator vane is larger close to the hub compared to the mid-span, causing a region of separate flow on the suction surface of the stator aerofoil near the hub. The authors observed that the injection of this high tangential-moment seal cavity leakage flow needs to be taken into account in the stator design [20]. Other interesting discoveries are linked to a better description of the flow structure inside the seal cavity, such as the vortices existing in both the seal cavity tranches connecting the main flow path and the cavity, driven by the main passage flow and the leakage flow. Additional findings are the fact, that the pitchwise distributions in the tranches are affected by the stator passage flow-field only in the -10% of the stator span, and the mixed positive and negative radial flows at the interface between the main path and the seal cavity. Indeed, although the majority of the fluid enters the seal cavity downstream of the stator vane and exits upstream, the regions of reverse flow were found both for the upstream and downstream openings. Upstream, they result from the potential field of the stator vane which forces mass flow downward into the seal cavity, whereas downstream, positive radial velocities were observed in the stator vane wake. The work included a parametric study of the stator seal cavity to quantify the impact of the seal tooth gap, the wheel speed, the cavity depth, the radial mismatch of the flow path, the axial trench gap, the hub corner treatment, and the stator land edge treatment. Among them, the size of the knife seal tooth gap was found to be the most sensitive parameter, whereas many of these other parameters had very little impact.

Similar results were achieved by Wellborn and Okiishi [19], who experimentally investigated the influence of the shrouded stator cavity flow on four stage low-speed axial flow compressor aerodynamics. They firstly modified all four stators of a multi-stage axial compressor to quantify the importance of the shrouded stator cavity flows on the performance the machine. Then they made alterations only to the third stage cavity flows while the other stages were kept at the baseline configuration. This allowed them to describe how shrouded stator cavity flow affects the aerodynamic performance of an embedded stage. Also, the flow-field within the shrouded stator cavity was investigated through detailed pressure and velocity distributions. They observed that although the gap size did not alter the stall margin, the increasing labyrinth seal-tooth leakage degraded compressor performance: an efficiency degradation of 1% and a penalty of 3% in the pressure rise was found for each percent increase in the seal clearance. In a multi-stage arrangement, overall performance is affected both directly and indirectly by the leakage flow; the stator row, in which the leakage occurred, is directly spoiled in the near-hub region by leakage flow, whereas the performance of the downstream stage is influenced by the altered inlet flow condition caused by the leakage flow in the upstream stator. Consequently, there is a compound effect caused by individual leakages occurring; the leakage flow and the loss distributions, as well as the stage matching, are altered and increasingly cause deviation from the design intent along the flowpath of a multi-stage compressor. The downstream rotor, in fact, does not tend to heal the maldistributed incoming flow near the hub, so the flow distribution into the next stator is also modified by providing a higher incidence near the hub. They emphasized that not only the stator row in which leakage occurs should be taken into account in the design phase of a multi-stage axial compressor, but also all the downstream blade rows should be considered. Furthermore, they observed that the flow within the cavity experiences spatial and temporal variations, some due to the upstream potential flow field influencing the next downstream blade row. In a different study, Wellborn and Okiishi [21] used numerical simulations to resolve details associated with the interaction between the primary and cavity flows. The results indicate that the fluid originating in the stator upstream cavity collects on the suction side when the cavity tangential momentum is low, but the fluid collects on the pressure side when it is high.

A higher stall margin but reduced work coefficient and efficiency resulted for the cantilevered build both in the studies conducted by Swoboda *et al.* [7] and Campobasso *et al.* [10], in which a multi-stage low-speed axial compressor, configured with both cantilevered and shrouded stators, was investigated. The experiments of Swoboda *et al.* [7] focused on the hub clearance vortex of the cantilevered build. They proved that the higher stall margin for the cantilevered configuration is caused by the hub clearance vortex, which removes separation regions on the hub, thus stabilizing the flow field because it acts against to the secondary flow in the passage. The stabilizing effect of the hub clearance vortex in the hub region reduces the stator losses for the cantilevered build. Campobasso *et al.* [10], by performing both numerical and experimental investigations, proved that a steady Navier-Stokes solver is able to predict correctly the local details of the flow field in a multi-stage arrangement. They stated, that the choice of the stator hub is mostly determined by mechanical and economic aspects rather than aerodynamics ones. Indeed engine direct operating and maintenance cost, as well as manufacturing cost of a shrouded stator stage can be up to 10% higher than for a cantilevered one.

For shrouded compressor stator vanes, the tangential velocity of the leakage flow within the seal cavity is determined by the combination of tangential momentum of the passage flow entering the seal cavity via the downstream trench and the relative motion of the rotating hub endwall. The influence of the tangential velocity of the shrouded cavity on aerodynamic performance was deeply investigated by Demargne and Longley [22] and Sohn *et al.* [23]. Both studies showed, that increasing the tangential velocity has the effect of increasing the overall efficiency. Demargne and Longley [22] studied the proprieties of the flow at the interface between the cavity and the main path in a linear cascade by independently varying the two main parameters controlling the interaction of shroud leakage and mainstream flows: leakage mass flow and tangential velocity. Also, they used separate upstream and downstream slots to simulate seal effects in a linear compressor cascade. They observed, that increasing the leakage mass flow rate has a detrimental effect on the aerodynamic performance, but increasing the cavity tangential velocity improves the performance of a stator row. The impact of increasing the leakage mass flow was expected, but the impact of increasing the tangential velocity highlighted new information. When the tangential velocity of the flow in the cavity is increased, the stator vane stagnation pressure loss decreases and the flow turning increases. At low cavity tangential velocity, the leakage flow tends to strengthen the hub endwall secondary flow and to increase the hub corner separation. As the tangential velocity approaches the wheel speed, the performance of the stator vane becomes largely insensitive to the amount of flow leaking from the shroud cavity and, for tangential velocity above the freestream values, the surplus tangential momentum of the leakage flow weakens the endwall secondary flows and reduces the hub corner stall. The effects of the change in cavity tangential velocity are not confined to the hub region, but affect the distribution of blockage, flow turning, and loss across the entire span. Sohn *et al.* [23] focused on the influence of the tangential velocity variation on the axial evolution of loss generated by the leakage flow in the shrouded cavity and the vane passage. Their results show, that increasing the tangential velocity of the leakage flow reduces loss by 10% to 50% for the chordwise locations in the passage and spreads the loss core, originally concentrated in the suction side hub corner, in the pitchwise direction. The increase of tangential velocity of the leakage flow also makes the near hub passage flow more radially uniform, reducing the shear and resultant mixing loss between the passage and leakage flows near the hub. However, as observed by Ozturk *et al.* [24], a higher cavity tangential velocity increases the windage heating that affects the compressor efficiency.

Kim *et al.* [25] have studied the streamwise evolution of loss within a shrouded stator vane passage. They investigated a linear shrouded compressor cascade with an actual seal cavity, that employed a secondary flow loop to vary the leakage flow tangential velocity in the seal cavity. They observed, that the low momentum fluids continuously move towards the vane suction side near the hub endwall, because of the cross-passage pressure gradient. The losses successively increase until they reach the upstream edge of the downstream cavity trench, then they decrease because the cavity ingests high-loss fluids. Downstream of the cavity, the loss again begins to increase due to the wake shed from the vanes.

Recently, Lange *et al.* [26] investigated a four-stage axial LSRC using both cantilevered and shrouded stators on stage three and leaving the other stages unchanged. The aim of the work was to compare these two design philosophies under rear stage conditions, so the investigations were done within the third and fourth stage of the compressor. Tests were conducted at four different hub gaps for the cantilevered and three seal gaps for the shrouded. They observed that the shrouded vanes are more sensible to sealing clearance than cantilevered. At the design point, the shrouded performs better than the cantilevered for clearances less than 1.5% of the span, whereas near the stall, the cantilevered performs better for all the clearances considered. However, an extensive hub corner separation was found on the suction side of the shrouded stator even at the design point and with the smallest clearance. When the clearance increases, the hub corner separation greatly increases and for the larger clearance, it covers nearly the whole pitch and one third of the span. The authors explained, that the large corner separation even at the smallest clearance was a result of the large inlet blockage near the hub, which occurs due to the first and second stator hub clearances, or the unconventional design of the cavity with a fairly large mass flow recirculating through it.

Yoon *et al.* [8], while systematically investigating how the stator hub configuration and the stage design parameters affect the hub leakage losses across the stator, explained the higher sensitivity to the clearance observed by Lange *et al.* [26] for the shrouded configuration in comparison with the cantilevered one as a consequence of the single seal shroud employed. They in fact showed, that the use of multiple seals desensitize the aerodynamic performance as the seal clearance increases.

Yoon *et al.* [8] demonstrated that the hub leakage loss depends on the stage design parameters by using a simple analytical model for leakage flow, only including the aerodynamic losses directly attributable to the leakage flow and to the mixing with the main flow. In particular, for any given flow coefficient and work coefficient, the choice of the degree of reaction was found to be critical. An increase of the degree of reaction improved the efficiency of both the shrouded and the cantilevered configurations, but mostly of the shrouded. This is a consequence of the fact that, for the shrouded configuration, the increased degree of reaction has two positive effects: it decreases the pressure rise across the stator, consequently decreasing the leakage loss, and it decreases the kinetic energy at the stator inlet. For the cantilevered configuration, instead, there are two competing mechanisms: the positive effect caused by the kinetic energy decrease at the stator inlet is countered by the negative effect of an increased circumferential pressure difference between PS and SS when the pitch-to-chord ratio remains unchanged. For the cantilevered configuration, the pitch-to-chord ratio is very important, as it affects both the vane loading and the fraction of the leakage area. Increasing the pitch-to-chord ratio generally increases the hub leakage loss for a cantilevered case. Comparing the cantilevered and the shrouded design there is a break-even degree of reaction for which the shrouded configuration performs better. However, the performance of the shrouded configuration can be improved by increasing the number of seals and, for an adequate number of seals, the shrouded design always performs better than the cantilevered one. Additionally, the aerodynamic efficiency of the shrouded stator design is larger for a high degree of reaction. Therefore, a very effective way to increase the efficiency across a shrouded stator consists of combining a high degree of reaction with a multiple seals shroud. However, the blade loading across the rotors as well as the Mach number at the rotor inlet tends to increase when the degree of reaction is increased, thus resulting in higher rotor tip leakage loss and profile loss. For a low degree of reaction, the cantilevered configuration performs as efficiently as the shrouded one.

2.4 Motivation of the work

The choice of the optimum stator hub design is nowadays still very complicated, as the effect of the stator hub configuration strongly depends on the specific flow field being considered. However, the recent development in high performance computers has facilitated deep investigations of the flow field in a turbomachine configured with shrouded stators. This allows engineers to simulate detailed Computational Fluid Dynamics (CFD) models, in which the cavities are entirely recreated, thus avoiding the need for leakage models, and their effect on aerodynamic performance is fully considered [27].

In this work, detailed numerical studies are conducted with two major objectives. The first one is to better understand the impact of the stator hub architecture in a multi-stage axial configuration. In the past, many studies, such as Wellborn and Okiishi [21], have shown, that not only the stator row that is changed, but also all the downstream blade rows should be considered in the design phase of a multi-stage axial compressor. However, there is hardly anything published in the open literature on how the stator hub configuration affects the flow field of downstream stages in multi-stage axial compressors by investigating in detail the aerodynamic losses and efficiency for each downstream row. The impact of the stator hub on loss generation and transmission in a multi-stage machine is considered for two different subsonic multi-stage axial compressors: the LSRC and the HSC one. For the LSRC compressor only the third stator is altered from cantilevered to shrouded, whereas the other rows are left unchanged. The data generated by CFD simulations are firstly verified against the experimental (EXP) data, then used to go further into detail in those regions of interest in which experimental data could not be gathered or was simply not available. For the HSC, the first four stators are equipped firstly as cantilevered and then as shrouded. For both machines, the study of the loss generation and transmission is conduced by considering one baseline cantilevered configurations, in which all the stators are configured as cantilevered, and two shrouded configurations, which differ because of the clearance levels. Indeed, as shrouded stators generally allow smaller clearances than the cantilevered ones, a fair comparison between the two stator designs requires reduced clearances for the shrouded stators. Therefore, we consider a shrouded configuration with the same clearance level employed for the cantilevered configuration and one with reduced clearances.

The second objective of the work is to determine the specific machine's best parameters for a multi-stage axial compressor featuring shrouded stators. A parametric study is firstly performed on a reduced model, consisting of 2.5 stages of the original 5.5-stage model. For the reduced model, both a configuration with exclusively shrouded stators and one with only cantilevered stators is considered. The inlet boundary conditions differ between the shrouded and the cantilevered configurations, and are derived by simulating the relative stator hub designs for the entire model. The use of the reduced model allow us to perform a sensitivity study more quickly by speeding up the design process. The parameters investigated are: the clearances of the gap/sealing, the impact of the degree of reaction, and the impact of the camber line distribution in the stator hub region. Only for the clearances study both the cantilevered and the shrouded configurations are considered. Instead, for the degree of reaction and the stator near-endwall geometry study, only the shrouded configuration is investigated. Successively, the results of the parametric study are used to design two improved configurations, by combining the best results of the degree of reaction study and the endwall profile style one. Eventually, indications that designers can use to identify a good configuration of a multi-stage axial compressor with shrouded stators are derived.

3 Validation of modelling a low-speed multi-stage axial compressor

In the present chapter[1], the impact of changing the stator configuration from cantilevered to shrouded is investigated in a low-speed multi-stage axial compressor with respect to stage matching effects as well as loss generation and propagation.

Numerical analysis is carried out on those stator hub clearance settings, which are particularly relevant for considering the stage-wise effects of shrouded stator clearance change, and for which experimental data is available from the measurements of Lange [29]. The analysis firstly compares the experimental and numerical results for the two configurations in order to validate and prove the simulation results in those planes, for which traverse data is available. Then, the numerical data is used to further investigate those regions of interest, where experimental data could not be taken or is simply not available. The polytropic efficiency and absolute total pressure ratio across each compressor stage are considered. The trend observed is explained using the radial distributions of the deviation and the diffusion factor, as well as radial distributions and the 2D contour plots of the total pressure loss coefficient.

This provides an improved understanding of one of those regions in the axial compressor, which, although key to efficiency and stability, is still not fully understood in the context of multi-stage arrangements. Given the state-of-the-art for the effects of stator leakage flow in a multi-stage axial compressor, the present study narrowly investigates the aerodynamic mechanisms involved when the stator hub configuration at a given stage is changed and influences the performance and flow field details of the downstream stage.

[1]Part of the content of this chapter is based on the paper "Interacting Effects in a Multistage Axial Compressor Using Shrouded and Cantilevered Stators", De Dominicis *et al.* [28] published on the Journal of Propulsion and Power, Volume 37, Number 4 on July 2021; reprinted by permission of the American Institute of Aeronautics and Astronautics, Inc. See appendix D for more details.

3.1 Compressor configurations and experimental data available

Figure 3.1 depicts the Dresden LSRC investigated in this study. It is a large-scale rig featuring an inlet guide vane (IGV) and 4 stages, using a repeating stage design, and running at a nominal rotational speed of 1000 *rpm*. The LSRC, described in detail by Müller *et al.* [30] and Boos *et al.* [31], has been in operation since 1995 at the Dresden University of Technology [32]. The reference blading was designed as a large-scale model, being representative of the middle/rear stages of a high pressure compressor. It is built vertically upright to give flow measurements easy access anywhere along the flow path.

The present geometry was experimentally investigated by Lange *et al.* [1] to quantify and describe the effect of increased stator hub clearances for both design options, cantilevered and shrouded, and provide high quality experimental data for CFD validation. The experimental study of different clearances, conducted by Lange *et al.* [1], focused on the third and fourth vane by using identical rotors and rotor clearances, and configuring the third stator either in cantilevered or shrouded configuration. For the cantilevered configuration, all stages were configured with cantilevered stators

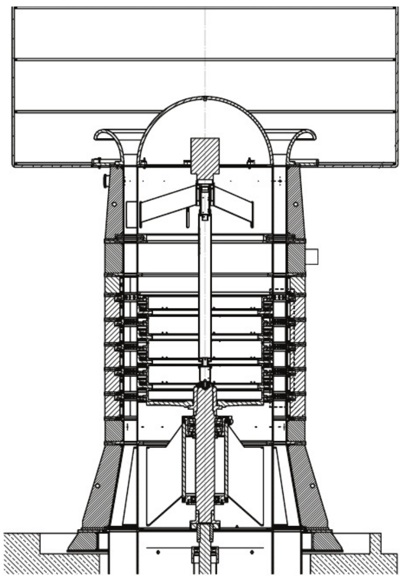

IGV + 4 identical stages			
Reynolds Number, rotor inlet, MS, DP			$5.7 \cdot 10^5$
Mach Number, rotor inlet, MS, DP			0.22
Design Speed			1000 *rpm*
Mass Flow, DP			25.35 *kg/s*
Mean Flow coefficient, DP			0.553
Enthalpy coefficient , DP			0.794
Hub diameter			1260 *mm*
Hub to tip ratio			0.84
Axial gaps between all blade rows, MS			32 *mm*
	IGV	rotor	stator
Blade number	51	63	83
Chord length, MS	80 *mm*	110 *mm*	89 *mm*
Stagger angle, MS	82.8 *deg*	49.3 *deg*	64.0 *deg*
Solidity, MS	0.941	1.597	1.709

Figure 3.1: LSRC, parameters for the reference building, Lange *et al.* [1]

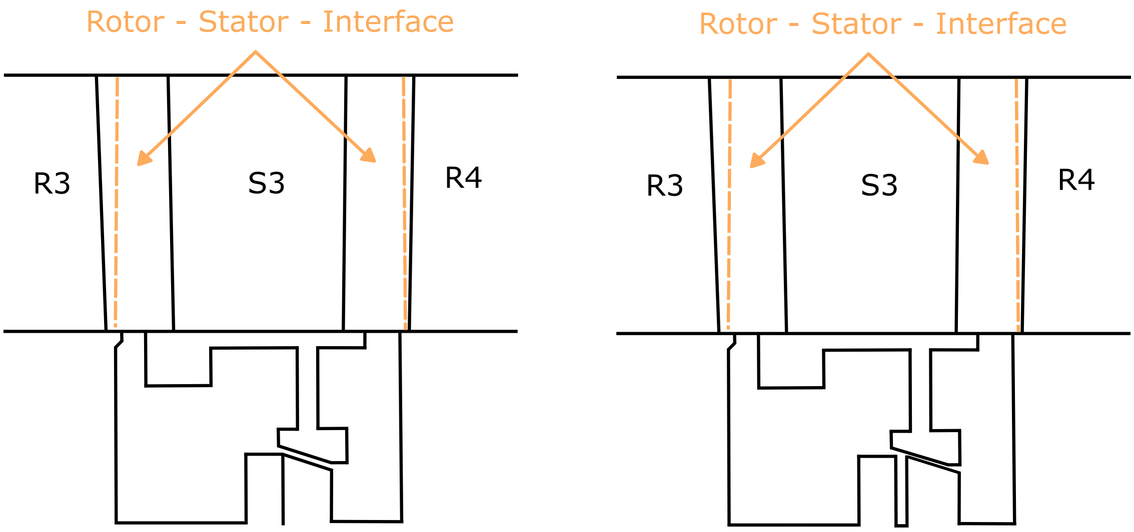

a) Increased seal clearance: 3.3% span b) Reduced seal clearance: 1.6% span

Figure 3.2: LSRC, geometry of the cavity for the two shrouded configurations

and four different hub clearance levels were considered. The shrouded configuration was investigated as a local third stator modification within the 4-stage cantilevered configuration, at three different seal gaps and rates of seal leakage mass flow through the cavity. The design point as well as near-stall conditions were analysed.

The cantilevered configuration is composed of an IGV and 4 stages. All the rotors have a tip gap of 1.25% span, i.e. approximately 1.3% of the chord length, and the first and second stators have hub gaps of 4.0% span, whereas the third and fourth stators have a hub gap which varies from 1.5% span, i.e. approximately 2.0% of the chord length, to 2.5% span, 4% span, and 5% span. For the shrouded configurations, only the third cantilevered stator was replaced with a shrouded stator including endwall fillets (radius of approx. 6.7% of span). The cavity, depicted in Figure 3.2, was chosen to match real design features, and a simple sealing ring was used instead of the typical labyrinth seal to allow additional measurements through the cavity. Here, with the aim of quantifying the effects of the seal clearance size, three different clearances were considered for the shrouded configurations: 1.0% span, 1.6% span, and 3.3% span. Instead, the hub gap used for the fourth stage was left unchanged and equal to 5% of the span. The isolated influence of the leakage flow on the third stage's performance, when the hub configuration is changed, as well as the influence of the third stage leakage flow on the fourth stage downstream, can be easily identified

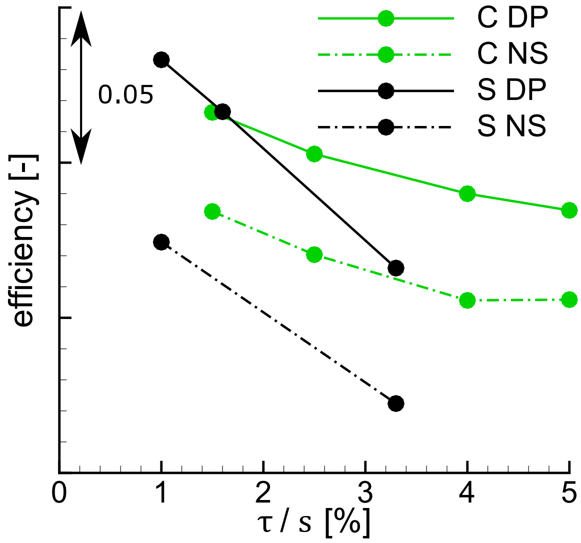

Figure 3.3: LSRC, isentropic efficiency with varying clearances [1]

since only the third stator hub configuration was changed by leaving unchanged the stages one, two, and four.

Re-configuring the third stator revealed that the shrouded stator is more sensitive to sealing clearance changes than the cantilevered stator with varying hub clearances. As shown in Figure 3.3, at the design point the shrouded configuration (S) has higher efficiency in comparison to the cantilevered (C) only if the clearance is lower than 1.5% span, whereas close to stall, the cantilevered configurations show always higher performance. Furthermore, the efficiency of the shrouded configuration, both at the design and near-stall points, strongly decreases when the clearances are increased. This can be a consequence of the high mass flow rates though the cavity, the high inlet blockage at the hub, but also, as pointed out by Yoon *et al.* [8], the geometry of the cavity with a single seal.

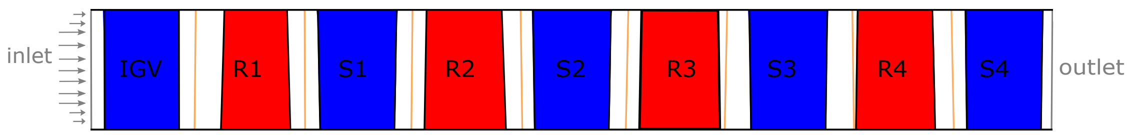

Figure 3.4: LSRC, geometry of the cantilevered configuration. In orange are shown the locations of the mixing plane interfaces

The blading in a meridional view of the LSRC, shown in Figure 3.4, was employed to carry out further numerical analysis of this 4-stage arrangement at those stator hub clearance settings which are particularly relevant for considering the stage-wise effects of shrouded stator clearance change, and for which experimental data are available from Lange's measurements [29].

Table 3.1: LSRC, stator tip levels considered

τ/s	Name	Abbreviation
1.6%	Reduced clearances	R
3.3%	Increased clearances	I
5.0%	Large clearances	L

Table 3.1 reports the different clearance levels investigated. For the cantilevered configuration, the hub gap of 5.0% span for the third and fourth stators was selected, whereas for the for the shrouded configurations, in order to quantify the effects of the seal clearance size, the two different clearances shown in Figure 3.2 were considered for the third stator: firstly a 3.3% span; then the seal clearance was reduced to 1.6% span.

3.2 Numerical Setup

The aerodynamic predictions for the cases described in this study were obtained using the DLR's CFD code TRACE [33], which solves the compressible three-dimensional Navier-Stokes equations in a rotating frame of reference:

$$\frac{\partial \hat{Q}}{\partial t} + \frac{\partial \hat{F}}{\partial \xi} + \frac{\partial \hat{G}}{\partial \eta} + \frac{\partial \hat{H}}{\partial \zeta} = \left[\frac{\partial \hat{F}_\nu}{\partial \xi} + \frac{\partial \hat{G}_\nu}{\partial \eta} + \frac{\partial \hat{H}_\nu}{\partial \zeta} \right] + \hat{S}. \tag{3.1}$$

The solution vector is $\hat{Q} = \frac{1}{J}[\rho, \rho u, \rho v, \rho w, \rho E]^T$, whereas the specific relative total energy E is defined as $E = e + \frac{1}{2}(u^2 + v^2 + w^2) - \frac{1}{2}\omega^2(y^2 + z^2)$ and $J = \partial(\xi, \eta, \zeta, t)/\partial(x, y, z, t)$ is the transformation Jacobian into a cell-local curvilinear coordinate system. The source term $\hat{S}$, containing the effective Coriolis and centrifugal forces, is $\hat{S} = \frac{1}{J}[0, 0, \rho\omega(y\omega + 2w), \rho\omega(z\omega - 2v), 0]^T$. A density-based scheme is used for the solution of the discretized equations. Density and pressure are coupled through the ideal gas equation of state $p = \rho RT$.

In the present work, steady three-dimensional RANS equations were solved. The idea behind the RANS equations is the Reynolds decomposition [34], whereby an instantaneous quantity, such as velocity, is decomposed into its mean and fluctuation:

$$\mathbf{U}(x,y,z,t) = \langle \mathbf{U}(x,y,z,t) \rangle - \mathbf{u}(x,y,z,t), \tag{3.2}$$

where the mean quantity $\langle \mathbf{U}(x,y,z,t) \rangle$ is defined as:

$$\langle \mathbf{U}(x,y,z,t) \rangle = \frac{1}{T} \int_0^T \mathbf{U}(x,y,z,t) \, \mathrm{d}t. \tag{3.3}$$

The Reynolds decomposition leads to the closure problem, since a consequence of the Reynolds decomposition is that the Reynolds stresses $\langle u_i u_j \rangle$ are unknown for the equations governing the mean velocity field. The closure problem consists of having only five independent equations and six unknowns. To determine the Reynolds stresses, i.e. to close the equations, it is necessary to include a turbulence model.

Over the last decades, two kinds of turbulence models have been developed: the eddy viscosity turbulence models, that use the Boussinesq hypothesis, and the Reynolds stress models, where a model transport equation is used for each Reynolds stress component. The Boussinesq hypothesis is based on the proportionality between the Reynolds stresses and the local velocity gradients:

$$\langle u_i u_j \rangle = -\nu_t \left(\frac{\partial \langle U_i \rangle}{\partial x_j} + \frac{\partial \langle U_j \rangle}{\partial x_i} \right) + \frac{2}{3} k \delta_{ij}, \tag{3.4}$$

where ν_T is the turbulent viscosity or the eddy viscosity. The turbulent kinetic energy k is by definition equal to the half of the trace of the symmetric tensor formed by the Reynolds stresses:

$$k = \frac{1}{2} \langle u_i u_i \rangle . \tag{3.5}$$

The two equation shear stress transport $k - \omega$ turbulence model based on Wilcox [35] was employed in this study. The two partial differential equations are solved for the turbulent kinetic energy k and turbulent frequency ω. The turbulent frequency ω is defined as $\omega = \epsilon / k$, where $\epsilon = 2\nu \langle s_{ij} s_{ij} \rangle$ is the rate of dissipation of turbulent kinetic energy, in which $s_{ij} = \frac{1}{2} \left(\frac{\partial u_i}{\partial x_i} + \frac{\partial u_j}{\partial x_i} \right)$. The $\kappa - \omega$ turbulence model is an eddy viscosity turbulence model. This turbulence model is well established not only in the treatment of the viscous near-wall region and in the accounting for the effects of streamwise pressure gradients, but also for numerical stability, as a consequence of simplicity. In fact, it allows Dirichlet boundary conditions and doesn't involve damping functions. The model's limit is in the treatment of non-turbulent free stream boundary conditions, where a boundary condition on ω is required and the calculated flows are very sensitive to the specified value.

To accurately capture the flow field near-wall surfaces, the low-Reynolds-number wall condition approach was used. This requires a fine mesh resolution close to the walls to achieve an average value of distance from the wall measured in viscous length y^+ equal to circa one. The definition of y^+, in accordance with Wilcox [36], is:

$$y^+ = \frac{u_t y}{\nu} \text{ with } u_t = \sqrt{\frac{\tau_w}{\rho}}, \tag{3.6}$$

where y is the distance of the first cell from the wall, ν is the local kinematic viscosity, and u_t is the friction velocity. The distance from the wall normalized by the viscous length scale y^+ determines the relative importance of viscous and turbulent processes. The size of the first cell depends on the thickness of the boundary layer: the thinner it is, the smaller are the cells on the boundary layer, and therefore the number of cells for the model increases.

Specifications of the solver used

In this project, the solver TRACE, developed by DLR's Institute of Propulsion and Technology in Cologne specifically to model and investigate turbomachinery blade rows, was used. It is a well established solver for turbomachinery applications [33], [37], [38], [39], [40], [41].

The solver was set as non-linear and steady, meaning that the steady RANS equations were solved. The equations are spatially discretized using a finite volume method. The spatial accuracy is second order for the governing equation, and first order for the transport equations of the turbulence model. The parameter entropy fix, which defines the Harten-Hyman Entropy-Fix [42] for Roe Solver [43], i.e. the lower entropy limit in the computations of the Roe fluxes at cell faces, is set to 0.002. This value is a compromise between high numerical dissipation, and hence the high stability of the computation achieved by the larger value of the Harten-Hyman Entropy-Fix, and the greater accuracy of the solution achieved with lower values. The Fromm scheme [44], in conjunction with the vanAlbadaSqr limiter, were used for the spatial discretization of the spatial derivatives for structured mesh. The limiter influences the gradients needed for the flux computations on the cell faces. This setting controls the limiter for the RANS equations but not for the additional transport equation for turbulence.

The discretization of the pseudo time operator is done using the predictor-corrector method [45]. It is an implicit Euler method and allows a Courant–Friedrichs–Lewy (CFL) number higher than 1. The CFL number defines the pseudo step of the pseudo time marching method used to solve the RANS equations.

The solution method applied to the transport equations of the turbulence models is an incomplete LU factorization. The rotational effect Bardina was used to increase the stability of separated flow. Furthermore, the Kato-Launder-modification, which alters the turbulence model production terms to reduce the tendency of the turbulence equations to over-predict turbulence production in regions with large normal strain, i.e. regions with strong acceleration or deceleration, was included in the model. For the heat flux model, the standard constant Prandtl number was used. The turbulent Prandtl number, i.e. a non-dimensional term defined as the ratio between the momentum eddy diffusivity and the heat transfer eddy diffusivity, was set to 0.9.

The numerical boundary conditions were matched to experimental data from the rig, which was designed to have a uniform flow without swirl at the entry of the IGV. Radial profiles of total pressure, total temperature, swirl angle, and radial flow angle were imposed at the inlet of the numerical domain, positioned at the axial location of measurements in the test rig. The inlet turbulence intensity was 0.05 and the inlet turbulence length scale was equal to 0.0001 m. A static pressure outlet boundary condition was applied in conjunction with radial equilibrium.

Ideal gas was used as the working fluid, with the specific gas constant equal to 287.06 J/kgK and the specific heat ratio equal to 1.4. Sutherland's law was used to relate dynamic molecular viscosity to temperature:

$$\mu = \mu_{ref} \frac{T_{ref} + S}{T + S} \left(\frac{T}{T_{ref}} \right)^{\frac{3}{2}} . \tag{3.7}$$

The reference temperature T_{ref} was 273 K, the reference molecular viscosity μ_{ref} at the reference temperature was 1.7198×10^{-5} Ns/m^2, and Sutherland's constant S was 110 K. A constant Prandtl number of 0.72 was used for the thermal conductivity model. The mixing plane approach was used all the way through the 4-stage machine. It is based on the non-reflecting boundary conditions developed by Giles [46] and Saxer *et al.* [47], in which the flux average is conserved at the interface. The locations of the mixing planes, depicted in orange in Figure 3.4, remained constant in the two configurations. Associated with this, single-passage models were applied to each of the 9 blade/vane rows. A non-matching fluid-fluid interface, which performs a flux conservative interpolation between non-matching grids, was used between the cavity and main flow path.

Mesh

The grid generator Autogrid of Numeca was used to model the geometry of the compressor. A structured mesh was generated for each row. The geometry was exactly replicated from the test rig including fillets. For the shrouded configuration, the leakage cavity of the third stator was modelled. It was fully meshed, resolving every detail of the stator shroud cavity.

Table 3.2: LSRC, evaluated grid sizes and results of the grid independence study

Grid n	no. of cells	$\dot{m}$ $[kg/s]$	$R_{n+1,n}$	$GCI_{n+1,n}$ [%]
1	22 347 456	26.499	1.1107	0.0133
2	16 309 424	26.502	1.1135	
3	11 813 632	26.507		

The grid size of the cantilevered configuration was varied keeping the endwall spacing constant in order to make an adequate choice, ensuring results largely independent from the mesh. The Grid Convergence Index (GCI) method, based on the Richardson extrapolation [48], was carried out. The mass flow rate at the outlet of the machine

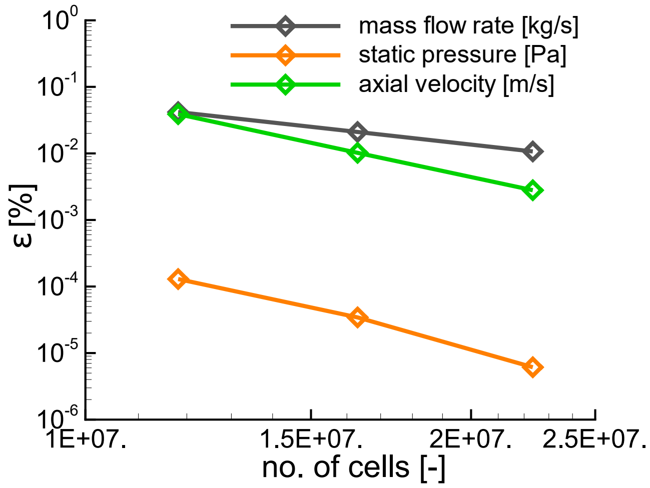

Figure 3.5: LSRC, numerical error as a function of cell number

was used to evaluate the three grids. Table 3.2 shows the number of cells n for each grid, the value of the mass flow rate at the outlet, the grid refinement factor R, and the grid convergence index, whereas Figure 3.5 shows the numerical error as a function of the number of cells.

According to the results, a mesh with 16 309 424 cells is considered to be sufficiently reliable to ensure grid independence and an averaged y^+ value lower than 1. Rotor blades are meshed with approximately 1 800 000 cells, whereas approximately 2 000 0000 cells are used for the stator vanes. Radially, 90 points are used for each aerofoil, to which 21 points are added within the tip clearance for the rotors and 30 points within the hub clearance for the stators. The two cavities, shown in Figure 3.2, were meshed with 922 752 cells and 1 171 584 cells respectively. A structured mesh was used for the cavities.

3.3 Results

The numerical simulations of the 4-stage axial LSRC at selected settings of stator hub clearance were carried out at the design point to use the results experimentally achieved by Lange [29] with the aim of enhancing the understanding of the flow field changes induced in the downstream fourth stage by the leakage flow in the third stator. The experimental data allow the verification of the data achieved by CFD simulations, confirming that the CFD is able to predict the flow phenomena linked with both the shrouded and the cantilevered configuration sufficiently well.

The results of the numerical simulations were then used to further assess the local aerodynamic behavior and the resulting stage interaction, which the stator hub configuration of the third stator induces in the fourth stage. In order to quantify the effects of different sealing clearances, two different shroud sealing clearances were considered. The different trends of the two stator hub configurations in terms of polytropic efficiency and the stage total pressure ratio were investigated by means of radial distributions of total pressure losses as well as the deviation and the diffusion factor across each row of the third and the fourth stage, with the aim of gaining insight into loss generation and transmission as well as the matching effects which characterize the two stator hub configurations. The secondary flow phenomena, linked with the two stator hub configurations, were investigated through 2D contour plots of the total pressure loss coefficient of the third stator, fourth rotor, and fourth stator.

3.3.1 Comparison of experimental and numerical data

The velocity and flow angle definitions used in the present analysis are shown in Figure 3.6. The mass-averaged radial distributions of normalized absolute total pressure, normalized axial velocity and absolute exit swirl flow angle downstream of the third stator and the fourth rotor are shown in Figure 3.7 and Figure 3.8 respectively, both for the cantilevered and the shrouded configurations at the larger stator hub/seal clearances: 5.0% span for the cantilevered configuration, CLE, and 3.3%

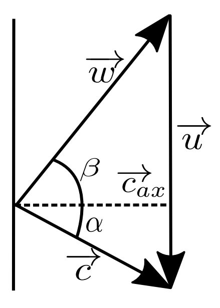

Figure 3.6: LSRC, velocities and flow angles definitions

span for the shrouded configuration, SIE. Each quantity was normalized by means of the corresponding mass-averaged value.

Overall, the numerical results agree reasonably well with experimental data, capturing the main trends for both stator hub configurations even though the shrouded case shows slightly more discrepancy between experiments and CFD results. Defining the reasons for these differences between experimental and numerical data is not trivial: they may be linked to both measurement inaccuracies and to the selection of numerical models in the computational study, such as the turbulence model.

The decision to solve the steady 3D Reynolds-Averaged Navier-Stokes equations with mixing planes at the interfaces between rotors and stators may limit the accuracy of the numerical predictions as observed by Lange [29], since the local influence of the upstream rows are not fully carried downstream due to circumferential averaging imposed at the interfaces. The uncertainty and data process errors for the experimental data have been reported by Lange *et al.* [1]: they are smaller than 0.5% of the midspan axial velocity for any velocity component and smaller than 0.25 degrees for the flow angles, whereas the total pressure ratio has been derived with a repeatability of $\pm 0.02\%$.

Considering Figure 3.7, the numerical prediction of the normalized absolute total pressure is in very good agreement with the experimental data in the area between 40% and 70% of the span both for the cantilevered and the shrouded configurations with larger seal clearance. Closer to the hub, in the inner 40% of the span, CFD predicts a lower absolute total pressure in comparison with the experimental data. There, the experimental and the numerical data present a different trend for the for the shrouded configuration; the normalized absolute total pressure distribution resulting from the CFD is almost linear, whereas the experimental data present a local minimum at 5% of the span. For the cantilevered configuration, the positions along the span of the local maximum and minimum of the absolute total pressure are numerically well predicted. For the axial velocity, the comparisons between experimental and CFD data show a similar trend with respect to the absolute total pressure: good agreement between 40 and 70% of the span, with CFD predicting close to the hub a lower value than the experiment proposes. For the cantilever-

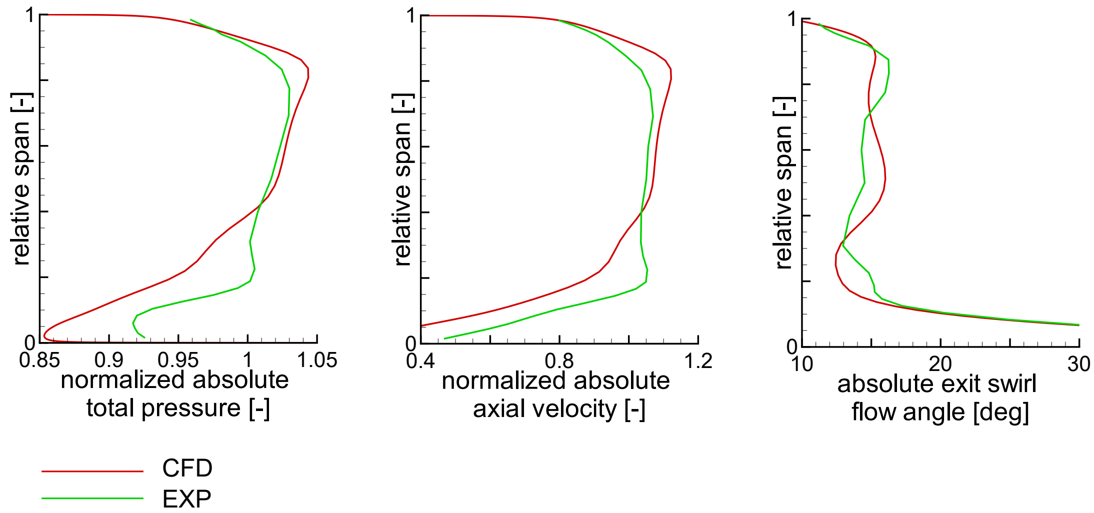

a) CLE

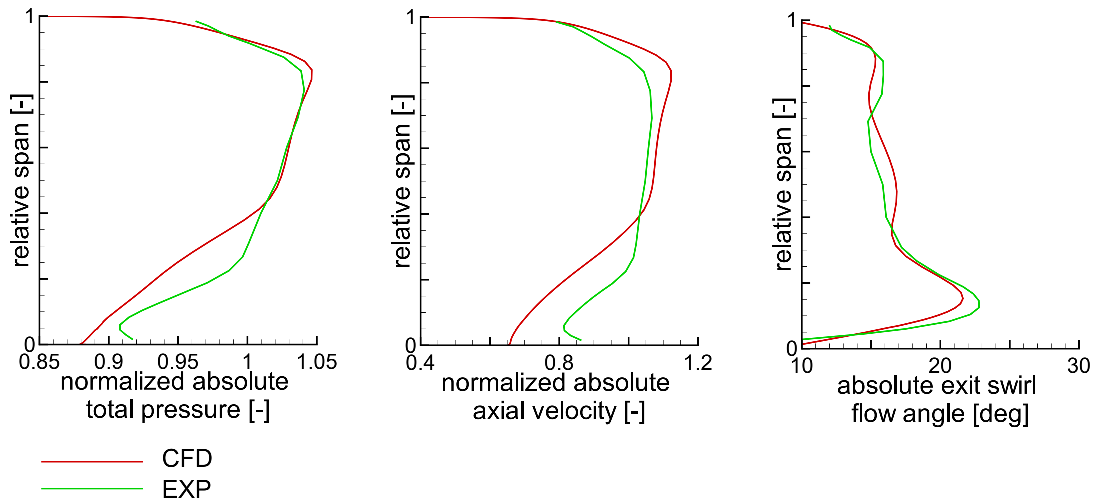

b) SIE

Figure 3.7: LSRC, radial distributions of normalized absolute total pressure, normalized axial velocity, and absolute exit swirl flow angle downstream of the third stator at the DP operating conditions

ed configuration, the local maximum and minimum in the hub region of the axial velocity are located at the same relative span; therefore the experimental and the numerical data are slightly off-set close to the hub. As observed for the normalized absolute total pressure, the experimental data show, for the shrouded configuration, a local minimum at 5% of the span not confirmed by the CFD which shows an almost linear trend. The numerical predictions of absolute exit swirl flow angles are in very good agreement with experimental data for both the designs considered along the full span.

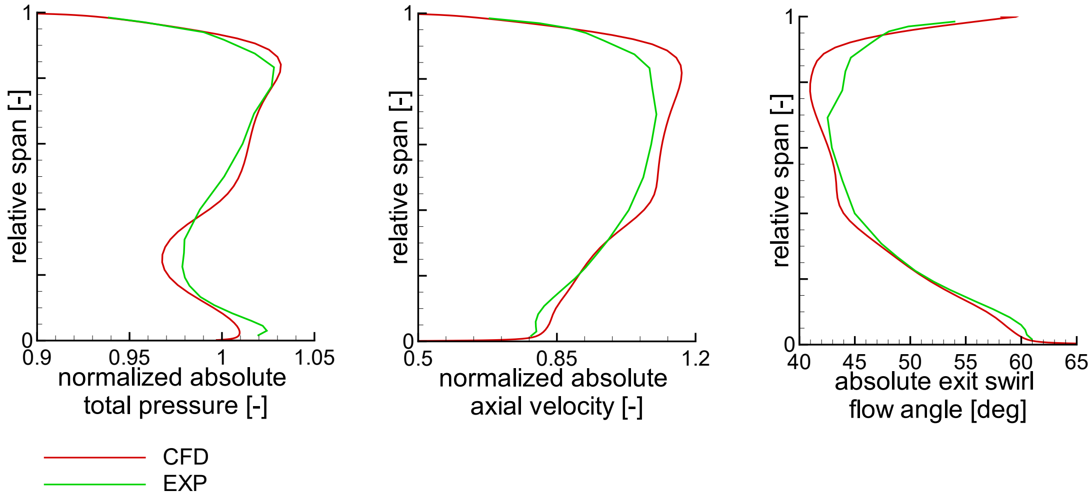

a) CLE

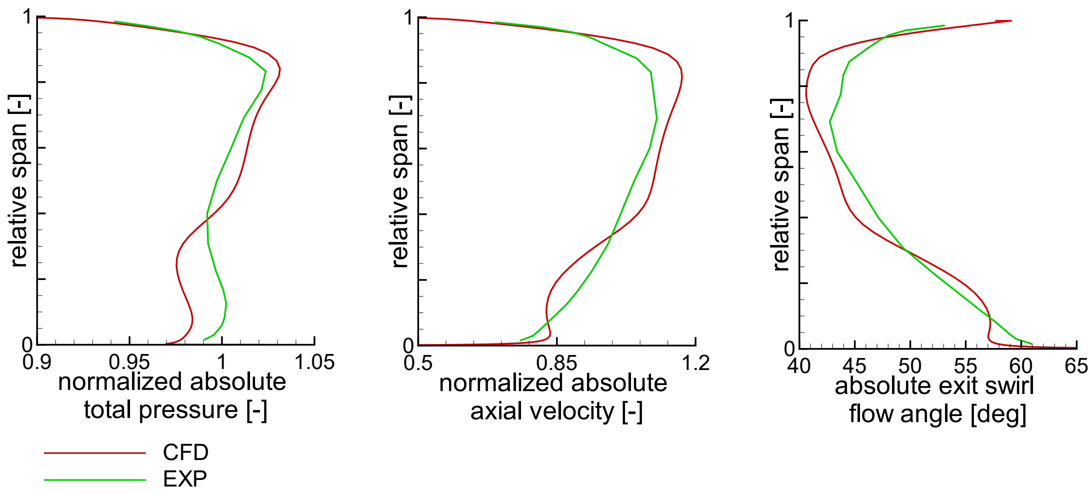

b) SIE

Figure 3.8: LSRC, radial distributions of normalized absolute total pressure, normalized axial velocity, and absolute exit swirl flow angle downstream of the fourth rotor at the DP operating conditions

Considering Figure 3.8, for the cantilevered configuration, the normalized absolute total pressure achieved by means of CFD study is in very good agreement with the experimental data in the area between 40 and 80% of the span. Closer to the hub, in the inner 40% of the span, the CFD predicts a slightly lower absolute total pressure; nevertheless the local maximum and minimum of the absolute total pressure are located at the same relative span. A lower value of the absolute total pressure, in comparison with the experimental data, can be also observed for the shrouded configuration in the inner 40% of the span. However, in this case, the difference is higher and the position of the local minimum in the hub region is not matched. As a consequence of the discrepancies close to the hub, in the shroud region, the experimental and the numerical data are slightly off-set. For the axial velocity, the comparisons between experimental and CFD data show small discrepancies for both the cantilevered and the shrouded case, with CFD predicting a higher value than the experiment proposes. This applies for both configurations along the entire span, with the exception, for the shrouded configuration, of the region between 8% and 35% of the span, where lower normalized absolute axial velocity are predicted by the CFD. The absolute exit swirl flow angles are lower in the CFD. The region of higher discrepancies between experimental and numerical data is, for the absolute exit swirl flow angles, close to the shroud, in the region of 75-95% of the span. The radial position of the local maximum and minimum in the hub region of the exit swirl flow angle is matched with a good agreement for the cantilevered configuration; whereas for the shrouded configuration, CFD predicts a local maximum at 20% of the span, but this is not confirmed by the experimental results.

The value of the mass flow rate through the cavity for the SIE configuration is, as shown in Table 3.3, in sufficient agreement with the experimental data. The measurement uncertainty of the shroud leakage flow was 0.5% of compressor mass flow. Hence, it was decided to use the leakage flow in CFD at the lower boundary of the uncertainty band.

Table 3.3: Cavity mass flow rate for the shrouded design with large clearance at the DP operating condition

	$\dot{m}_{cavity}/\dot{m}$ [%]
EXP	1.85
CFD	2.3 ± 0.5

The comparison of the experimental and CFD data confirms that the CFD is able to predict the dominant features of the flow, both when the third stator is configured as cantilevered and as shrouded. However, better matching with experimental data was observed for the numerical results of the cantilevered configuration when compared to those achieved for the shrouded configuration, in particular in the inner 40% of the span. Although there is no perfect match between experimental and numerical results, and this could not really be expected using the mixing plane approach and studying high level of stator clearances, the comparison confirms that CFD modeling approach taken here is valid to locally model and analyse flow phenomena linked with the two stator hub configurations within the domains across the third and fourth stage.

3.3.2 Effect of the stator hub configuration on the aerodynamic performance of downstream blade rows

The CFD results, which have been verified in the previous section by comparisons to available experimental data, are used to investigate the impact of the third stator hub configuration on the aerodynamic loss and flow field changes induced in the downstream fourth stage, the inlet flow conditions of which are strongly affected by the type of leakage flow from the upstream third stator. The results of the numerical simulations are used to go further into detail where experimental data are not available.

Based on the work of Lange *et al.* [1], the clearance sensitivity on this compressor was higher for the shrouded configuration. Therefore, in terms of loss generation in the hub region a 5.0% hub clearance on the cantilevered stator appeared to be approximately equivalent to a 1.6% shroud seal clearance on the shrouded stator. These two clearance values were anticipated in the present numerical simulations. However, in order to consider shroud clearance sensitivity and improve the understanding of the effect of the shroud seal clearance, two different clearances of the shrouded configuration were studied: 1.6% of span, SRE, and an increased clearance of 3.3% of span, SIE. Figure 3.9 shows the polytropic efficiency and the absolute total pressure ratio at the design flow across the four stages of the compressor in the two configurations, cantilevered and shrouded, and considers two different clearances for the shrouded design. It emerges that, since the redistribution of the flow field induced by stator configuration changes in the third stage is not large enough to influence the upstream stages, the first two stages are hardly affected. In contrast, the third stage itself and the fourth stage are strongly affected by the stator hub configuration change on the third stator. CLE and the SRE show a similar behaviour in terms of polytropic efficiency for the first three stages; however the efficiency of the cantilevered configuration on the fourth stage is lower than the efficiency of the

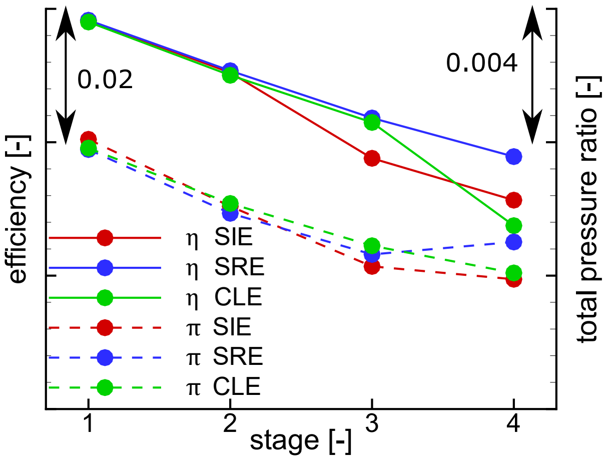

Figure 3.9: LSRC, polytropic efficiency and absolute total pressure ratio at the DP operating conditions for each stage

two shrouded designs in the fourth stage. SIE follows the same trend as SRE only in the first two stages. An important difference in terms of the polytropic efficiency between the two shrouded configurations can be observed in the third stage, where the performance of SIE has deteriorated in comparison with that of SRE. In the fourth stage, the two shrouded configurations show an equal reduction of the efficiency with respect to the third stage. The absolute total pressure ratio of CLE and SIE decreases almost linearly from the first stage to the third, with a higher slope for the shrouded configuration. This slope is substantially reduced for both configurations between the third and the fourth stage. SRE shows, instead, a linear trend of the absolute total pressure ratio only in the first two stages; in the third stage the slope is already substantially reduced, and in the fourth stage the absolute total pressure ratio has increased with respect to the upstream stage.

In order to gain a deeper insight into the understanding of the flow mechanisms related to the third stator configurations, the individual flow phenomena in the third and fourth stages are deeply investigated by means of both radial distributions and 2D contour plots. Figures 3.10, 3.11, and 3.12 show the radial distributions of the total pressure loss coefficient, the deviation and the diffusion factor.

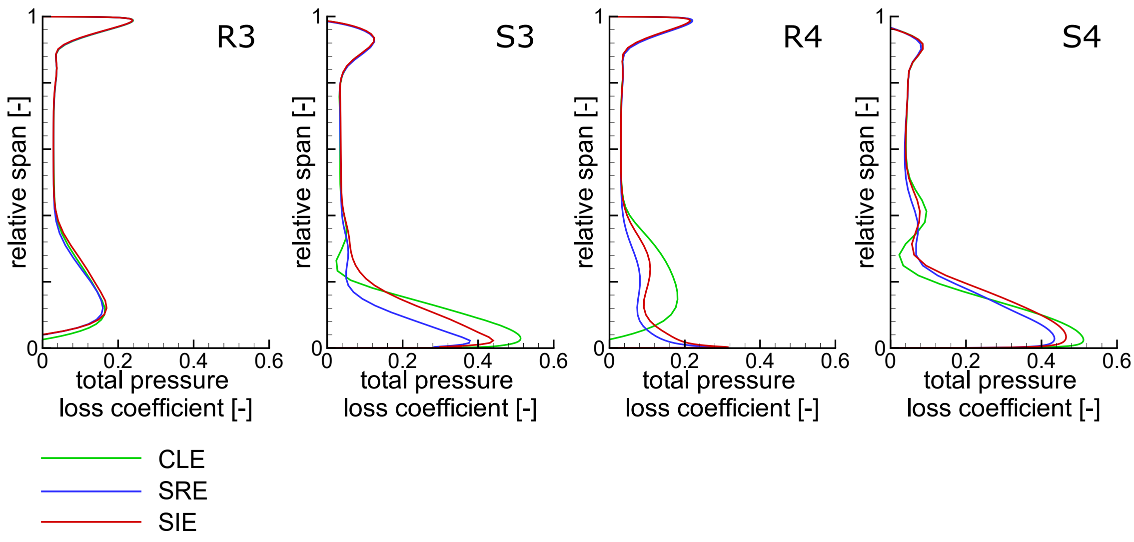

Figure 3.10: LSRC, radial distributions of the total pressure loss at the DP operating conditions for the cantilevered configuration and the shrouded configuration with two different levels of clearances

The radial distribution of the total pressure loss coefficient is defined as:

$$\xi_{pressure}(r) = \frac{\overline{p_{t,in}}(r_{in}) - p_{t,out}(r_{out})}{\overline{p_{dyn,in}}(r_{in})} \tag{3.8}$$

with $\overline{p_t}$ corresponding to the circumferential mass-averaged absolute total pressure for stators and circumferential mass-averaged relative total pressure for rotors. It is evident that only the lower 50% of the span is strongly affected by the third stator hub configuration. According to expectation, there are small changes behind the third rotor when only the third stator configuration changes. Considering the total pressure loss coefficient, see Figure 3.10, a local improvement of the third rotor performances can be observed near the hub, when for the shrouded case the clearance is reduced from 3.3% to 1.6% of the span. In terms of the third stator, CLE and SIE visibly cause a higher total pressure losses profile in the hub region, with the maximum located at the same relative span, very close to the hub, and higher in value for the cantilevered configuration. A different flow structure characterizes the two designs: in the cantilevered case, the rotating hub accelerates the fluid in the hub region and a clearance vortex is formed due to the leakage flow rolling up. For the shrouded configurations, the flow re-entering the main path is transported to the suction side of the stator vane by the pitchwise pressure gradient in the aerofoil passage. The boundary layer tends to separate on the suction side of the shrouded stator vane as a combined effect of the low momentum fluid collected there and the adverse pressure gradient. Since the stator hub configuration was changed only in the third stator, while stages one, two, and four remain unchanged, the fourth stage is indirectly influenced by the leakage flow in the third stage, since different inlet conditions are imposed at the inlet of the fourth rotor depending on the leakage flow on the third stator. The loss distribution on the fourth rotor shows large differences between the two stator hub designs in the hub region: the cantilevered configuration reaches the minimum value at the hub, negative in sign, whereas both the shrouded configurations reach their maximum value at the hub, positive in sign. Negative losses close to the hub are caused by radial re-distribution of near-endwall flow and passage vortex interaction with the low momentum fluid at the wall. Despite negative losses at the hub for the cantilevered configuration, a large portion of the span, between 15% and 40%, shows large losses. The resulting mass-averaged value of the total pressure losses on the fourth stator is higher for the cantilevered design than for the shrouded designs. Even if to a lower extent, the fourth stator is also influenced, indirectly, by the change of the third stator hub configuration. The total pressure losses for the cantilevered configuration in the fourth stage are very similar to the losses in the third stage, in particular very close to the hub. This result was expected since, for the cantilevered configuration, the third and fourth stators have not only the same design but also the same hub gap. The total pressure losses of the two shrouded configurations are instead higher in the fourth stage with respect to the third one. The large total pressure losses in the fourth stage for the cantilevered configuration are mostly responsible for the reduced polytropic efficiency in the fourth stage in comparison with the two shrouded configurations, see Figure 3.9.

Considering the radial distributions of the deviation, see Figure 3.11, it is evident that in the third stator, the two shrouded configurations have a deviation at the hub much lower than in the cantilevered case. This is a direct consequence of the leakage flow entering the main path through the cavity, which increases the passage vortex strength in the inner 10% of the span and consequently reduces deviation. For the shrouded configurations, the flow re-entering the main path grows the boundary layer; therefore the deviation for the cantilevered configuration is lower in the region of 15-60% of the span. The flow structures in the tip region are very similar for the three cases considered. At the outlet of the fourth rotor, the minimum value of the deviation is higher when the third stator is shrouded. For the cantilevered design, the

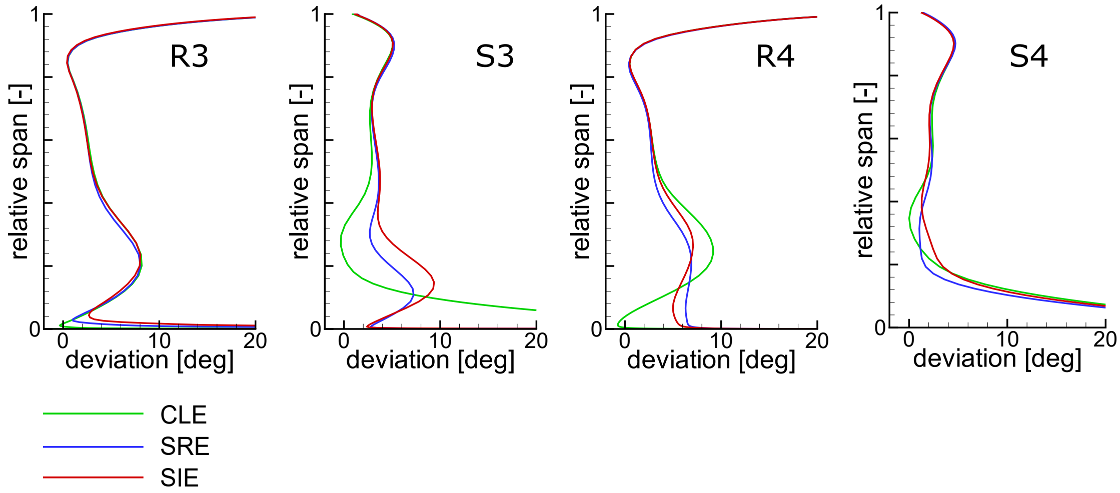

Figure 3.11: LSRC, radial distributions of the deviation at the DP operating conditions for the cantilevered configuration and the shrouded configuration with two different levels of clearances

minimum value of the deviation lies at the hub. In terms of the fourth stator, small differences between the stator hub configurations can be observed. The effect of the third stator leakage flow affects the fourth stator deviation in the region between 10% and 70% of the span.

Figure 3.12 depicts the radial distributions of the diffusion factor. It is defined as:

$$\mathrm{DF}(r) = \left(1 - \frac{v_{\mathrm{out}}(r_{out})}{v_{\mathrm{in}}(r_{in})}\right) + \frac{|v_{\theta,\mathrm{in}}(r_{in}) - v_{\theta,\mathrm{out}}(r_{out})|}{2\sigma v_{\mathrm{in}}(r_{in})} \tag{3.9}$$

where the first term on the right-hand side, $\left(1 - \frac{v_{\mathrm{out}}(r_{out})}{v_{\mathrm{in}}(r_{in})}\right)$, represents the mean deceleration of the flow and the second term, $\frac{|v_{\theta,\mathrm{in}}(r_{in}) - v_{\theta,\mathrm{out}}(r_{out})|}{2\sigma v_{\mathrm{in}}(r_{in})}$, represents the flow turning divided by the the solidity, equal to blade chord/blade pitch, which is important as this determines how well the flow is guided by the blades. v corresponds to the circumferential mass-averaged absolute velocity for stators and circumferential mass-averaged relative velocity for rotors. On the third stator, the loading of the cantilevered configuration is substantially higher in the hub region in comparison with the two shrouded configurations. This is a direct consequence of the hub clearance leakage, which increases the diffusion in the hub region. Changes in the diffusion factor occur across most of the span for both the third and the fourth stage:

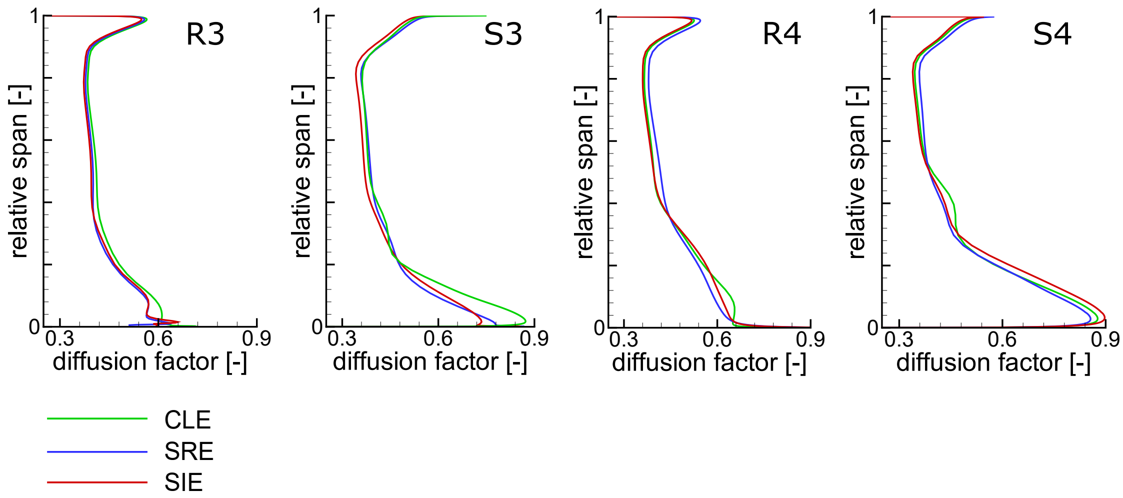

Figure 3.12: LSRC, radial distributions of the diffusion factor at the DP operating conditions for the cantilevered configuration and the shrouded configuration with two different levels of clearances

an increased value of loading in the upper span and a decrease of loading in the lower span for the shrouded configuration with a smaller seal clearance, with respect to the one with a larger seal clearance, can be observed for all the rows considered. This is consistent with the total pressure loss and the deviation previously mentioned: the decreased blockage near the hub forces less fluid to pass above, thus loading the tip and unloading the hub.

The improved pressure ratio of SRE in the fourth stage in comparison with SIE and CLE, see Figure 3.9, results from a combined effect of lower deviation, i.e. higher exit flow angles, both in the fourth rotor and in the fourth stator, and reduced total pressure losses.

Figure 3.13 shows the 2D distributions of the total pressure loss coefficient, defined as:

$$\xi_{pressure}(r,\theta) = \frac{\overline{p_{t,in}}(r_{in}) - p_{t,out}(r_{out},\theta)}{\overline{p_{dyn,in}}(r_{in})} \tag{3.10}$$

with $\overline{p_t}$ corresponding to the circumferential mass-averaged absolute total pressure for stators and circumferential mass-averaged relative total pressure for rotors. The 2D contour plots of the total pressure loss coefficient, see Figure 3.13, allow us to easily identify the secondary flow phenomena of the third stator cantilevered configuration, such as the aerofoil wakes V1. The clearance vortex V2 results from the circumferential pressure difference between the pressure side and the suction side. It is located on the pressure side of the vane, since it corresponds to the clearance vortex of the adjacent vane. A three-dimensional corner separation, V3, evolves

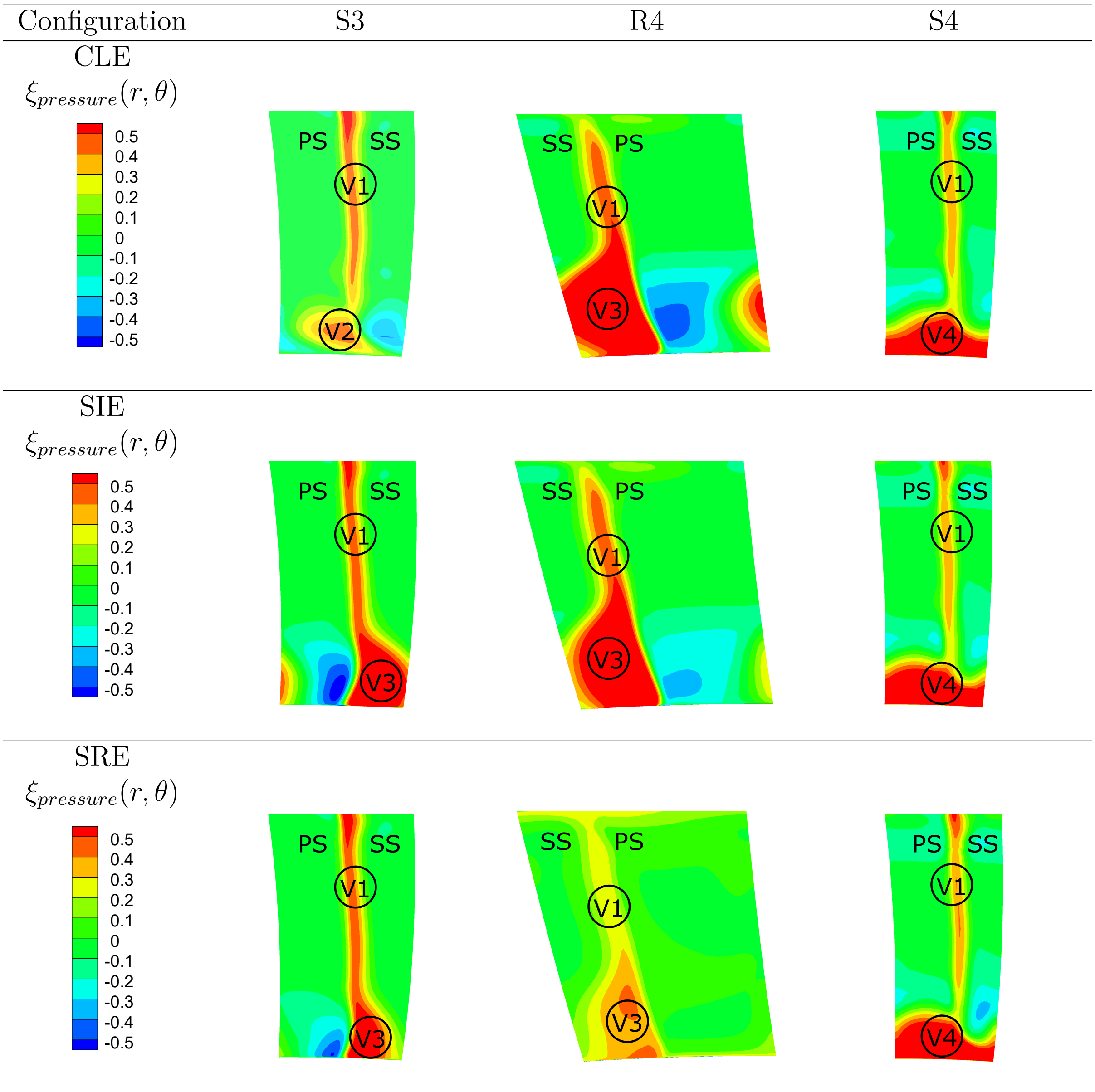

Figure 3.13: LSRC, area plot of total pressure loss coefficient at the DP operating conditions

on the suction side of the stator vane for the shrouded configurations. The corner separation is reduced for the shrouded case with smaller seal clearance, as it is mainly caused by low momentum cavity leakage fluid which re-enters the main path ahead of the stator from the upstream opening of the cavity [49] and, due to the cross-passage pressure gradient, collects on the suction side of the blade/vane, resulting in a high loss region in the hub suction side corner [25]. A large corner separation has been observed by Lange *et al.* [1] even for small clearances. The cause of this might be the large inlet blockage near the hub or the non-standard design of the cavity and seal arrangement. Since the blockage and loss distribution on the third stator are affected by the leakage flow, the inlet flow conditions of the downstream rotor are modified by the stator hub configuration of the upstream stator. Despite that, for the two configurations with larger seal clearance, i.e. CLE and SIE, the total pressure loss coefficient of the fourth rotor shows a similar trend: a huge region of losses, due to the three-dimensional corner separation V3, on the suction side of the blade/vane which is extended over a large percentage of the span and, especially for the cantilevered case, for more than half of the distance between the suction side and the pressure side of the adjacent blade/vane. This leads to higher losses in the cantilevered configuration for the fourth rotor. For the shrouded configuration with reduced seal clearance, it may be interesting to observe that the decrease of total pressure losses in the fourth rotor affects not only the hub region but, to a lesser extent, also the shroud region. The fourth stator is also affected by the stator hub configuration of the third stage, but mostly within the inner 25% of the span. Large endwall separations, V4, are clearly visible, possibly due to the fact of this stator being the last stator, with no downstream rotor. The shrouded case with reduced seal clearance shows, for all three rows investigated, a trend similar to the one achieved with larger clearance; however, the losses are drastically reduced. These results confirm the trend already observed in different, previous studies by Swoboda *et al.* [7], Sohn *et al.* [23] or Fröebel *et al.* [50]: namely, a decrease of the mass flow through the cavity results in a decrease of the total pressure losses.

The 2D contour plots of the total pressure loss coefficient, shown in Figure 3.13, provide a deeper insight into the flow structure resulting from the two stator hub configurations in the downstream stages, and confirm the trend observed for the radial distribution of the total pressure loss coefficient in Figure 3.10. Evidently, the total pressure losses on the fourth rotor are higher for the cantilevered configuration and lower for the shrouded case with reduced clearance, whereas the losses on the fourth stator are similar in all three cases. The trend of the polytropic efficiency, see Figure 3.9, is a direct consequence of the total pressure loss coefficient: in the fourth stage, higher total pressure losses for the cantilevered configuration result in lower polytropic efficiency, as well as lower total pressure losses for SRE results in higher efficiency. The large three-dimensional corner separation on the third stator of SIE shown in Figure 3.13, is mainly responsible for the polytropic efficiency deterioration of the third stage that is observed for SIE in comparison with SRE.

3.4 Conclusion

In this chapter the impact of stator hub leakage in a section of a 4-stage axial LSRC featuring a local third stage change of stator hub configuration was investigated. As a starting point, a verification of CFD, as being able to correctly predict the dominating phenomena of the flow for both cantilevered and shrouded configurations, was performed by comparing experimental and numerical results. Then, the CFD modeling was used to investigate the effects of the stator hub configuration on aerodynamic loss generation and transmission, as well as stage matching; radial distributions of the deviation and the diffusion factor, as well as radial distributions and 2D contour plots of the total pressure loss coefficient, gave insight into the flow phenomena induced in the downstream stage by the change of stator 3 hub configuration, and explained the trend observed for stage polytropic efficiency and stage pressure ratio.

The results showed that the rotor upstream is only slightly influenced by the stator hub configuration, whereas the stage downstream is strongly affected in the lower 50% of annulus height. The polytropic efficiency and the absolute total pressure ratio at the design flow for each stage of the machine show that, for the cantilevered and for the shrouded configuration with smaller clearance, the polytropic efficiency behaves similarly in the stages upstream and including the stage where the stator hub configuration was altered. The downstream stage instead shows a lower polytropic efficiency for the cantilevered case in comparison with both the two shrouded designs, caused by larger total pressure losses in the downstream stage for the cantilevered configuration. The trend of polytropic efficiency for the two shrouded configurations is similar for the upstream stages, whereas for the shrouded configuration with increased seal clearance, the performance of the altered stage deteriorated, due to a large three-dimensional corner separation on the altered stator. The predictions of the absolute total pressure ratio show that the cantilevered and the shrouded with increased clearance follow a similar trend, with the total pressure ratio decreasing along the machine, whereas the shrouded with reduced clearance has, in the stage downstream of the altered stage, a higher absolute total pressure ratio with respect to the upstream stage. This is a consequence of the combined effect of lower deviation and reduced total pressure losses, both in the downstream rotor and in the downstream stator.

In conclusion, when the design of the fourth rotor is kept unchanged and not tailored to the exit flow of the upstream stator, the impact of the third stator hub configuration alteration is drastically high on the fourth rotor aerodynamic performance, and consequently, due to reduced rotor pressure ratio, the downstream stator changes the aerodynamic performance by unexpectedly low increments.

4 Investigation of a high-speed multi-stage axial compressor

The analyses of the last 5.5-stage of a high-speed 11-stage axial compressor are presented in this chapter[1]. Starting from the baseline cantilevered configuration of the entire model, in which all the stators are configured as cantilevered and have the same level of clearance, two shrouded configurations are achieved by changing the stator hub configuration of the first four stators of the 5.5-stage compressor model. The two shrouded configurations differ because of the level of clearance considered for the stator vanes.

Firstly, the regions of higher losses for both the cantilevered and the shrouded stator hub configurations are identified, and the loss generation and propagation in the multi-stage arrangements are evaluated.

Successively, a parametric study is performed on a reduced model, consisting of 2.5 stages of the entire model. The parameters investigated are: the clearances of the gap/sealing, the impact of the degree of reaction, and the impact of the camber line distribution in the stator hub region. The results are used to design two improved shrouded configurations for the compressor under investigation. Furthermore, generic recommendations for determining the improved designs of a multi-stage axial compressor with shrouded stators are derived.

4.1 Baseline cantilevered geometry and set-up

The geometry of the baseline cantilevered configuration. taken from a design study, is shown in Figure 4.1. As the entire model consists of the last 5.5 stage of a 11-stage compressor, the first stage considered is stage 7. The position of the inlet is located on the measurement plane of the inlet boundary conditions. The compressor

[1]Part of the content of this chapter is based on the paper "Numerical Evaluation of Losses in Shrouded and Cantilevered Stators of a Multi-Stage Axial Compressor", De Dominicis *et al.* [51], Proceedings of the ASME Turbo Expo, 2021.

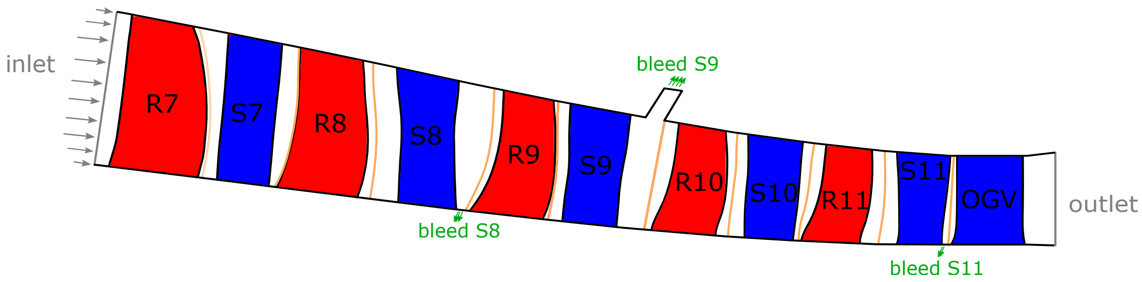

Figure 4.1: HSC, baseline cantilevered geometry of the entire model. The locations of the bleeds for S8, S9, and S11 are shown in green, and the locations of the interfaces are depicted in orange

includes three bleeds, on S8, S9, and S11, taking approximately 2%, 3%, and 1% of the inlet mass flow of the compressor. As shown in Figure 4.1, for the bleed of S9 a bleed slot is gridded, whereas for the bleeds of S8 and S11 a sink located at the hub is used due to their smaller mass flow. All the stators are configured as cantilevered, having the same levels of clearance of approximately 1.5% of the S7 span. Also the outlet guide vane (OGV) has the same clearance of the stators. The clearances of the rotors instead vary from stage to stage.

Figure 4.1 depicts the locations of the interfaces, which correspond to the evaluation stations for the flow proprieties calculations. Their shape is curved, and is adapted to the geometry of the aerofoil to maintain a constant distance to the interfaces. Their locations are not varied for all the configurations considered. The mixing plane approach, based on the non-reflecting boundary conditions developed by Giles [46] and Saxer *et al.* [47], is used for the whole machine from inlet to outlet except for the connection between S11 and OGV. There, a non-matching fluid-fluid interface, which is a conservative cell approach of second order accuracy as described by Yang *et al.* [52], is imposed. As only one passage is modelled, periodic boundary conditions are used. The solid walls are modelled as viscous walls using wall functions treatment.

The numerical boundary conditions are matched to the numerical results achieved from the simulation of the 11-stage compressor. Radial profiles of total pressure, total temperature, swirl angle, radial flow angle, turbulence intensity, and length scale are imposed at the inlet of the numerical model. A radial distribution of static pressure is employed as the outlet boundary condition.

4.2 Numerical Setup

Specifications of the solver used

Steady three-dimensional RANS are solved in conjunction with the SST $\kappa - \omega$ turbulence model. An introduction of the RANS equations is given in section 3.2.

The two-equation SST $\kappa - \omega$ turbulence model is employed in the formulation given by Menter [53]. The two partial differential equations are solved for the turbulent kinetic energy k and turbulent frequency ω. The Menter SST $\kappa - \omega$ turbulence model is an eddy-viscosity turbulence model, and such as, it has a limitation in correctly predicting the onset and the amount of separation in adverse pressure gradient flows [54]. However, Johnson and King [55] clearly demonstrated that, the ability of an eddy viscosity model to predict strong adverse pressure gradient flow is ultimately determined by the eddy viscosity in the wake region. Therefore, in the Menter SST $\kappa - \omega$ the classical eddy viscosity formulation was redefined as described by Mentor [56] so as not to violate Bradshaw's observation [57]. Bradshaw noted that the principal turbulent shear stress is proportional to the turbulent kinetic energy in the wake region of the boundary layer. The model name SST, which means Shear Stress Transport, is given by the modification to the eddy viscosity, in which the wall-bounded flow takes into account the effect of the transportation of the principal turbulent shear stresses.

The model is designed to yield the best behavior of two well-established turbulence models, i.e. the $\kappa - \omega$ and the $\kappa - \epsilon$ turbulence model, which are combined by means of a blending function. The $\kappa - \omega$ turbulence model based on Wilcox [58] is used in the sublayer of the boundary layer. An introduction of the model is given in section 3.2. The standard $\kappa - \epsilon$ turbulence model [59] is used in the free stream and in the wake region of the boundary layer. The $\kappa - \epsilon$ and the $\kappa - \omega$ turbulence models have the same expression for ν_T and the same κ equation. They differ only for inhomogeneous flows, where the $\kappa - \epsilon$ turbulence model contains an additional term.

The performance of the $\kappa - \epsilon$ turbulence model at a free stream boundary layer was studied by Cazalbou *et al.* [60] and has been proved to be more accurate in comparison with the $\kappa - \omega$ turbulence model. It is a widely used turbulence model and over the years many modifications have been proposed to improve performance for a specific class of flows. The two model transport equations are solved for the turbulent kinetic energy κ and the dissipation ϵ. The dissipation ϵ describes how the kinetic energy is transformed into internal energy by the work of the fluctuating velocity gradients $\frac{\partial u_i}{\partial ux_j}$ against the fluctuation of deviatoric stresses $2\nu s_{ij}$ and is, by definition, non-negative. The standard model transport equation for ϵ is empirical and contains a number of model constants. Close to the walls, in flow characterized by high adverse pressure gradients, it may lead to discrepancies, such as too high skin friction coefficients as observed by Rodi *et al.* [54].

Concerning the other solver specifications, those described in section 3.2 are used, except for the value of the lower entropy limit in the computational of the Roe fluxes at cell faces. This value is set to 0.075, as recommended for configurations with wall functions. Thermally perfect gas is used as the working fluid, with the specific gas constant and the specific heat ratio function of the temperature.

Mesh

A structured mesh was generated for each row of the baseline cantilevered configuration by using the commercial grid generator Autogrid from Numeca. The GCI method, based on the Richardson extrapolation [48], was used to choose the grid size, ensuring results independent from the mesh. The number of cells were varied by keeping the endwall spacing constant. The mass flow rate at the outlet of the machine was used to evaluate the three grids. Table 4.1 shows the number of cells n for each grid, the value of the mass flow rate $\dot{m}$ at the outlet, the grid refinement fac-

Table 4.1: HSC, evaluated grid sizes and results of the grid independence study for the cantilevered baseline configuration

Grid n	no. of cells	$\dot{m}$ $[kg/s]$	$R_{n+1,n}$	$GCI_{n+1,n}$ [%]
1	22 949 120	595.72	1.3393	0.0491
2	9 552 064	595.82	1.3681	
3	3 730 288	595.89		

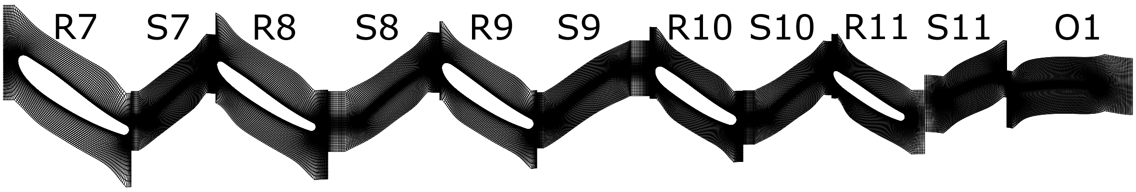

Figure 4.2: HSC, grid topology at the hub

tor R, and the grid convergence index GCI. The results show that a mesh with 9.55 million cells is sufficiently reliable to ensure grid independence for the cantilevered configuration.

The solid wall cell width, equal to $y = 5e - 5\ m$, was chosen to guarantee a non-dimensional y^+ value adequate for the wall treatment with wall functions. Indeed, to save computational time, in this work the wall treatment approach with wall functions was used. In order to do that, firstly the results achieved with the wall functions mesh were validated against those of a more accurate low-Reynolds mesh. The validation, which is reported in appendix A, has proven a very good agreement between the two approaches, thus has demonstrated that the wall functions approach is able to capture sufficiently correctly the flow phenomena.

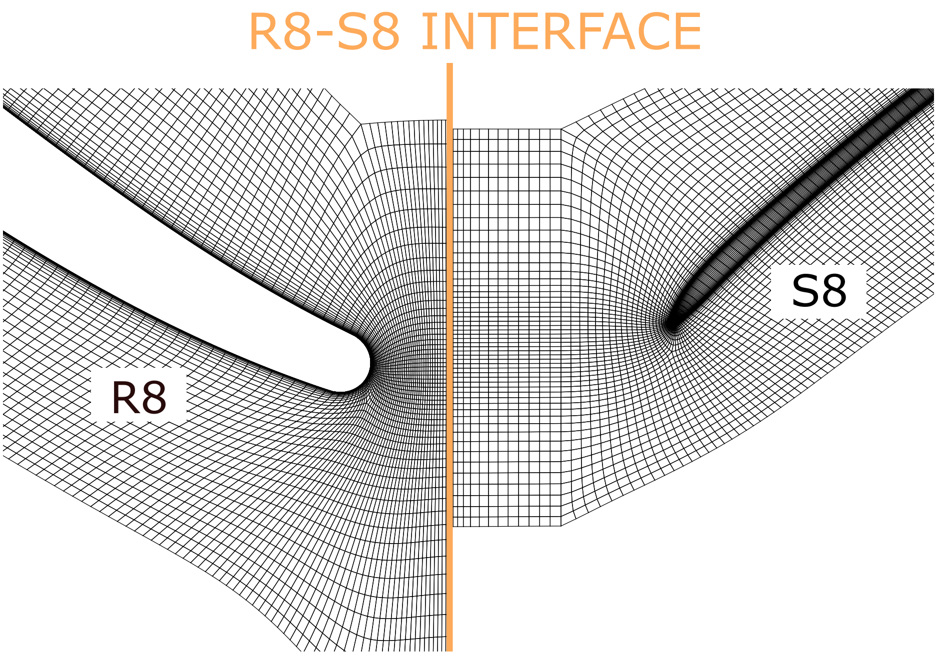

Figure 4.3: HSC, grid topology at the interface between R8 and S8 at the hub

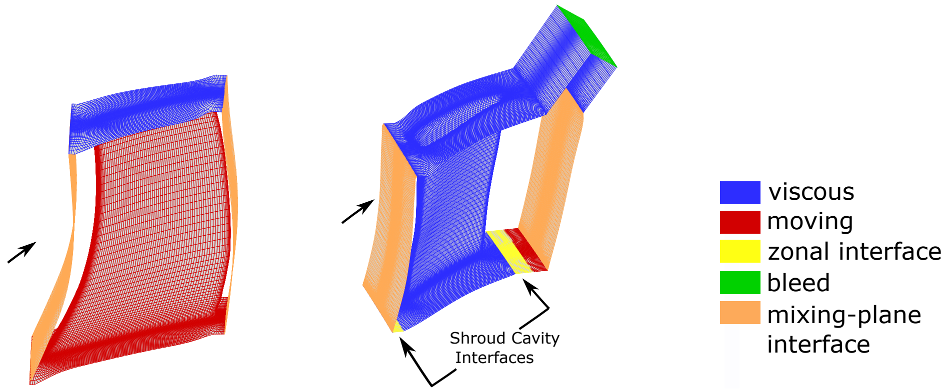

a) R9 mesh

b) S9 mesh

Figure 4.4: HSC, stage 9 mesh details

At the interfaces, the same grid resolution was used perpendicular to the interface itself. Figure 4.2 shows the grid topology at the hub and in Figure 4.3 is depicted the detailed view of the interface between R8 and S8 at the hub. Figure 4.4(a) and Figure 4.4(b) show the mesh details of respectively R9 and S9. The radial grid resolution is identical in each row, consisting of 89 points with 17 points in the hub and tip clearances. To save computational time, the points are clustered in the regions where large radial changes of flow properties are expected, such as solid boundaries and regions of tip leakage flow. This guarantees a sufficient grid refinement in these regions. Conversely, fewer points are used in the areas where limited radial changes of flow properties are expected, such as at midspan. The number of points used for each row is shown in Table 4.2.

Table 4.2: HSC, number of cells for each row for the cantilevered baseline configuration

R7	R8	R9	R10	R11	
7.45 M	8.70 M	7.36 M	9.24 M	8.85 M	
S7	S8	S9	S10	S11	OGV
9.57 M	8.32 M	9.39 M	8.23 M	8.21 M	9.96 M

4.3 Assessment of different stator hub configurations

To assess the impact of the stator hub design in the 5.5-stage axial machine, we consider, as reference configurations, both the baseline cantilevered configuration, equipped exclusively with cantilevered stators, and a shrouded one, of which the first four stators are equipped with shrouded stators.

The first four stators have, for each configuration investigated, the same clearance level. Instead the clearances of the rotors, of the OGV and of S11, remain unchanged across the different configurations. The clearance level of the two reference configurations is different. Nominal clearances, equal to circa 1.5% of the S7 span, are used for the reference cantilevered configuration and reduced clearances, equal to approximately 1.1% of the S7 span, are employed for the reference shoulder configuration. Indeed cantilevered vanes require relatively large hub-to-endwall clearances to avoid rubs and possible catastrophic damage, whereas shrouded vanes allow smaller clearances, as the impact between the seal and the fins is not so dangerous as it would be for cantilevered stators. Additionally, we consider a shrouded configuration with the same clearances as those used for the reference cantilevered configuration.

4.3.1 Shroud cavity definition

Starting from the baseline cantilevered configuration, the reference shrouded configuration was derived by replacing the stator hub design of the first four cantilevered stators with shrouded ones. Figure 4.5 depicts the geometry of the cavity. It is the typical geometry of a labyrinth seal. The upstream axial opening has a rounded shape which facilitates the re-entering of the leakage flow into the main path with lower losses. The shape of the hub line is modified to be adapted for the rounded shape of the cavity in the upstream axial opening.

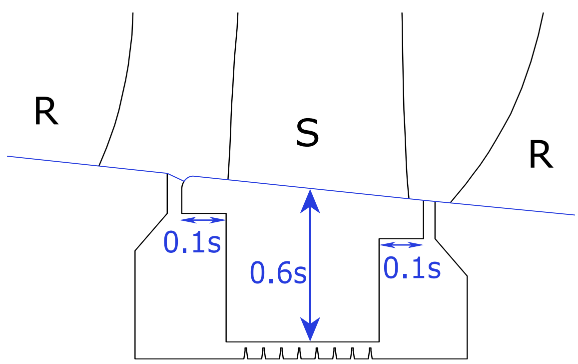

Figure 4.5: HSC, geometry of the cavity

The number of fins is selected to achieve for each stator similar values of leakage mass flow, total temperature, and tangential velocity difference between the upstream and downstream axial openings of the cavity as those available.

Although the same kind of geometry is used for all the cavities, the geometry of each cavity is adapted to the specific stator geometry. Indeed, the cavity specifications depend on the span of the relative stator s as shown in Figure 4.5. A constant upstream axial opening of circa 5 mm and a constant downstream axial opening of circa 4 mm is used for all the cavities with the exception of S9 downstream axial opening. There, because of the larger axial space available between the S9 trailing edge and R10 leading edge, an axial distance of 10 mm is used.

4.3.2 Aerofoil modification

For the two reference configurations, the aerofoil design was maintained unchanged, with the exception of the position of the maximum thickness along the span, which was adapted for the shrouded vanes, aiming to account for the mechanical requirements of the shrouded configurations. Indeed, the cantilevered design is pinned only on the casing, whereas the shrouded design has also a connection at the stator hub. This reduces the vibration problems but increases the weight and the radius of the vane.

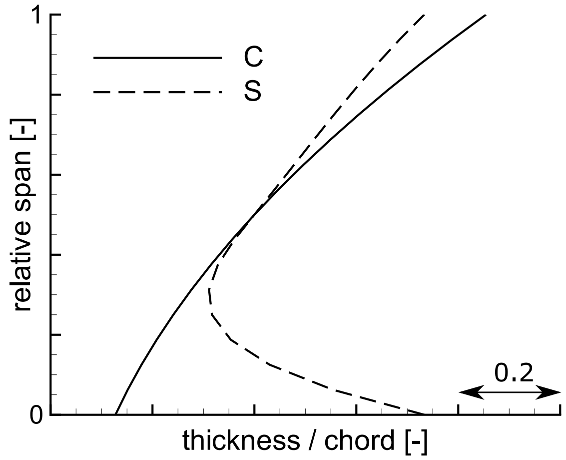

Figure 4.6: HSC, thickness-to-chord ratio distributions for the cantilevered and the shrouded stator vanes

The different structural requirements of the two stator hub configurations lead to different thickness distributions along the span as shown in Figure 4.6. For cantilevered vanes, the thickness-to-chord ratio increases gradually from hub to shroud. Instead, for shrouded vanes, the value of the thickness-to-chord ratio is maximum at the hub and the shroud, and has its minimum at circa 30% of the span. At midspan the two distributions coincide. The value of the maximum thickness, as well as the other vane parameters, remains instead unchanged.

4.3.3 Introduction of shrouded stators

The reference shrouded configuration is depicted in Figure 4.7. The locations of the mixing plane interfaces, which are unchanged respect to the reference cantilevered configuration shown in Figure 4.1, are selected to have the entire cavities within the stator domains, thus avoiding interfaces inside the cavity.

The location of the bleed of S8, directly on the hub for the cantilevered configuration, is moved into the cavity for the shrouded configuration. The bleeds on S9 and on S11 are instead left unchanged between the two configurations.

The introduction of the cavities requires the introduction of non-matching interfaces at the axial openings between the cavities and the main path. As shown in Figure 4.8 only for S9, a fluid-fluid interface is used, between the main path and the cavity, both for the upstream and the downstream openings. For the other stators, a fluid-

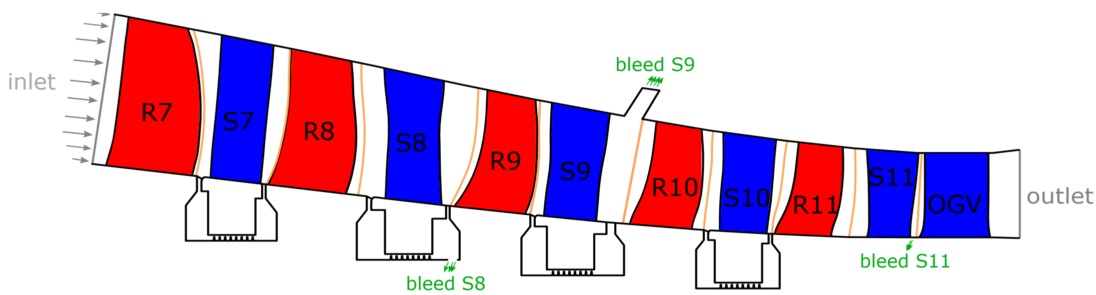

Figure 4.7: HSC, reference shrouded geometry of the entire model. The locations of the bleeds for S8, S9, and S11 are shown in green, and the locations of the interfaces are depicted in orange

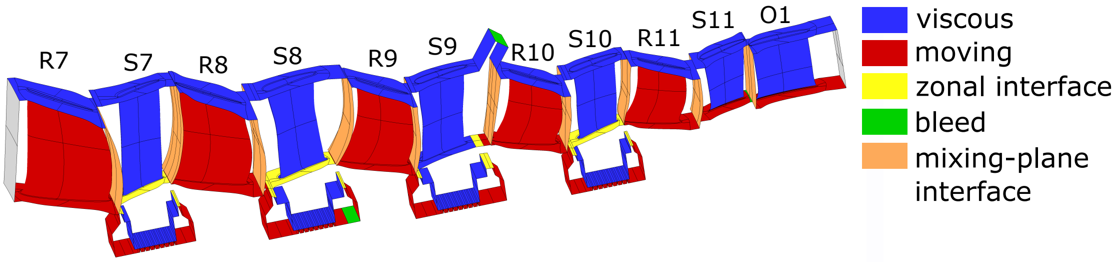

Figure 4.8: HSC, shrouded set-up

fluid interface is used for the upstream opening and a mixed fluid-solid interface is employed for the downstream opening, thus improving the mesh resolution in those regions with reduced axial space.

4.3.3.1 Mesh of the shrouded stator

Table 4.3: HSC, number of cells for each cavity for the reference shrouded configuration

S7	S8	S9	S10
7.95 M	7.65 M	7.84 M	7.13 M

For the shrouded configurations, the labyrinth seals are meshed and resolved in every detail including fillets. Table 4.3 reports the number of cells for each cavity for the reference shrouded configuration.

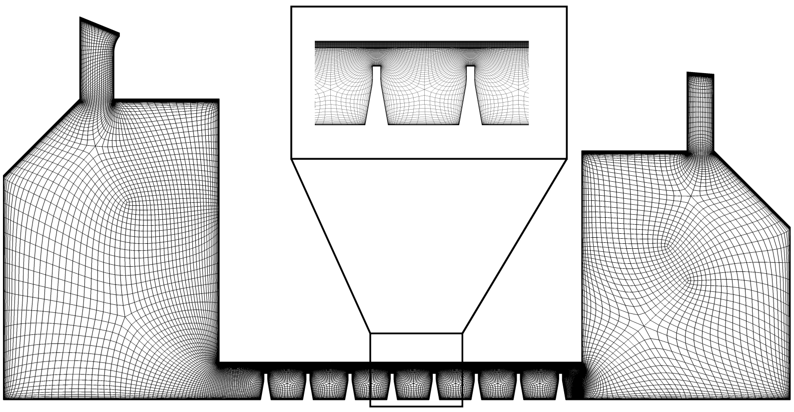

Figure 4.9: HSC, S8 cavity mesh

Figure 4.9 depicts the mesh of S8 cavity. At the interfaces between the cavity's upstream and downstream openings and the main path, the same cell width was used. The mesh used for the main path is the same as the one used for the cantilevered configuration, described in 4.2.

4.4 Simulation of the baseline cantilevered and the two shrouded configurations

In this section, three configurations of the entire 5.5-stage model are considered. They are the baseline cantilevered with nominal clearances, CNE, and the two shrouded configurations with different levels of clearance, SRE and SNE. SRE is the shrouded configuration with reduced clearances and SNE the shrouded configuration with nominal clearances. Indeed, due to the fact that shrouded stators require for mechanical reasons smaller clearances in comparison with cantilevered stators, the two reference configurations, CNE and SRE, have different clearances. However, also a shrouded design with the same clearances as the cantilevered is considered.

The aim of the study is to identify the regions of higher losses as well as to give further inside into the mechanism of loss generation and transmission in a multi-stage axial compressor configured both with cantilevered and with shrouded stators. Furthermore, for the shrouded design, it is investigated how the losses change when the clearance is increased. The stall behaviour is investigated for the two reference configurations to identify the causes of the stall when different stator hub designs are used.

4.4.1 Overall performance

The isentropic efficiency and the total absolute pressure ratio are shown in Figure 4.10 for the cantilevered configuration and the two shrouded configurations across the entire operational range. The points DP, TS, and NS represent the operating conditions design point, towards-stall point, and near-stall point, respectively. They are used in subsection 4.4.4 to analyse the stall behaviour.

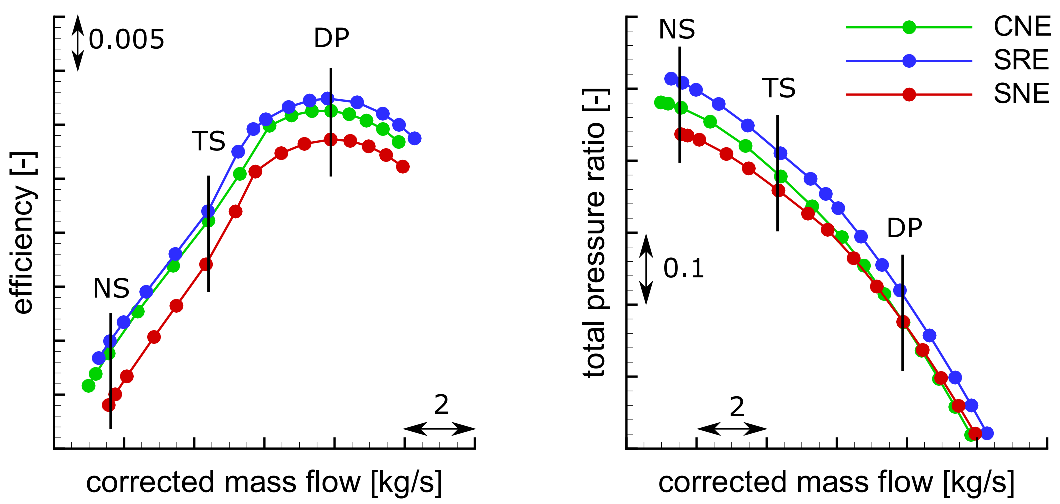

Figure 4.10: HSC, entire model, overall performance for the CNE, SRE and SNE configurations. DP, TS, and NS denote respectively the operating conditions design point, towards-stall point and near-stall point

The isentropic efficiency is defined as:

$$\eta = \frac{P_{ht,is}}{P_{ht}}, \tag{4.1}$$

where $P_{ht,is}$ is the power output calculated by assuming the process isentropic, and P_{ht} is the real power output. This formulation accounts correctly for the impact of the bleed flows, which is essential in this study because the position of S8 bleed is different for the cantilevered and for the shrouded configurations. Indeed, as shown in Figures 4.1 and 4.7, S8 bleed is located on the hub for the cantilevered configuration and in the cavity for the shrouded ones.

In Figure 4.10, we observe that the shrouded configuration with lower clearances, SRE, performs best across the entire operational range in terms of isentropic efficiency. In comparison, the cantilevered configuration, CNE, has lower performance, which is even more deteriorated for the shrouded configuration with nominal clearances, SNE. For all the configurations considered, the peak efficiency, i.e. the design point DP, is located at the same corrected mass flow. The stall margin of the CNE configuration is larger compared to the two shrouded configurations. Also, the stall margin of the shrouded configurations is adversely affected when the clearance level increases.

In terms of total pressure ratio, SRE has a higher total stagnation pressure ratio compared to SNE across the whole operational range. CNE has a total pressure ratio similar to SNE for large mass flows and between the two shrouded configurations for small mass flows.

4.4.2 Stage performance

The performance of each stage is shown in Figure 4.11. The local corrected mass flow is represented on the x-axis for each stage. For isentropic efficiency and total pressure ratio respectively, the same scales are used across the different stages.

At the DP operating conditions, the performance of CNE with respect to the two shrouded configurations varies from stage to stage. For stage 7, 9, and 10 CNE has an efficiency similar to SRE, whereas for stage 8, CNE has lower efficiency, even in comparison with SNE. This is a direct consequence of the bleed on stator 8, which is located at the hub for the cantilevered and on the cavity for the shrouded. Also for stage 11, CNE shows slightly lower efficiency in comparison to the two shrouded configurations. The aerofoil design of stage 11 remains unchanged for the 3 configurations and the changes in performance observed here are only a result of the different upstream flow field.

At the NS operating conditions, the relation of the efficiency level between the three configurations is unchanged for all the stages considered, except for stage 8. The isentropic efficiency of SRE is higher for each stage, whereas it is lower for SNE. Only for stage 8, SNE has higher isentropic efficiency than CNE.

The total pressure ratio of stage 7 shows an offset between the cantilevered configuration and the two shrouded configurations, which instead have a very similar total pressure ratio. Starting from stage 8, differences in terms of total pressure ratio between the two shrouded configurations are observed towards stall.

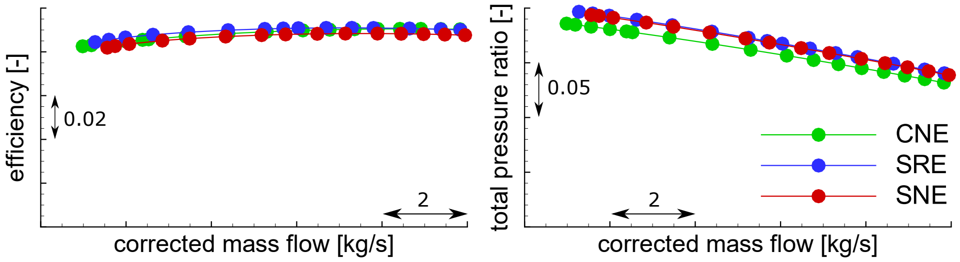

a) Stage 7

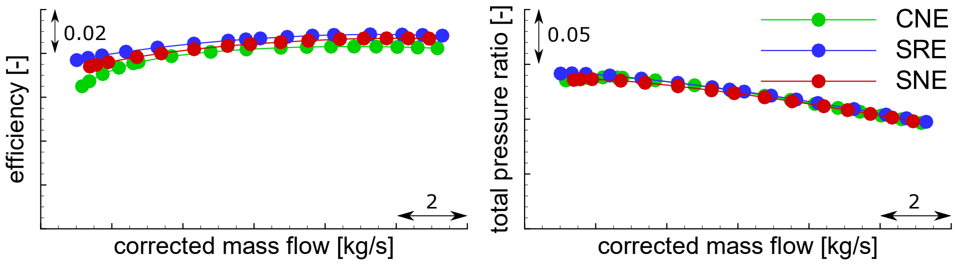

b) Stage 8

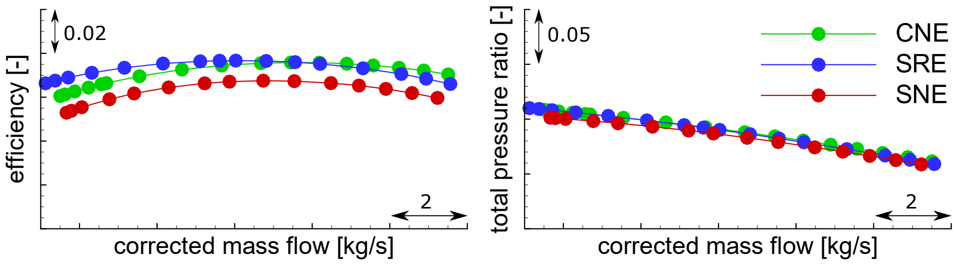

c) Stage 9

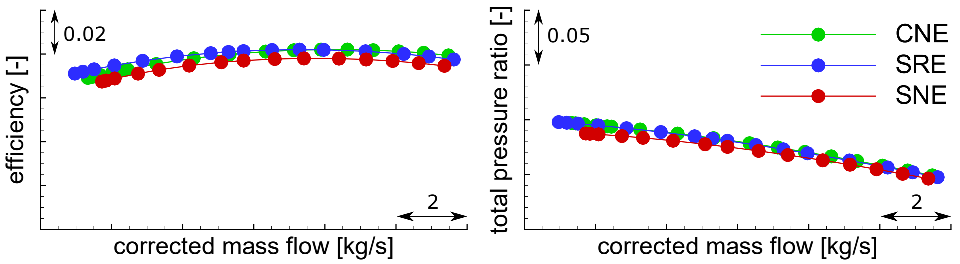

d) Stage 10

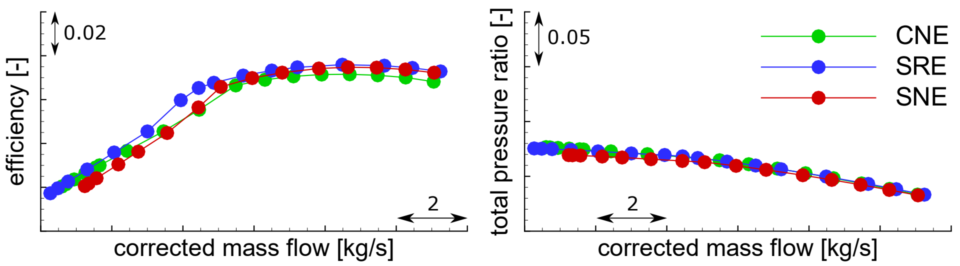

e) Stage 11

Figure 4.11: HSC, entire model, stage performance for the CNE, the SRE and SNE configurations

The analyses of the stage performance highlights that, for all the configurations considered, stage 8 and stage 11 are the weaker stages. Therefore in the subsection 4.4.4 these stages are investigated more in detail.

4.4.3 Design point analysis

The analysis goes more in detail by investigating the radial distribution of the losses for each row at the design point.

The choice of the most suitable definition of a loss coefficient is very important and, if chosen inadequately, may result in misleading conclusions as pointed out by

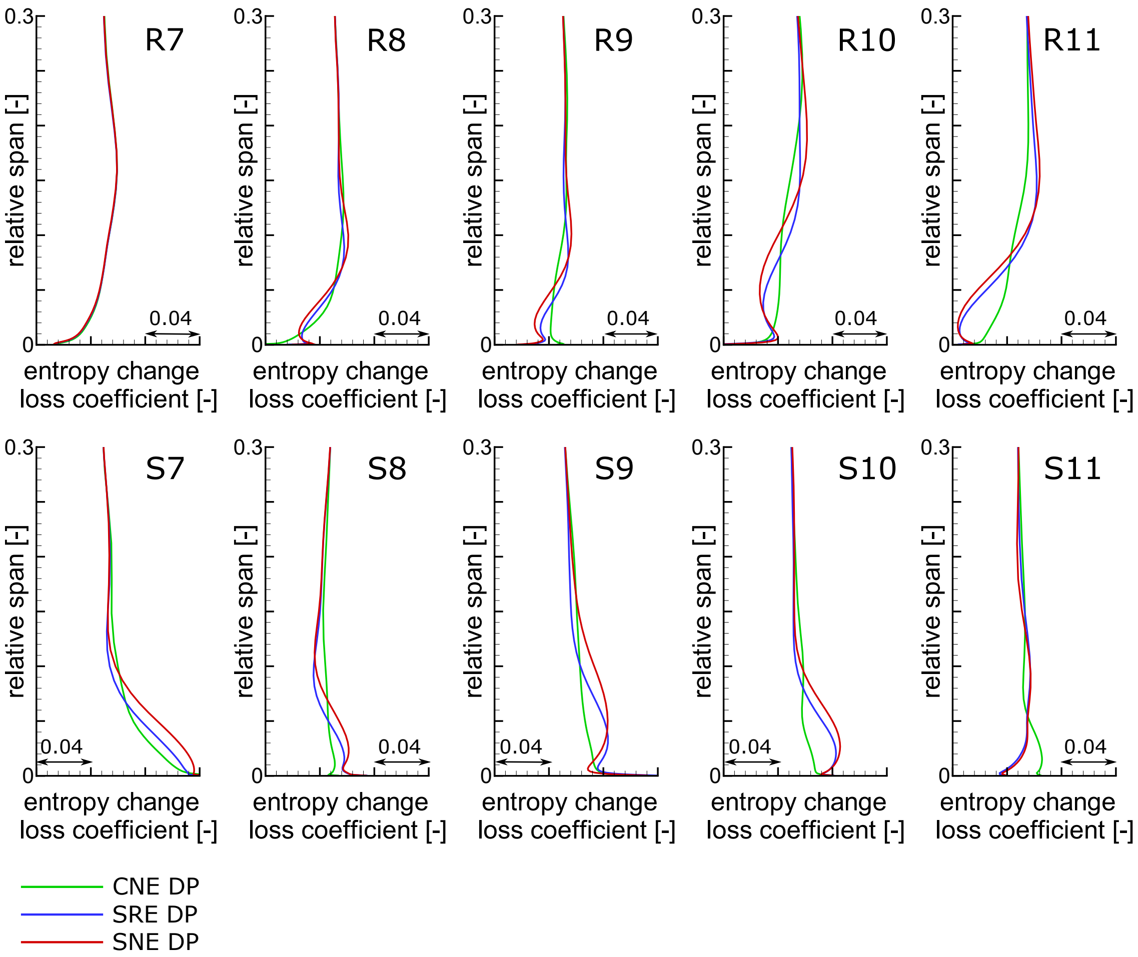

Figure 4.12: HSC, entire model, radial distributions of the entropy change loss coefficient at the DP operating conditions for the CNE, the SRE and SNE configurations

Yoon *et al.* [8]. De Dominicis *et al.* [51] have demonstrated that, in a multi-stage axial compressor featuring a change of stator hub configuration, the entropy loss coefficient defined by the Equation 2.2 should be used. The entropy change based loss coefficient takes into account the energy added by the rotating surfaces, which differs for the two stator hub configurations. The relative rotation between the stator and the hub imparts energy to the hub flow for the cantilevered stators, whereas the rotating inner leakage surface imparts energy to the seal cavity leakage flow for shrouded stators. The impact of the energy added by the rotating surfaces is different not only for the stator featuring a change of stator hub configurations but also for the downstream rows.

Figure 4.12 depicts radial distributions of the entropy change loss coefficient for each row at the design point. As the impact of the stator hub is limited to the inner 30% of the span, only this region is analysed. As expected, the flow field on R7 is only slightly affected by the redistribution induced by the downstream stator changes. The impact on S7 is, however, evident. S7 experiences a change of stator hub configuration, so the key feature causing the losses to be generated is different for the two stator designs. For the cantilevered case, the clearances vortex, which develops from the pressure side to the suction side of the vane in the gap between the rotating hub and the stationary stator, plays a major role. For the shrouded configurations, the leakage flow recirculates through the cavity, moving from the downstream opening to the upstream one, driven by the axial pressure difference across the stator. The leakage flow re-enters the main path upstream of the leading edge and, due to the low momentum of the leakage flow, generates a three-dimensional corner separation on the suction side of the vane.

Considering the loss distributions on S7, it emerges that only the lower 25% of the span is affected by the change of the stator hub configuration. In the comparison of the cantilevered design with the two shrouded ones, the entropy change loss coefficient indicates lower losses at the hub for the cantilevered stator configuration.

Since R8 is the first row downstream of S7, it is strongly affected by the upstream change of the stator hub configuration. Very close to the hub, i.e. between 1% and 6% of the span, the shrouded configurations show higher losses in comparison with CNE, and SNE has slightly lower losses than the one with reduced clearances. Between 6% and 11% of the span, the two shrouded configurations have higher losses with respect to the cantilevered, with SNE having larger ones.

For S8, the maximum value is, for CNE, lower than the one for the shrouded cases and is located at 1% of the span. In the region between 7% and 27% of the span, the entropy losses of the cantilevered design are slightly larger than those of both the two shrouded ones. The loss distributions of S8 are strongly impacted by the bleed, which is positioned at the hub for the cantilevered configuration and in the shroud cavity for the two shrouded configurations, as shown in Figure 4.1 and Figure 4.7, respectively.

Regarding stage 9, the R9 of the cantilevered configuration shows a different trend than the R8, R10, and R11. This is due to the bleed on the S8 hub, which has reduced the boundary layer at the S8 outlet, and hence also at the R9 inlet. For the shrouded configuration with higher clearances, the loss coefficients show great losses with respect to the other two configurations. On S9, the losses of the shrouded configurations are evidently higher than the cantilevered, with SNE showing larger losses, especially in the region between 5% and 19% of the span.

As a consequence of the upstream S9 flow field, the impact of the stator hub configuration on R10 is expanded over 30% of the span for the shrouded configuration with higher clearances. For S10, the losses of the two shrouded configurations are limited to 20% of the span, and are larger for the case with higher clearances.

Stage 11 is only indirectly affected by changes of stator hub configuration. The changes on S11 are only the consequences of the changes to the stator hub configurations in stators 7, 8, 9, and 10. For R11 the same considerations made for the other rotors apply, whereas for S11 the loss distributions are those typical of a cantilevered configuration. The impact of the upstream change in stator hub configuration appears in up to the 25% of the span. Close to the hub, the entropy change losses are consistently different for the cantilevered and the two shrouded configurations, although the stator hub configuration of S11 remains unchanged for the three configurations.

4.4.4 Near-stall analysis

To understand the stall mechanism of the investigated stage block, firstly the flow development that leads the machine towards the stall is considered. In this section, the stall behaviour of the two reference configurations, i.e CNE and SRE, is investigated, whereas the near-stall analysis for SNE is reported in appendix B. The main focus is to understand if and how the stators hub configuration affects the stall mechanism of the machine.

For each configuration, the stall analysis is conducted by considering the radial distributions of the entropy loss coefficient at three different corrected mass flows, which are the design point DP, towards-stall point TS, and near-stall point NS. Those points are highlighted in Figure 4.10. The regions found to be critical are then more deeply analysed through 3D plots, which show the reverse flow region and the entropy contours, downstream of the trailing edge of the blade/vane row under investigation.

4.4.4.1 Cantilevered configuration

Figure 4.13 depicts the radial distributions of the entropy change loss coefficient for each row of CNE at the three different corrected mass flow operating conditions DP, TS and NS, highlighted in Figure 4.10. Moving from the DP operating condition towards the stall, the region of increased losses is limited to the tip region for R7 and is found mostly in the hub region for S7. Starting with R8, instead, changes can be observed both at the hub and at the casing for all the rows when DP, TS, and NS are compared. R8 shows a very similar loss in the hub region for DP and TS, but a large increase of losses in the region between 16% and 36% of the span for NS. S8, close to the hub, has very similar losses for NS and TS, whereas, between 10% and 20% of the span, for NS shows larger losses transmitted downstream by the loss distributions on R8. As observed for the design point analysis in Figure 4.12, the bleed on S8 impacts the loss distributions of R9, as it reduces the boundary layer at S8 outlet. As a consequence, they show in the hub region a different trend in comparison with R8, R10 and R11.

For the rotors, the losses at TS and NS operating conditions compared with those at the DP, are lower close to the hub but larger moving towards midspan. In the tip region instead, the losses increase when the mass flow is decreased. For the stators, we observe an opposite trend. Compared with the losses at the DP, the losses at TS and NS, are lower close to the tip and larger in the hub region.

In general, by moving downstream, the losses become larger in terms of absolute value and more expansive across the span both for the rotors and the stators. In particular, S11 experiences a large region of losses in the hub region for TS and NS operating conditions in comparison with DP. It is extended up to 40% of the span at TS operating condition and up to midspan at NS operating condition. At TS and

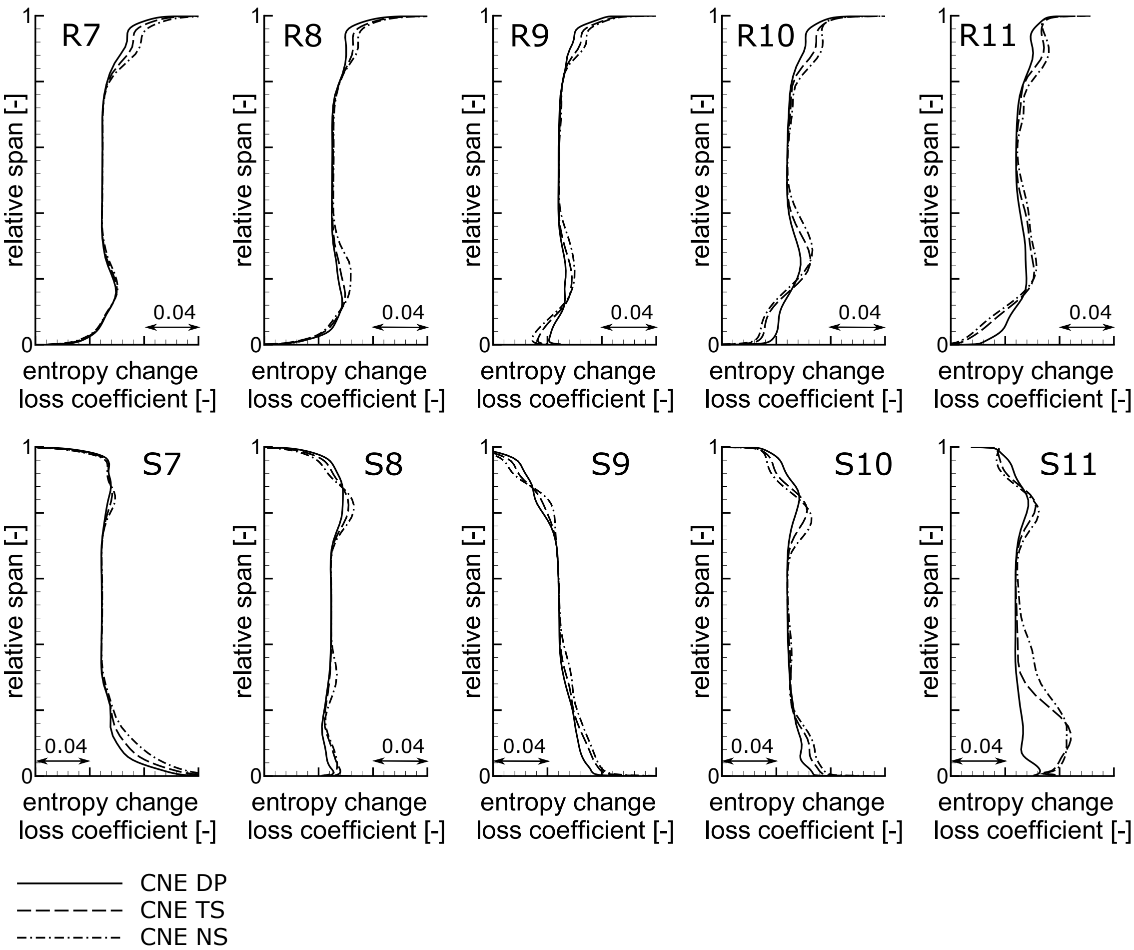

Figure 4.13: HSC, entire model, radial distributions of the entropy change loss coefficient at the operating conditions DP, TS and NS for the CNE configuration

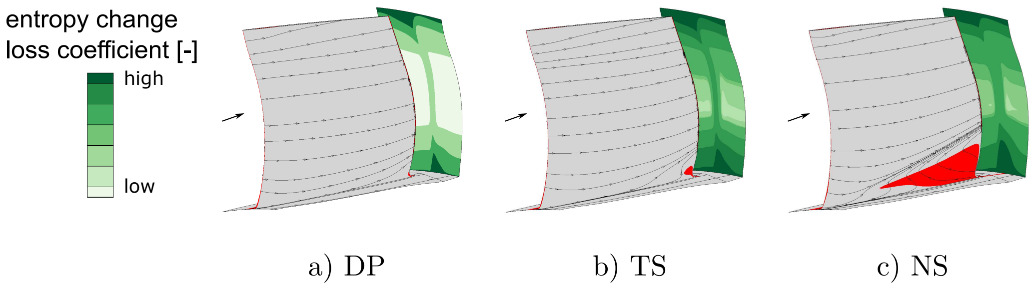

Figure 4.14: HSC, entire model, near-stall for the CNE configuration. The regions of negative axial velocity on R8 are depicted in red and the entropy contours downstream of the rotor trailing edge are depicted in green

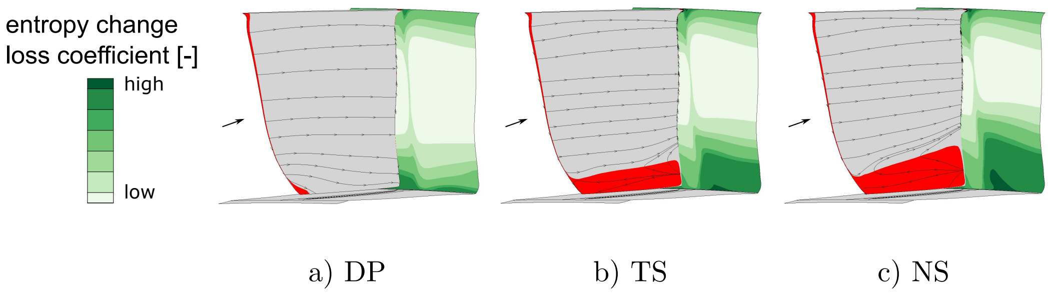

Figure 4.15: HSC, entire model, near-stall for the CNE configuration. The regions of negative axial velocity on S11 are depicted in red and the entropy contours downstream of the rotor trailing edge are depicted in green

NS operating conditions, the loss distributions of the entropy change loss coefficient reach, between 10% and 15% of the span, a similar maximum value.

The near-stall analysis is taken to more detail by investigating the causes of the increase of losses in the region between 16% and 36% of the span for R8, and in the hub region for S11, when the back pressure is increased. Figures 4.14 and 4.15 show the reverse flow region and the entropy contours downstream of the blade/vane row trailing edge, respectively, for R8 and S11, at the operating conditions DP, TS and NS.

In Figure 4.14 we observe a large reverse flow region in the hub region for R8 at NS operating condition. This reverse flow region cannot be observed at DP operating condition and is very limited at TS. This is in agreement with the trend observed in Figure 4.13 for the radial distributions of the entropy change loss coefficient, in which at DP and TS the loss distributions are very similar. Instead, at NS, R8 shows an increase of losses in the region between 16% and 36% of the span. However, the circumferential extension of the reverse flow region at NS, shown in the entropy contour plot, is limited. Therefore, the large region of reverse flow on R8 is not causing the numerical stall of the machine.

For S11, depicted in Figure 4.15, we observe a large region of reverse flow in the hub region for the operating conditions TS and NS, whereas at the DP operating condition it is very limited to the leading edge. At TS and NS, the reverse flow region affects the entire chord length. It causes the large increase of losses observed in Figure 4.13 and takes the machine to stall. This is confirmed by the entropy contour plots. Both at TS and NS, the region of reverse flow is extensively extended circumferentially.

4.4.4.2 Shrouded configuration with reduced clearances

Figure 4.16 depicts the radial distribution of the entropy change loss coefficient for each row of SRE at the three different corrected mass flow operating conditions DP, TS and NS highlighted in Figure 4.10.

When the compressor back pressure is increased from the DP operating condition to NS operating condition, the region of increased losses is mostly limited to the tip region for R7 and to the hub region for S7. This is in agreement with the observations made for CNE. Also for SRE, starting from R8, there are changes in losses both in the hub and in the tip region. Considering R8, we observe a relevant difference in the loss distribution between the shrouded and the cantilevered configuration. Indeed, R8 does not show a marked increase of losses in the hub region at NS. However, slightly higher losses are visible between 5% and 35% of the span for NS in comparison to DP and TS. This is a beneficial consequence of the altered inlet flow conditions for R8, resulting from the change of the S7 stator hub configuration from cantilevered to shrouded.

In the hub region, the change of stator hub configuration of the first four stators, from cantilevered to shrouded, results in different loss distributions, as discussed for the design point analysis in Figure 4.12. However, the same considerations made for CNE, when the mass flow is decreased, applies for SRE with the exception of S8 and R9. This is a consequence of the different location of S8 bleed for the cantilevered and the shrouded configuration. S8 bleed is located within the cavity for the shrouded configuration and directly at the hub main gas path contour for the cantilevered configuration. Therefore, when the two stator hub configurations are compared, it emerges, that for the shrouded configuration, S8 bleed not only has less effect on the loss distributions of S8 but also on those of the downstream row R9. It follows, that R9 loss distributions have a similar trend in comparison to the other rotors.

Similarly, as observed for CNE for the rotors, the losses at TS and NS operating conditions are, in comparison to the losses at the DP, lower close to the hub and larger

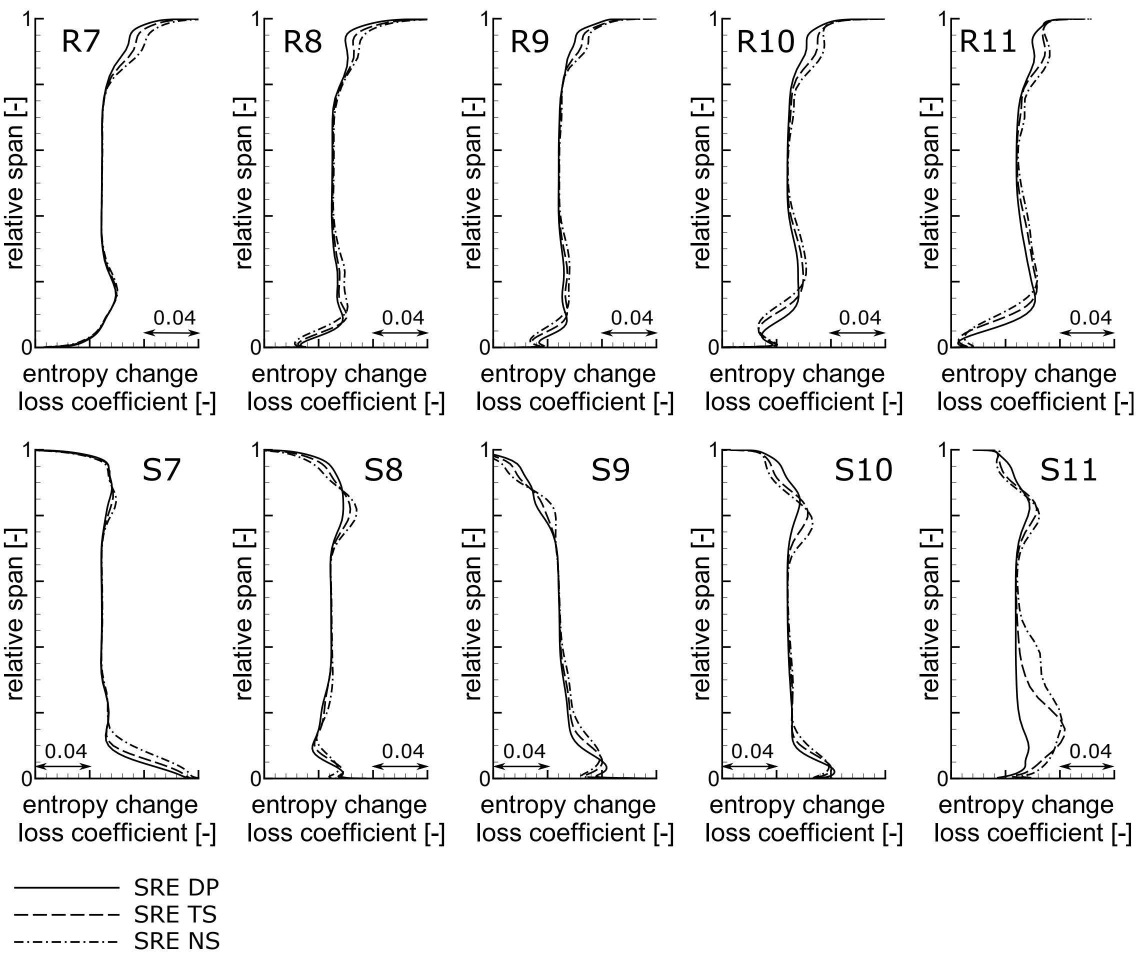

Figure 4.16: HSC, entire model, radial distributions of the entropy change loss coefficient at the operating conditions DP, TS and NS for the SRE configuration

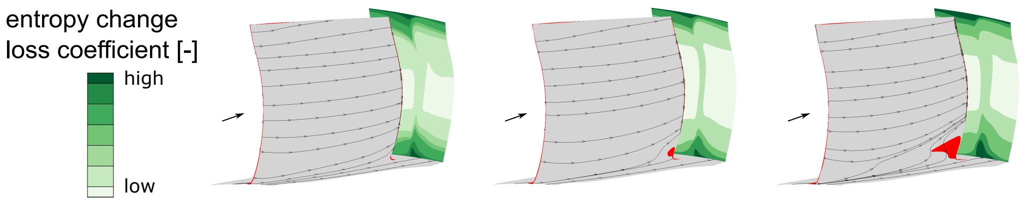

a) DP b) TS c) NS

Figure 4.17: HSC, entire model, near-stall for the SRE configuration. The regions of negative axial velocity on R8 are depicted in red and the entropy contours downstream of the rotor trailing edge are depicted in green

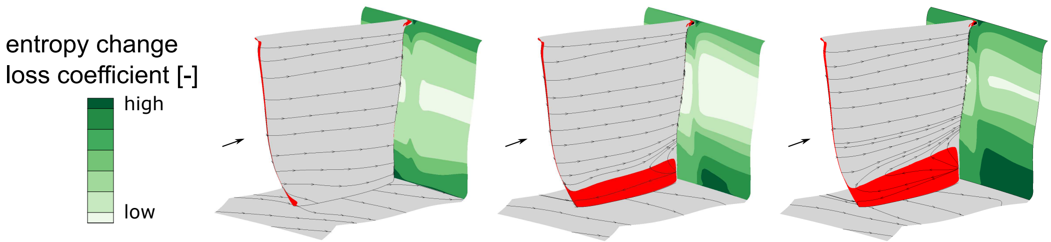

a) DP b) TS c) NS

Figure 4.18: HSC, entire model, near-stall for the SRE configuration. The regions of negative axial velocity on S11 are depicted in red and the entropy contours downstream of the rotor trailing edge are depicted in green

moving towards midspan. For the stators, the hub losses increase gradually when the mass flow is decreased. Conversely, at the tip, the losses increase gradually when the mass flow is decreased for the rotors, instead for the stators TS and NS result in lower losses close to the casing but higher losses towards midspan. The loss distributions at the tip show limited changes across the two stator hub configurations.

Also for the SRE configuration, by moving downstream, the level of entropy change loss coefficients become larger and losses are more expansive across the span both for the rotors and the stators. S11 losses increase drastically at the TS and NS conditions. Similarly as for CNE, the losses extend up to 40% of the span at TS operating condition and 50% of the span at the NS operating condition. The maximum value of losses is very close for both TS and NS operating conditions, and corresponds to the value of maximum loss for CNE.

With the aim to understand the reason for the reduced losses occurring on R8 and the causes of the large losses on S11, the respective regions of reverse flow and the entropy contours at the DP, TS and NS operating conditions are presented in Figure 4.17 and in Figure 4.18 for R8 and S11, respectively.

For R8, depicted in Figure 4.17, the region of reverse flow at the NS operating condition is drastically reduced compared to the one observed for CNE in Figure 4.14. At NS operating condition, the region of reverse flow is mostly limited in the trailing edge hub region and its circumferential extension is relatively small.

In Figure 4.18, S11 shows similar regions of reverse flow as those observed for the cantilevered configuration in Figure 4.15. Therefore, the change in stator hub configuration of the first 4 stators has not changed the stall behaviour of the machine. S11 is the row taking the machine to numerical stall, not only for the CNE configuration, but also for SRE.

4.4.5 Key Outcomes

In this section, the entire model compressor block was investigated, consisting of the last 5.5 stages of an 11-stage axial compressor. Starting from the baseline cantilevered configuration of the entire model, in which all the stators are configured as cantilevered and have the same level of hub clearance, the reference shrouded configuration was obtained by changing the stator hub design of the first four stators. The clearance level of the reference shrouded configuration is smaller than that of the baseline cantilevered configuration, because this general advantage of the shrouded approach was exploited here. Indeed, cantilevered stator vanes require relatively large hub-to-endwall clearances to avoid rubs and possible catastrophic damage, whereas shrouded stator vanes allow smaller seal clearances. However, a shrouded configuration with the same clearance level of the cantilevered configuration was also considered in this study.

For all the configurations investigated, the first four stators have the same clearance level and the clearances of the rotors as well as those of S11 and OGV were maintained unchanged. The stator aerofoil designs were left unchanged, apart from the thickness-to-chord ratio distribution, which is different for cantilevered and shrouded vanes. For the two shrouded configurations, the cavities were fully meshed and resolved. To physically account for the three bleeds, at S8, S9, and S11, the isentropic efficiency was formulated based on the output power.

The overall performance CFD prediction have shown, that the shrouded configuration with reduced clearances performs better in terms of efficiency. However, when the clearances were increased to match those of the cantilevered configuration, the shrouded design resulted in lower efficiency compared to the cantilevered one. In terms of stall margin, the cantilevered configuration shows a greater stall margin relative to the two shrouded configurations. Considering the individual stage performance, we have observed, that the better performing configuration changes from stage to stage, and the weaker stages are stages 8 and 11 for all three configurations.

The design point analysis, conducted using the entropy loss coefficient, has shown, that the two stator hub architectures, cantilevered and shrouded, result in a different distribution of the losses for all rows except R7. S7 is the first row upstream which experiences a change of stator hub configuration, therefore the impact on the upstream flow field of R7 is very limited. Instead, distinct changes in the loss distributions can be observed for S7 and the downstream rows. The changes are, however, limited to 30% of the span. In general, when moving downstream, the differences are larger in terms of absolute values and more expanded across the span both for the rotors and the stators. Although S11 is only indirectly affected by changing the upstream stator hub configurations and remains unchanged for the two configurations, also the loss distributions of S11 are consistently different for the cantilevered and the two shrouded configurations. The trend observed for the two shrouded configurations is similar, with the configuration with larger clearances showing larger losses.

The near-stall analysis of the two reference configurations, the cantilevered with nominal clearances and the shrouded with reduced clearances was conducted by considering the operating conditions DP, TS, and NS. It has shown, that for both configurations S11 has a large region of reverse flow at the hub for TS and NS operating conditions, which causes the machine to stall. Additionally, for the cantilevered configuration at NS a region of reverse flow on the R8 hub was observed, which is strongly reduced in the case of the shrouded configuration.

4.5 Sensitivity analysis

In this section, a parametric study is performed on a reduced model of the 5.5-stage axial compressor analysed in section 4.4 to quantify the impact of some significant parameters. Those are the clearance level of the first four stators for both the cantilevered and the shrouded configurations, the degree of reaction, and the endwall stator vane geometry, only investigated for the shrouded configuration. The results of this sensitivity study are used in section 4.6 to design two improved shrouded configurations.

4.5.1 Reduced model

Figure 4.19 shows the reduced model with shrouded stators investigated in this section of the work. It consists of stage 8, stage 9, and R10 of the shrouded baseline configuration presented in Figure 4.7. The inlet of the reduced model coincides with the mixing plane between S7 and R8 in the entire model, whereas the outlet of the reduced model coincides with the mixing plane between R10 and S10 of the entire model. Similarly, a reduced model for the cantilevered configuration was derived starting from the model shown in Figure 4.1. The inlet boundary conditions differ between the shrouded and the cantilevered configurations as they are derived by simulating the entire model using their individual stator hub designs.

The running clearances of rotors and stators used for the reference reduced models, shrouded and cantilevered, are the same as those used for the entire model. Nominal clearances, equal to approximately 1.5% of the S7 span are used for the reference cantilevered configuration, and reduced clearances, equal to approximately 1.1% of the S7 span, for the reference shrouded configuration. For each configuration considered, only the clearances of the stators has been changed, maintaining the

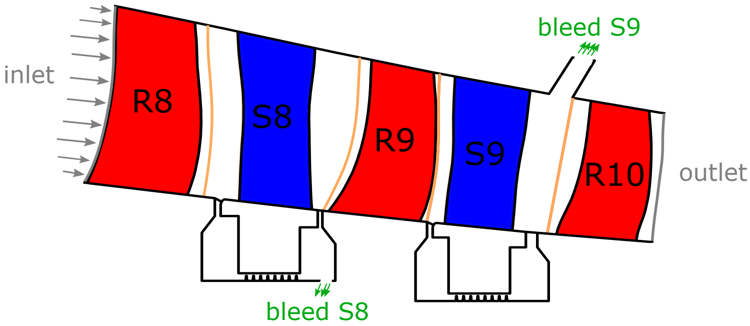

Figure 4.19: HSC, reduced shrouded model. The locations of the bleeds for S8, and S9 are shown in green, and the locations of the interfaces are depicted in orange

rotor clearances unchanged. The two stators have the same level of clearances for each configuration.

A reduced model was used to achieve faster results and speed up the design process. Indeed, the variations in the degree of reaction and the stator near-endwall profile geometry required an iterative process to maintain unchanged the pressure ratio and the incidence across the different configurations investigated.

4.5.2 Assessment of different hub clearances and seal gaps

Clearances play an essential role in determining the performance of an axial compressor. For multi-stage compressors, the impact of the clearances can be even more significant because the cumulative impact of leakage flow not only degrades the local performance, but also alters the stage matching intended by the designers. For rotor blades with normal operating clearances, a general rule is to expect a 1 to 1.5 point reduction in efficiency for every 1% increase in the clearance-to-height ratio [61, 5]. The stall margin can be reduced by up to 6% for every 1% increase in clearance-to-chord ratio [9]. The size of the clearances is not constant over time. It strongly depends on thermal effects and, during the lifespan of the machine, the clearance inevitability increases because of wear. Furthermore, the stages' loading affects aerofoil and seal erosion, with greater pressure differences promoting faster erosion [19]. Therefore, in the design phase of an axial compressor, the behavior of the machine over a range of reasonable clearance values needs to be investigated.

Avoiding the clearances is impossible; however, different kinds of designs have been developed resulting in different kinds of leakage flows [8]. Cantilevered stators require relatively large hub-to-endwall clearances to avoid rubs and possible catastrophic damage of the drum. Shrouded vanes, instead, allow smaller clearances, as the impact between the seal and the fins is not so dangerous as it would be for a cantilevered stator. Furthermore, in the recent years, different sealing technologies have been developed to reduce the amount of leakage flow [11] for shrouded configurations.

The focus of this section is to understand, whether increased stator clearances change the stall mechanism both for the cantilevered and the shrouded configuration.

4.5.2.1 Methodology

The clearance level of the two stators of the reduced model, i.e. S8 and S9, was systematically varied from small clearances to large ones. For each clearance level considered, both stators have the same absolute clearance value. The rotors clearances remained unchanged.

The study was performed both for the cantilevered and the shrouded configuration. Figure 2.1 depicts the aerofoil-clearance arrangement for the cantilevered and the shrouded designs.

Four different clearances are considered, representative of typical clearances used for axial compressors in stationary gas turbines. Table 4.4 summarises the different clearance levels investigated and the clearance-over-span τ/s for each stator. τ_{ref} is the nominal clearance and corresponds to the reference clearance for the cantilevered model.

Table 4.4: HSC, clearance study, stator tip levels considered

τ/τ_{ref}	τ/s S8	τ/s S9	Name	Abbreviation
0.70	0.0111	0.0127	Reduced clearances	R
1.00	0.0159	0.0182	Nominal clearances	N
1.43	0.0226	0.0260	Increased clearances	I
2.00	0.0317	0.0363	Large clearances	L

4.5.2.2 Overall performance

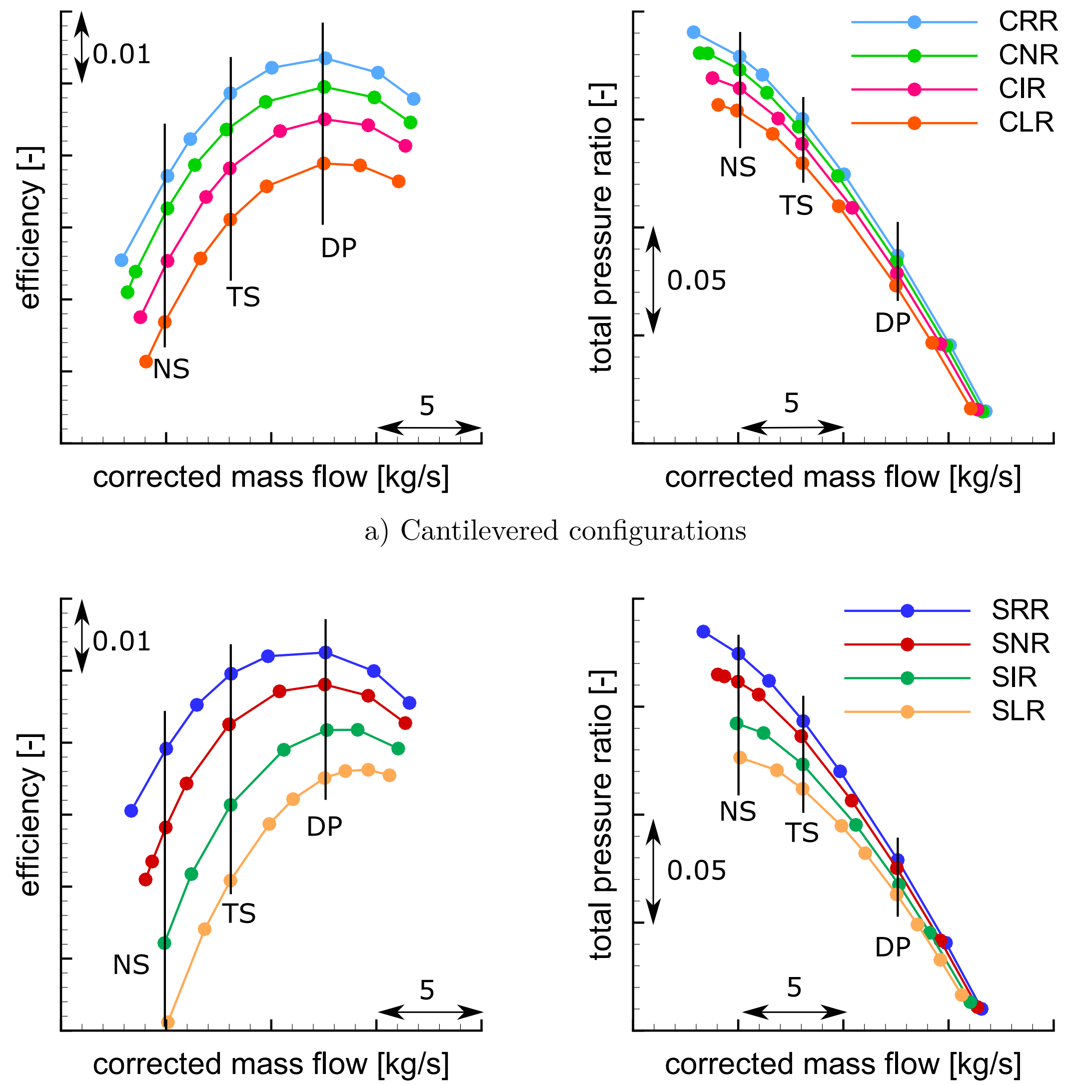

a) Cantilevered configurations

b) Shrouded configurations

Figure 4.20: HSC, clearance study, overall performance

Figure 4.20 shows the overall performance of the cantilevered and the shrouded configurations. The overall performance considers only stage 8 and stage 9, thus excluding R10.

We observe a clear trend of decreasing isentropic efficiency across the entire operational range when the stator clearances are increased, both for the shrouded and the cantilevered configurations. This trend was expected, as it was observed in many studies (e.g. [5], [19], [26]).

The peak efficiency remains at the same mass flow for the cantilevered configurations with varying clearances, whereas, when the clearances are altered for the shrouded configuration, the peak efficiency slightly shifts towards higher mass flow for larger clearances.

Considering the total pressure ratio, for high mass flow the impact of the clearances is very limited, both for the cantilevered and the shrouded configurations. When the clearances are increased, the total pressure ratio slightly drops. Moving toward smaller mass flows, the configurations with larger clearances results in a more pronunced reduction of total pressure ratio and in a reduction of stall margin.

Efficiency vs. clearance at the design point

The sensitivity of the isentropic efficiency to the clearances level at the design point is shown in Figure 4.21. The design point is highlighted in Figure 4.20.

For each of the clearances considered, the cantilevered configuration, C, has higher efficiency when compared with the shrouded one, S. However, to fairly compare the cantilevered and the shrouded design, a smaller clearance should be used for the

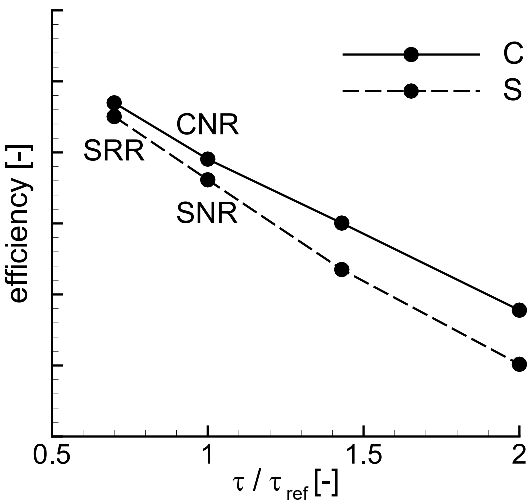

Figure 4.21: HSC, clearance study, isentropic efficiency vs. clearance levels for the cantilevered and the shrouded configurations

latter. Indeed, as pointed out in chapter 2, shrouded vanes allow reduced clearances in comparison with the cantilevered ones.

For reduced clearances, the two configurations have similar efficiency. When the clearances are increased, the shrouded design is more strongly impacted, showing a larger sensitivity to the clearance level than the cantilevered one. Consequently, to achieve the same efficiency of the cantilevered configuration with nominal clearances, smaller clearances are required for the shrouded configuration.

4.5.2.3 Cantilevered configuration

With the aim to deeply understand how the clearances affect the two different stator hub configurations, a more detailed analysis was performed. The analysis includes stage performance, design point and near-stall analysis of radial loss distributions.

Firstly, for the cantilevered design and then for the shrouded one, the reference and the larger clearances are considered. The larger clearances are the same for the two configurations, whereas the reference clearances correspond to the nominal clearances for the cantilevered configuration and to the reduced clearances for the shrouded configuration.

Stage performance

In Figure 4.22, the stage performance is shown for stages 8 and 9 by using the local mass flow and the same scale for the efficiency and for the total pressure ratio.

In general, for both stages, the trend is in agreement with the overall performance shown in Figure 4.20(a). Indeed, when the clearances are increased, we observe a decrease of the efficiency and a shift of the total pressure towards lower level. The reduced efficiency, despite larger for stage 9, can be observed in both stages, whereas the pressure shift mostly happen in stage 9. R9 is strongly affected by the upstream S8 change, whereas the impact on the upstream R8 is very limited. However, when the back pressure is increased to reach the stall, CLR shows an earlier roll-over

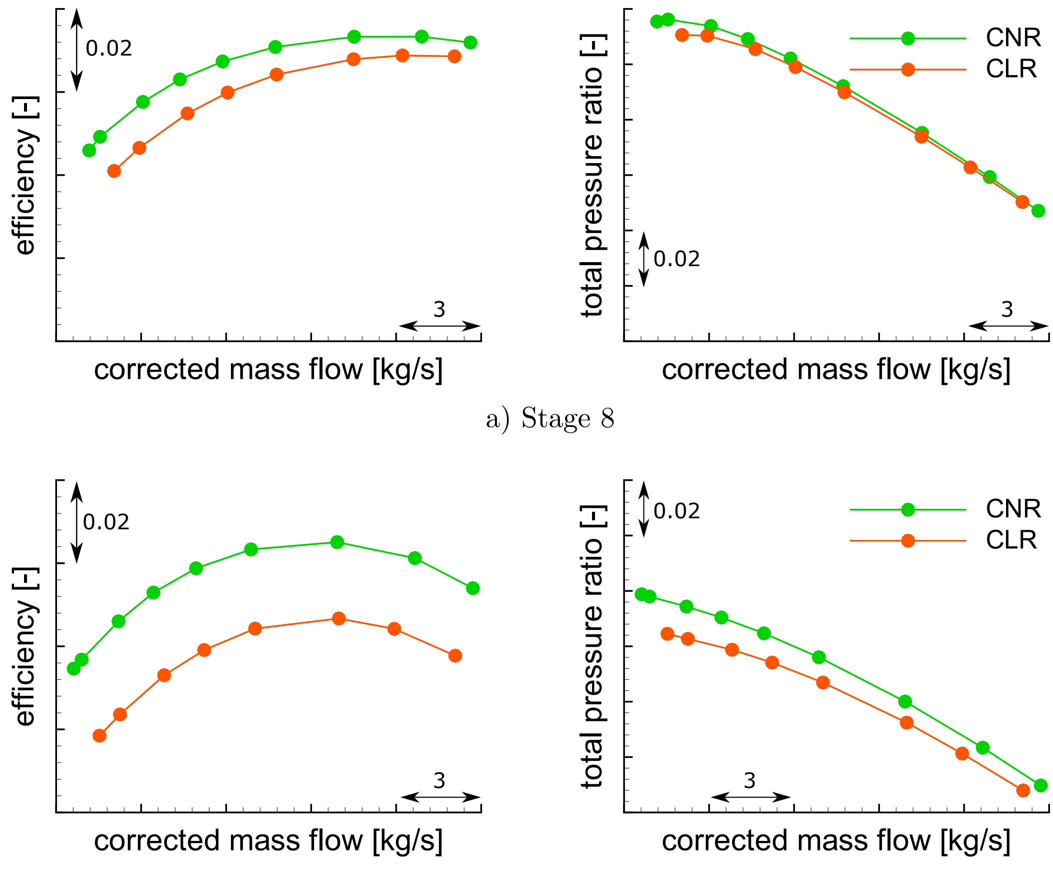

a) Stage 8

b) Stage 9

Figure 4.22: HSC, clearance study, stage performance of CNR and CLR

behavior of the characteristic, both for stage 8 and 9. The altered S8 clearance affects the stage 8 efficiency but, except for the near-stall region, has limited impact on the total pressure ratio. Stage 9 has both a reduced efficiency and a drop of total pressure ratio across the entire operational range.

Design point analysis

The radial distributions of the entropy change loss coefficient at the design point are depicted in Figure 4.23 for the CNR and CLR configurations. Only the lower 50% of the span is shown, the differences being limited in this region.

Comparing the distributions of the entropy change loss coefficient of the reduced cantilevered configuration with nominal clearances, CNR, with those of the enti-

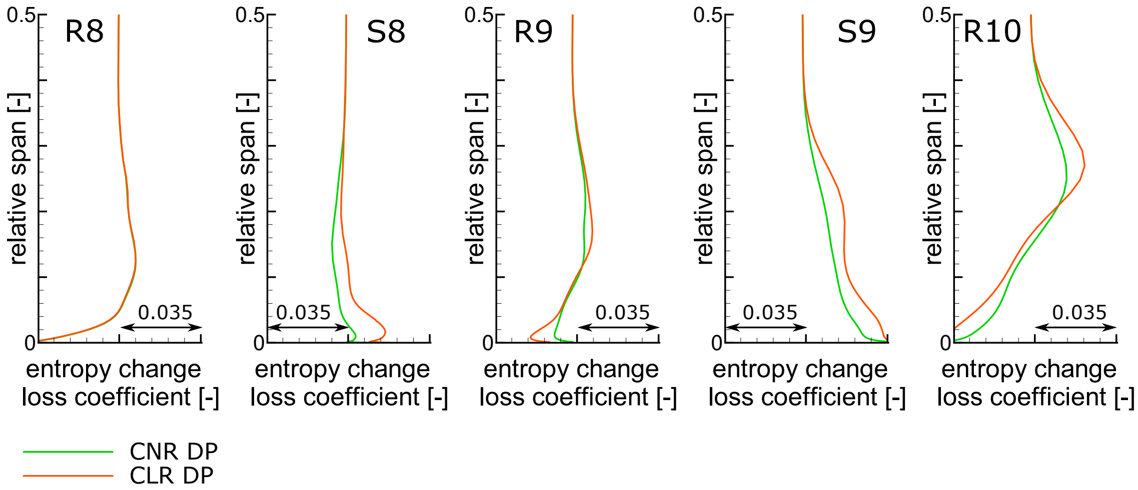

Figure 4.23: HSC, clearance study, radial distributions of the entropy change loss coefficient at the DP operating conditions for the CNR and CLR configurations

re cantilevered configuration with nominal clearances, CNE, which are depicted in Figure 4.12, we do not observe any significant difference. This was expected, because the boundary conditions imposed at R8 inlet to the reduced model were taken from the 5.5-stage model.

In Figure 4.23 we observe marked differences for all the row except R8 when the clearances are increased from the nominal to the larger ones. S8 and S9 show higher losses for CLR up to respectively 30% and 35% of the span. R9 and R10 have lower losses for CLR close the hub but larger losses toward midspan. In general, by moving downstream the differences between CNR and CLR are more expanded along the span, being up to 45% of the span for R10.

Near-stall analysis

To study the stall behavior of the machine, the DP, TS, and NS operating points, as shown in Figure 4.20, are firstly considered for the nominal and then for the large clearances.

Figure 4.24 depicts the the near-stall analysis for the CNR configuration. In comparison with the entire model, CNE, depicted in Figure 4.13, the reduced model

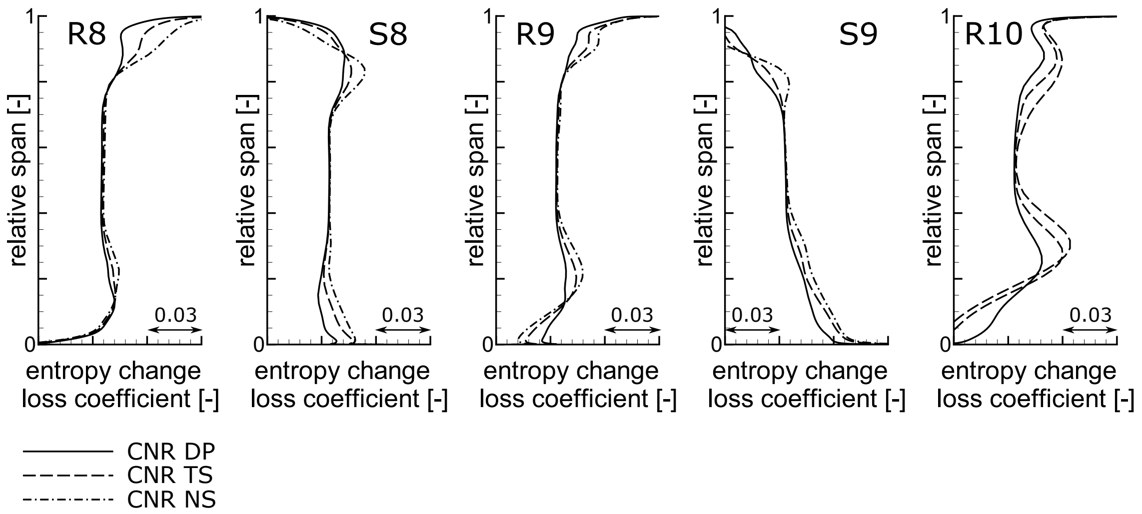

Figure 4.24: HSC, clearance study, radial distributions of the entropy change loss coefficient at the operating conditions DP, TS and NS for CNR

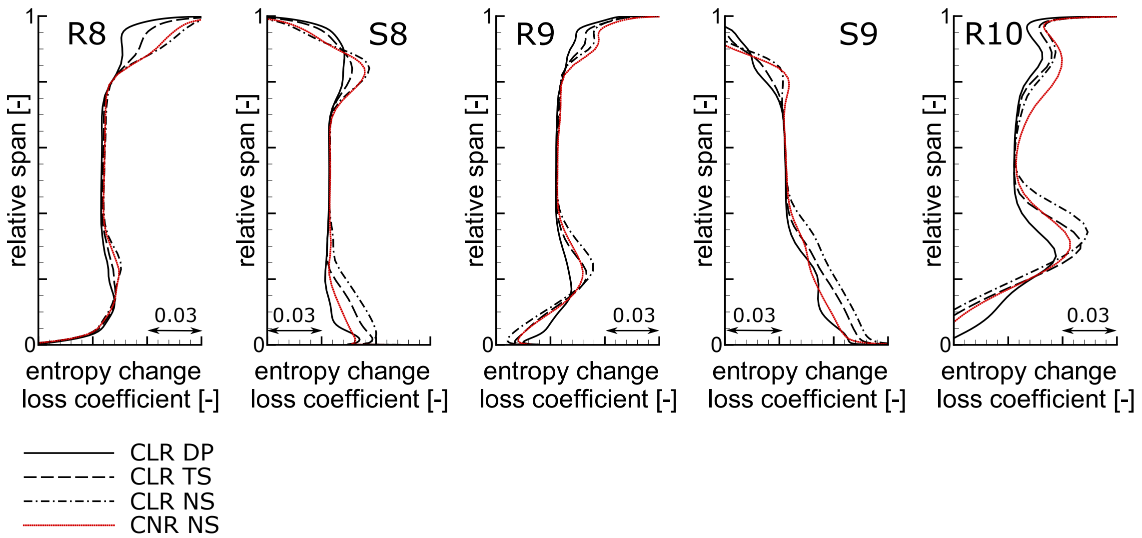

Figure 4.25: HSC, clearance study, radial distributions of the entropy change loss coefficient at the operating conditions DP, TS and NS for CLR and at the NS operating condition for CNR

shows marked differences in the rotors losses both at TS and NS, especially for R8 tip and R10, as a consequence of stages 8 and 9 being further throttled to search the stall regime for this shorted stage block. Indeed, considering the reduced model, the tip losses of R8 increase significantly when the back pressure is increased and, for R10, the maximum value of the losses at TS and NS is considerably larger and more expanded across the span. For the CNR configuration, R10 is the row driving the machine to stall.

Considering Figure 4.25, we observe for CLR a similar losses trend as the one observed for CNR, with the absolute value larger for the larger clearances. Also for CLR, R10 is causing the stall of the machine. The R8 and R9 tip losses increases, moving towards the stall, are for CLR similar to the one of CNR. This indicates that the total pressure bent observed for stage 8 and 9 for CLR, which indicates a earlier stall for CLR in comparison with CNR, is mainly driven by the larger losses on S8 and S9 respectively.

4.5.2.4 Shrouded configuration

The same analysis performed for the cantilevered configuration with two level of clearances is now conducted for the shrouded stator design. In this case, the reduced and the large clearances are considered. It has to be mentioned, that for the shrouded configurations the difference between the two clearances levels considered is larger than in the cantilevered study, which was based on the reduced and the nominal clearances.

Stage performance

The stage performance of the shrouded configurations for the two levels of clearances, SRR and SLR, is depicted in Figure 4.26 by using the local mass flow and the same scale for the efficiency and for the total pressure ratio respectively.

When the clearances are increased, similarly as observed for the cantilevered configuration, a decrease of efficiency can be observed for both stages 8 and 9, being significantly greater for stage 9. The total pressure drop on stage 8 is very limited, whereas it is marked for stage 9. At throttled operating conditions, the characteristics of the configuration with large clearances tends to roll over earlier both for stage 8 and, more evidently, for stage 9.

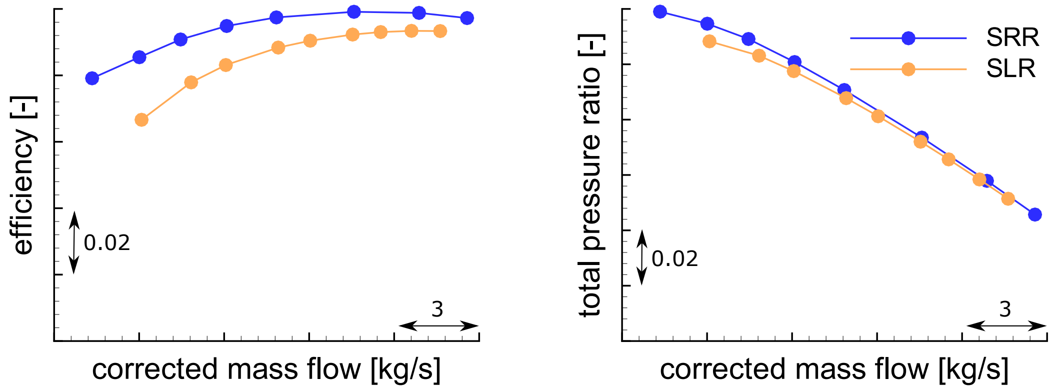

a) Stage 8

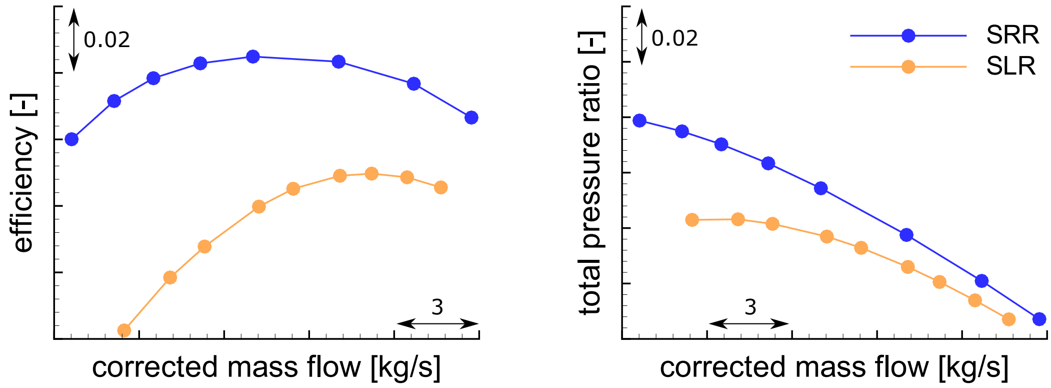

b) Stage 9

Figure 4.26: HSC, clearance study, stage performance of SRR and SLR

Performance deterioration with increasing clearances for the shrouded design were observed for the 5.5-stage configuration in Figure 4.11. However, for the entire model, the difference in clearance levels investigated were smaller, being the nominal and reduced clearances.

Design point analysis

Figure 4.27 shows the radial distributions of the entropy change loss coefficient at the design point for SRR and SLR in the lower 50% of the span.

For SRR, no visible differences can be observed between the reduced model and the 5.5-stage model, depicted in Figure 4.12. Large differences can instead be observed in Figure 4.27 between the SRR and SRL starting from S8. These differences are

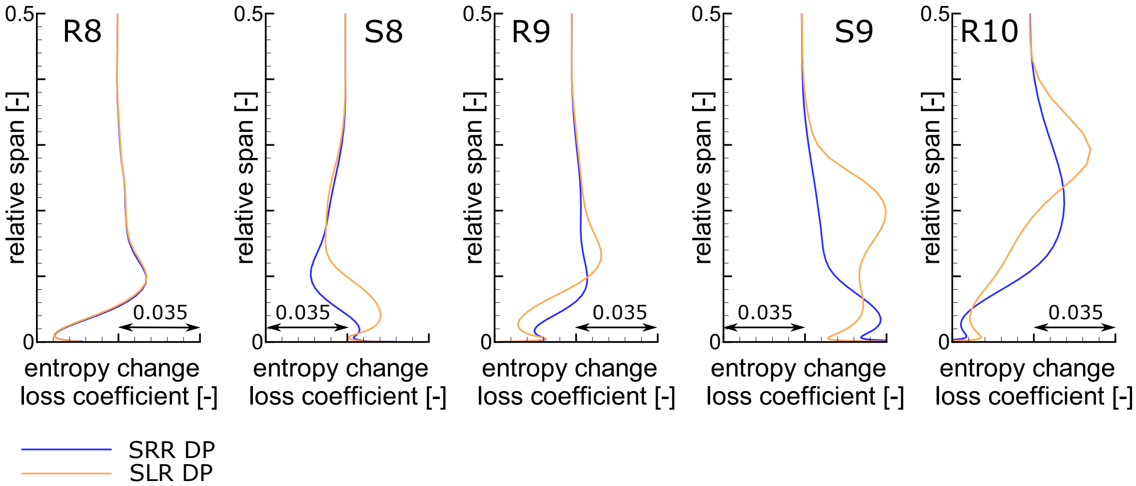

Figure 4.27: HSC, clearance study, radial distributions of the entropy change loss coefficient at the DP operating conditions for the SRR and SLR configurations

limited and close to the hub for S8 and R9, but relatively evident and extended across the span for S9 and R10. The large efficiency reduction observed in Figure 4.26 for stage 9 is therefore mostly caused by S9.

Near-stall analysis

In accordance with the near-stall study performed for the cantilevered configuration with two levels of clearances, the operating conditions DP, TS, and NS, shown in Figure 4.20, are also considered for the shrouded configuration, equipped firstly with reduced and then with large clearances.

Figure 4.28 depicts the stall analysis considering radial distributions of the entropy change loss coefficient, for the reduced shrouded configuration with reduced clearances, SRR. Although the trend is similar to the one observed in Figure 4.16 for the entire shrouded configuration with reduced clearances SRE, the reduced model shows greater losses moving toward the stall, especially at R8 tip and R10. This was also observed for the cantilevered configuration and is a consequence of stages 8 and 9 being further throttled to search the stall regime for this shorter stage block. The large losses on R10 at NS, extended across a huge portion of the span, indicate that R10 is the row taking the machine to stall for the reduced model. Therefore,

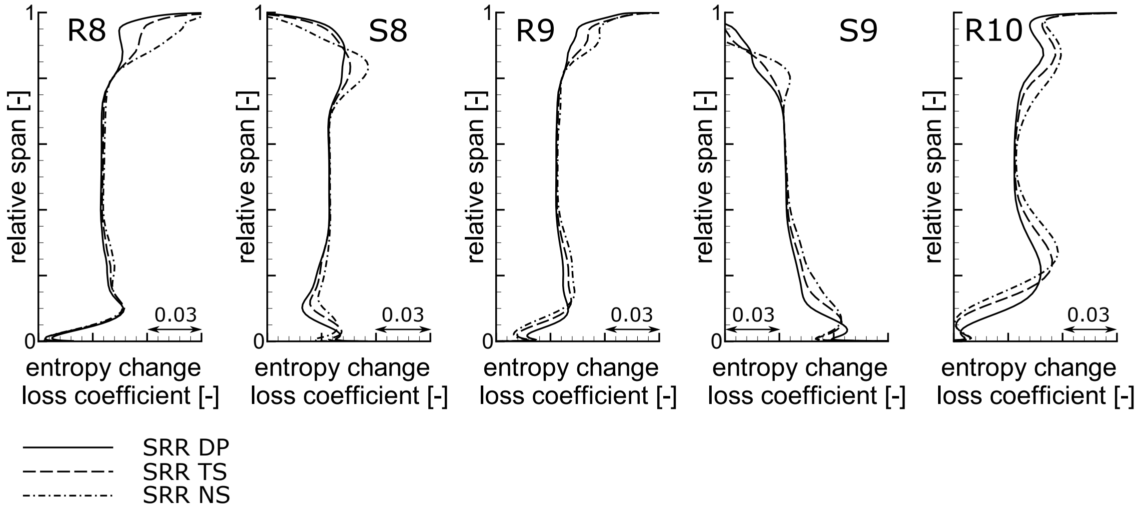

Figure 4.28: HSC, clearance study, radial distributions of the entropy change loss coefficient at the operating conditions DP, TS and NS for the SRR configuration

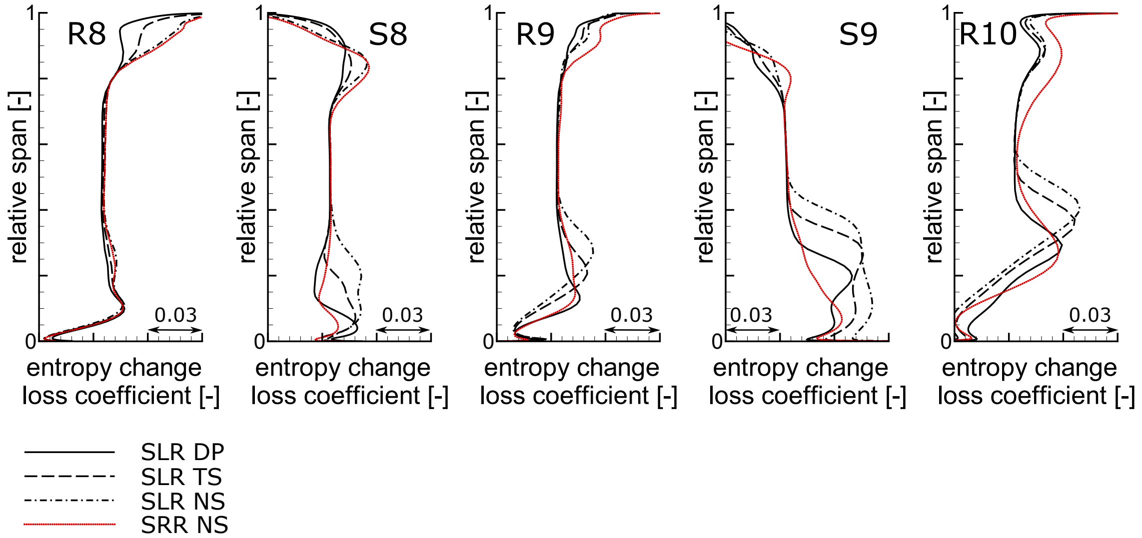

Figure 4.29: HSC, clearance study, radial distributions of the entropy change loss coefficient at the operating conditions DP, TS and NS for the SLR configuration and radial distributions of the entropy change loss coefficient at the NS operating condition for the SRR configuration

for CNR, CLR and SRR configurations, R10 is the row driving the machine to stall for the reduced model.

Comparing the stall mechanism of SLR, depicted in Figure 4.29, with SRR, depicted in Figure 4.28, we observe for all rows except R8 large differences in the trend of the losses. Indeed R8, being the first row upstream, is only slightly affected by the downstream stator changes. S8 hub losses are strongly increased for SLR already at the TS operating condition, however S9 is the row which presents the larger increase of losses when the back pressure is increased, thus causing the deteriorated performance observed for stage 9 in Figure 4.26. R10 presents large separations across most of the span, which are, in the lower 58% of the span, greater in comparison with SRR. Also for SLR, R10 drives the machine to stall. The reduced stall margin of SLR results from the very large region of high losses on S9.

4.5.3 Assessment of different degrees of reaction

The impact of the degree of reaction on the shrouded reduced model is analysed in this section. For a compressor stage, the degree of reaction is defined as the ratio of the rotor static enthalpy rise and the stage static enthalpy rise:

$$\Lambda = \frac{\Delta h_{rotor}}{\Delta h_{stage}}. \tag{4.2}$$

A low degree of reaction implies, that most of the static pressure rise occurs in the stator and, conversely, a high degree of reaction implies that little enthalpy change occurs in the stator and the majority takes place in the rotor.

The choice of the degree of reaction depends on constraints such as the compressor module's axis-symmetric inflow and outflow [3], [63]. A common approach is a degree of reaction of 50%, which results in an equal aerodynamic loading of rotor blade and stator vane. Furthermore a 50% degree of reaction means, that the rotors and stator aerofoils have a similar shape. However, the degree of reaction is not always a free design parameter.

Cumpsty [3] observed, that a change of the degree of reaction has a low impact on the stage efficiency but, as shown by Casey [63], the three-dimensional flow phenomena, such as the rotor tip leakage flow and the stator vane endwalls flow, were neglected in Cumpsty's study. Ortmanns [64] investigated the effects of changing the degree of reaction, including the three-dimensional phenomena for a conventionally loaded high pressure compressor stage. He showed, that the correlation between the overall stage efficiency at constant pressure ratio and the degree of stage reaction is low. Nevertheless, he observed, that the degree of reaction has a direct impact on the rotor tip leakage flow and the secondary flow phenomena in the stator endwall region, both driven by static pressure gradients within the respective rotor/stator passage.

In this section, the methodology used in this work to change the degree of reaction is first explained. Then, four different configurations with different degrees of reaction are considered.

4.5.3.1 Methodology

The design of the SNR configuration was varied to consider four different degrees of reaction. The SNR configuration is used as the original configuration for both the degree of reaction analysis and the stator near-endwall profile style modification, presented in section 4.5.4.

The original geometry of aerofoils corresponds to the baseline cantilevered configuration introduced in section 4.1 except for the thickness-to-chord ratio distribution, that was adapted to the new hub architecture as described in section 4.3.2.

The very first step in changing the degree of reaction was a preliminary assessment at the aerofoil midspan by using the velocity triangles. Starting from the SNR configuration, the stage inlet absolute angles were changed by a certain desired delta δ as shown in Figure 4.30. The four configurations with different degrees of reaction considered are presented in Table 4.5. They have the same design flow coefficient and work coefficient at the DP. The velocity triangles at the outlet of the rotors were calculated by imposing constant work across the rotors. The inlet axial velocity was kept unchanged for each row.

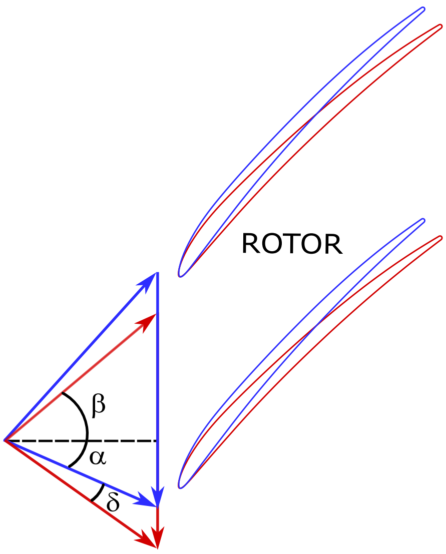

Figure 4.30: HSC, degree of reaction study, rotor inlet velocity triangles, original geometry depicted in red, new geometry depicted in blue

The preliminary assessment indicated how the metal angles of each row should be changed at midspan to achieve the desired swirl angles and consequently an altered degree of reaction. These results were then used as a starting point to change the geometry of the entire aerofoil. A tool-kit based on Matlab and Numeca Autoblade was used for this purpose [65]. The true chord length was maintained unchanged. The leading edge was the stacking point for both the rotors and the stators; however, the stator vanes were then translated to keep constant the axial location of the trailing edge. The decision to maintain the axial location of the stators' trailing edge was driven by the need to maintain the length of the stage (rotor + stator), in order to have comparable results across the different configurations. The lengths, that must be kept unchanged are shown in Figure 4.31: the distance A between the rotor TE and the mixing plan interface, the distance B between the downstream edge of the upstream axial cavity opening and the stator LE, and the distance C

Table 4.5: HSC, degree of reaction study, changes of stage inlet absolute angle considered

name	$\delta[°]$
SNR	0
DOR1	10
DOR2	5
DOR3	-5

between the upstream and the downstream upstream axial opening of the cavity. Other design parameters kept constant are the maximum thickness and the leading and trailing radii. Also the camber line, lean, and bow distributions were maintained. The geometry of the cavity was only altered in the x-direction.

The new CFD setup was prepared by adapting the inlet flow condition to stage 8. Indeed, for the first stage of the model, the inlet swirl angles were changed by modifying the inlet boundary conditions by the desired delta δ. R9 and R10 receive instead, as input, the exit flow of the previous stator, which was changed to obtain the desired swirl flow change δ.

To preserve the stage and rotor total pressure ratios, both integral and radial, as well as the incidence of all aerofoil sections, iterative corrections of the metal angle distributions were performed using 3D simulation. Indeed, the newly designed aerofoils are required to match the pressure ratio, both integral and radial, and the incidence of the starting configuration at the design point.

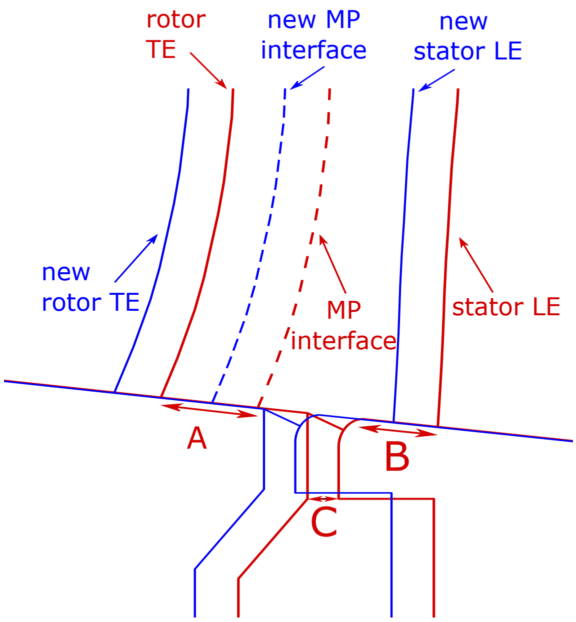

Figure 4.31: HSC, degree of reaction study, constant lengths when the degree of reaction is changed, original geometry depicted in red, new geometry depicted in blue

4.5.3.2 Geometry

The aerofoil geometries of stage 8 and the locations of the mixing planes are shown in Figure 4.32. The original configuration SNR is depicted in red.

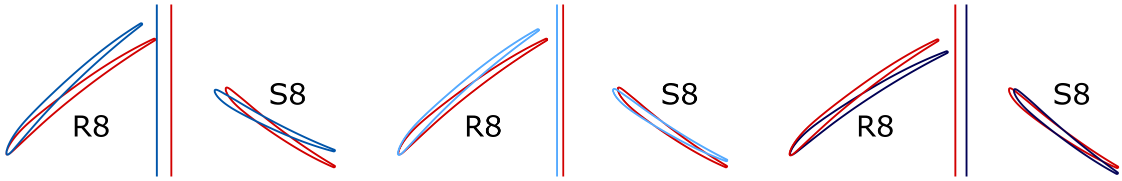

a) DOR1 b) DOR2 c) DOR3

Figure 4.32: HSC, degree of reaction study, stage 8 aerofoil geometries and mixing plane locations at midspan. The original geometry is depicted in red

The configurations DOR1 and DOR2 have a greater absolute inlet flow angle in comparison with SNR, whereas DOR3 has a smaller one. For DOR1 and DOR2, the larger absolute inlet flow angle results in a smaller rotor stagger angle. The rotor turning must increase to maintain the stage pressure ratio, thus the stator flow turning decreases. Oppositely, for DOR3, the smaller absolute inlet flow angle results in a higher rotor stagger angle and a smaller degree of flow turning on the rotor blade, resulting in a higher turning on the stator vane.

The change of the degree of reaction is not local, but instead affect the entire height, both for rotors and stators. For the rotors, an increased degree of reaction results in a larger static pressure rise.

4.5.3.3 Overall performance

Figure 4.33 shows the overall performance for the four different degrees of reaction, by considering only stage 8 and stage 9, thus excluding R10.

Observing the efficiency at the design point, DOR2 maintains the same efficiency as SNR, whereas DOR1 and DOR3 have distinctly lower efficiency, which is very similar. This trend is maintained moving towards the stall for all the configurations except for DOR1, which has a lower decrease in efficiency very close to stall in comparison to the other configurations. However, DOR1 stalls much earlier in comparison

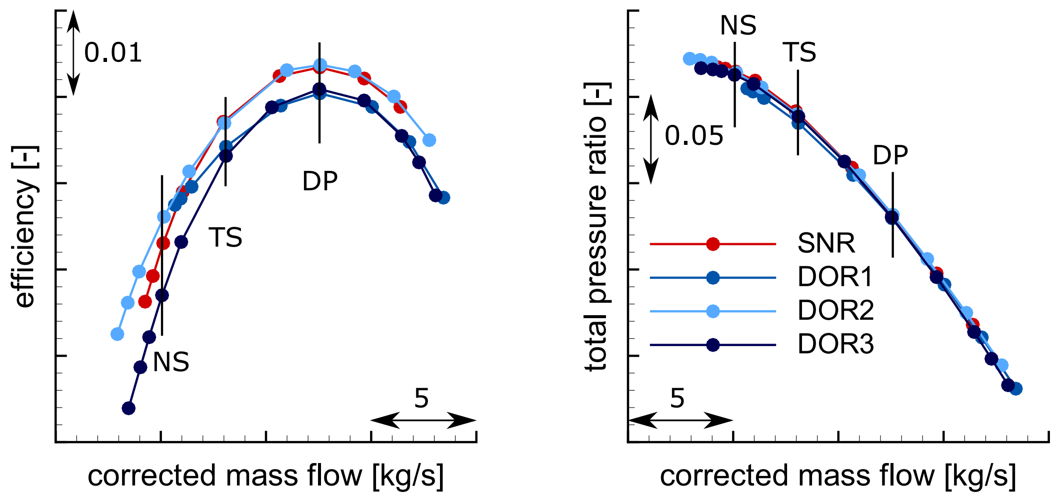

Figure 4.33: HSC, degree of reaction study, overall performance

with the other configurations. DOR2 is, at the near-stall operating conditions, the configuration with higher efficiency.

Both DOR2 and DOR3 show an increased stall margin of the machine, however DOR3 has lower efficiency across the entire operational range. Thus DOR2 results as the best configuration among the four investigated.

Considering the total pressure ratio, the four configurations show the intended same value at design point and only small differences towards the stall.

4.5.3.4 Stage performance

Figure 4.34 shows the performance of individual stages of the four configurations considered.

Both for stage 8 and stage 9, SNR and DOR2 perform similarly across the entire operational range, with DOR2 having slightly larger efficiency close to stall. There, DOR2 has lower total pressure ratio for stage 8, when compared with the SNR, but higher pressure ratio for stage 9.

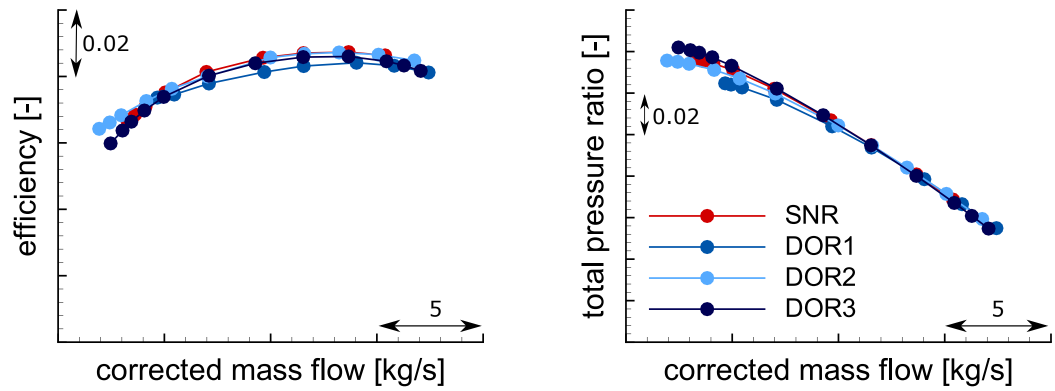

a) Stage 8

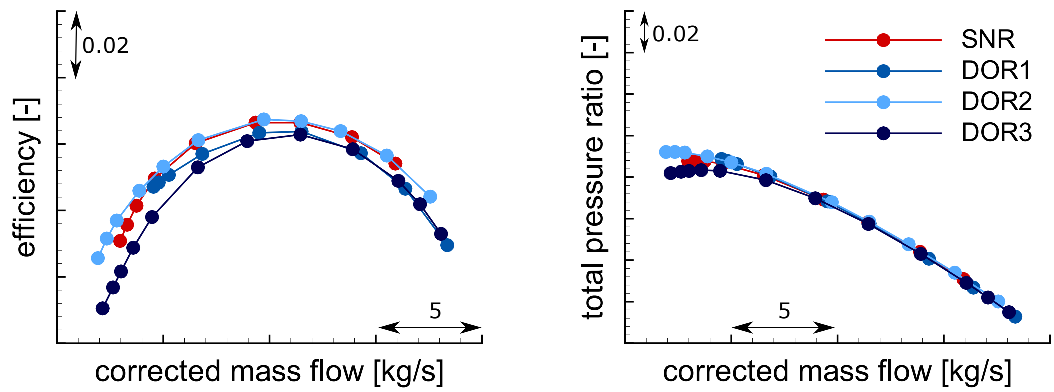

b) Stage 9

Figure 4.34: HSC, degree of reaction study, stage performance

DOR1 has reduced efficiency both for stage 8 and stage 9 and, for stage 8, has a different efficiency trend in comparison with the other configurations. DOR3 shows similar performance as SNR for stage 8, but lower efficiency and lower total pressure ratio for stage 9. This indicated, that the lower efficiency observed in the overall performance for DOR3, Figure 4.33, is mostly caused by deficits occurring is stage 9.

4.5.3.5 Design point analysis

At the design point, the four configurations are analysed in more depth. Table 4.6 tabulates the values of degree of reaction for each stage of the configurations investigated.

Table 4.6: HSC, degree of reaction study, values of configurations considered

	SNR	DOR1	DOR2	DOR3
Stage 8	0.54	0.65	0.60	0.46
Stage 9	0.47	0.62	0.54	0.39

Compared to SNR, DOR1 and DOR2 have for both stages a larger degree of reaction whereas DOR3 has reduced values. Although the change of stator exit flow angle has the same amount, but is opposite for DOR2 and DOR3, the variation of degree of reaction for both stage 8 and stage 9 is greater for DOR3.

Figure 4.35 shows the loss distributions across the span for each row for the four different degrees of reaction at the design point, which is marked in Figure 4.33. When the degree of reaction is increased, i.e. for DOR1 and DOR2, the tip losses increase for all the rotors while the stator hub losses decrease. Indeed a higher degree of reaction requires a higher enthalpy change across the rotors. In particular, R8 has a very large increase of losses related to the tip vortex for DOR1.

On the other hand, when the degree of reaction is decreased, i.e. for DOR3, the tip leakage losses decrease and the stator shroud leakage losses increase. A smaller

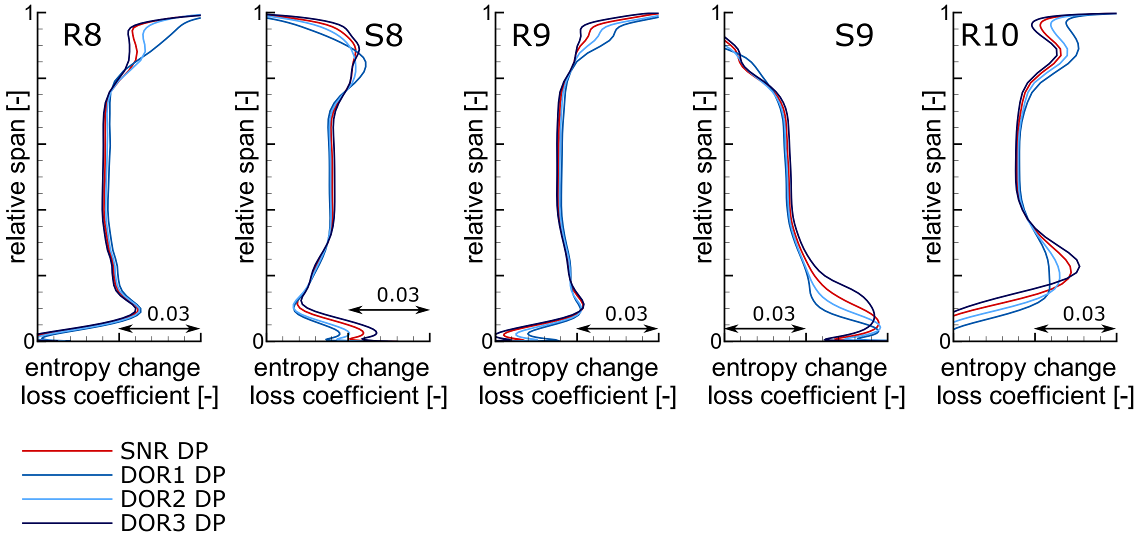

Figure 4.35: HSC, degree of reaction study, radial distribution of the entropy change loss coefficient at the DP operating conditions for the SNR, DOR1, DOR2, and DOR3 configurations

Configuration	R8	R9	R10
SNR	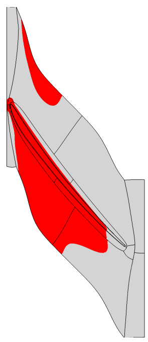	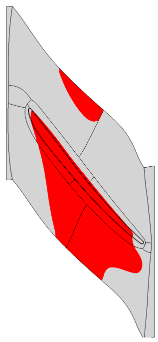	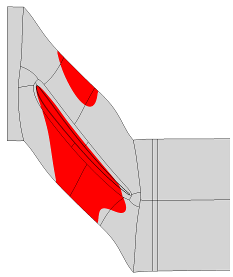
DOR1	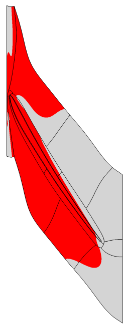	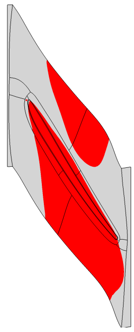	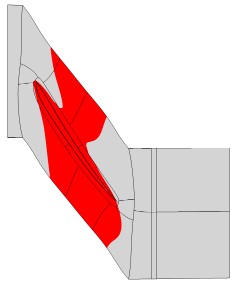
DOR2	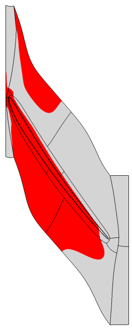	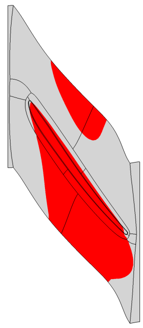	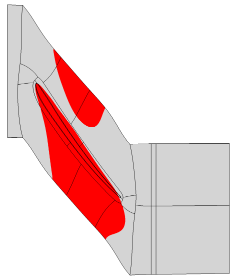
DOR3	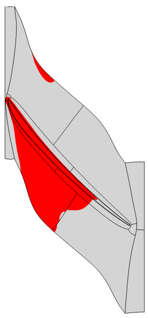	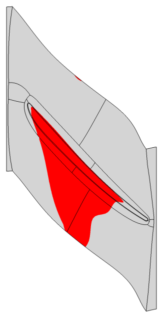	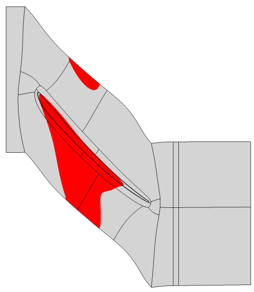

Figure 4.36: HSC, degree of reaction study, the regions of negative axial velocity at the mid-clearance height of the rotors for SNR, DOR1, DOR2 and DOR3 at the DP operating conditions are depicted in red

degree of reaction results in a larger static enthalpy change across the stator, thus larger static pressure difference between the upstream and the downstream axial opening of the inner shroud cavity. For S8 the increase of losses is however limited, whereas for S9 it is large.

These observations are in agreement with the regions of reverse flow at mid-clearance height of the rotors at the DP operating conditions, as shown in Figure 4.36, which depicts in red contours of negative axial velocity. Three-dimensional separation within the compressor can be identified and assessed when considering regions of low or negative axial velocity. This can be done in 2D or 3D views of the flow field, plotting contours of axial velocity, which identify reverse flow regions and therefore give evidence of potential flow separation occurring. In comparison with SNR, all the rotors of DOR1 and DOR2 have greater reverse flow patches, whereas those of DOR3 have smaller ones. For all the configurations, R9 is the rotor with smaller reverse flow patches at the tip in comparison with R8 and R10.

For DOR1 the regions of reverse flow are more expansive both in the axial and the circumferential directions. In particular, for R8, the reverse flow region includes a large portion of the inlet. This results in the large entropy change loss coefficients to be observed at R8 tip for DOR1 in Figure 4.35.

4.5.3.6 Near-stall analysis

The near-stall analysis is conducted for the original configuration, SNR, and the best degree of reaction configuration, DOR2, with the aim to better understand why DOR2 has a higher efficiency at the near-stall operating conditions and a larger stall margin compared with SNR. The results considered are the entropy change loss coefficient, the regions of reverse flow at the mid-clearance height of the rotors, and the regions of reverse flow and the entropy contours downstream of the stators' trailing edge at the operating conditions DP, TS and NS.

Figure 4.37 depicts, for SNR, the radial distributions of the entropy change loss coefficient for the DP, TS and NS highlighted in Figure 4.33. For all the rows, the trend is similar to the one seen in Figure 4.29 for the SLR configuration, even if the

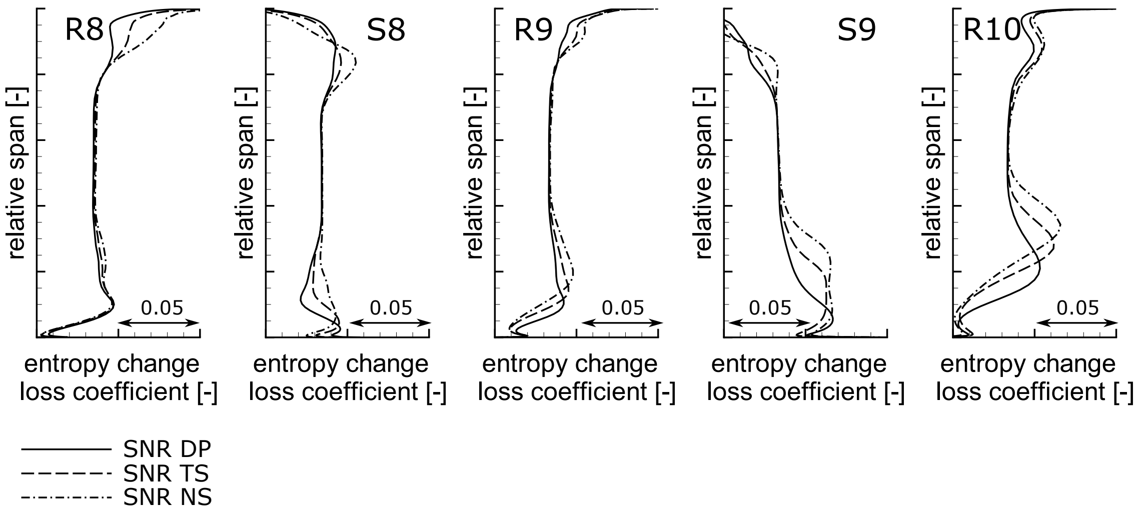

Figure 4.37: HSC, degree of reaction study, radial distribution of the entropy change loss coefficient at the operating conditions DP, TS and NS for the SNR configuration

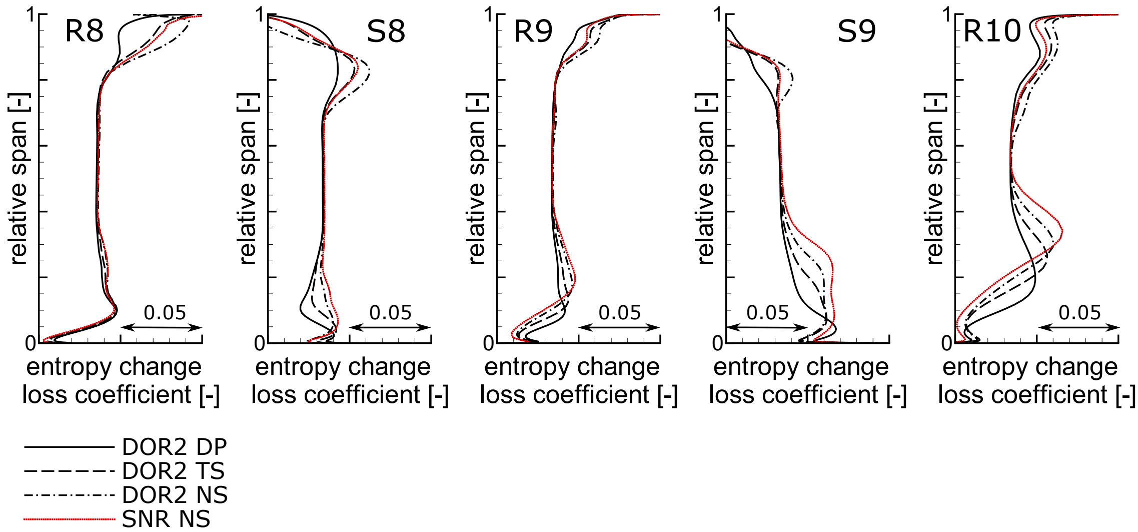

Figure 4.38: HSC, degree of reaction study, radial distributions of the entropy change loss coefficient at the operating conditions DP, TS and NS for the DOR2 configuration and at the NS operating condition for the SNR configuration

absolute values of the losses are lower for the configuration with nominal clearances, SNR. When the mass flow is decreased, the losses increase considerably on S9 and R10, thus taking the machine to stall. Also R8 tip losses are strongly affected by an increase of back pressure.

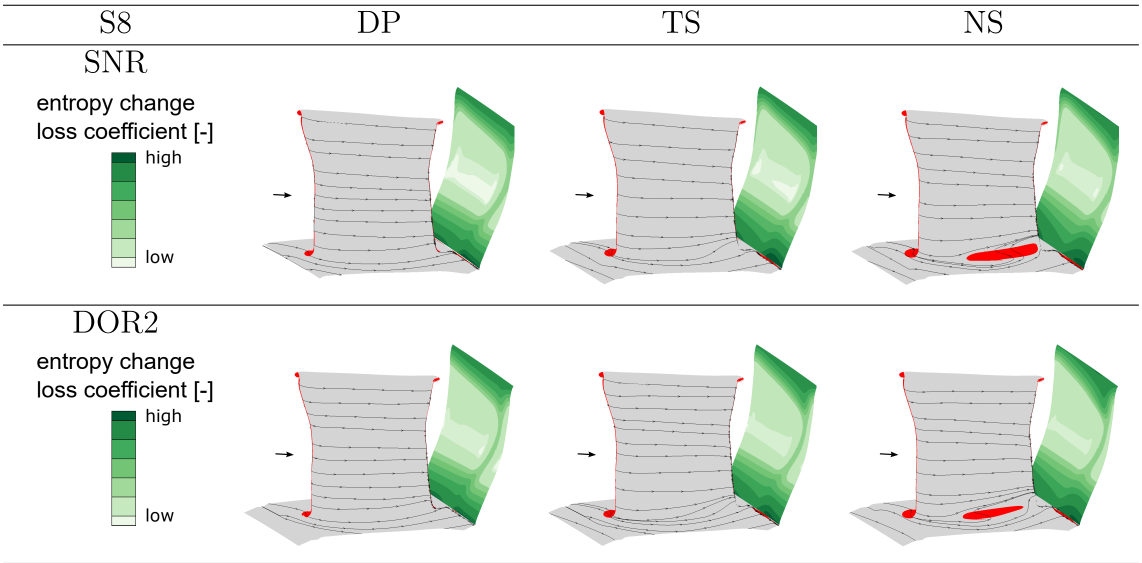

Figure 4.39: HSC, degree of reaction study, near-stall for the SNE and DOR2 configurations. The regions of negative axial velocity on S8 are depicted in red and the entropy contours downstream of the stator TE are depicted in green

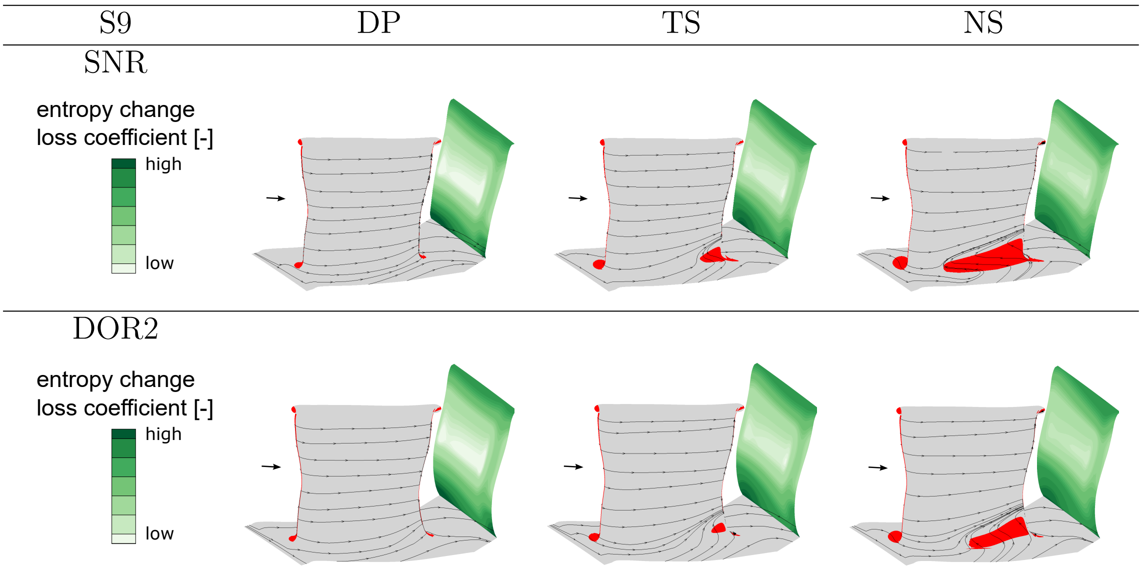

Figure 4.40: HSC, degree of reaction study, near-stall for the SNR and DOR2 configurations. The regions of negative axial velocity on S9 are depicted in red and the entropy contours downstream of the stator TE are depicted in green

Considering the entropy change loss coefficient at operating conditions the DP, TS and NS for DOR2 in Figure 4.38, a large increase of the tip losses can be observed when the mass flow is decreased in comparison with the SNR in particular for R8 and R10. In the tip region the losses of DOR2 at TS are similar to those observed for

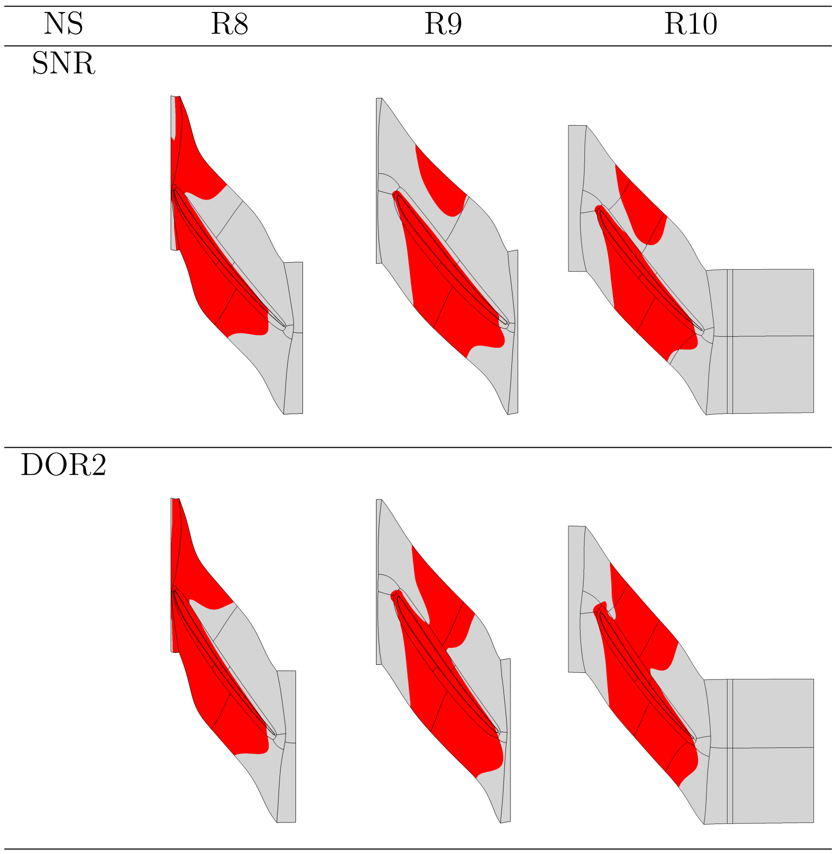

Figure 4.41: HSC, degree of reaction study, the regions of negative axial velocity at the mid-clearance height of the rotors for the SNR and DOR2 configurations at the NS operating conditions are depicted in red

SNR at NS. At the hub, S8 has only a smaller decrease of hub losses for DOR2 when compared with SNR, whereas S9 a considerable one. This decrease of hub losses on S9 delays the inception of the stall and results in a larger stall margin for DOR2.

The regions of reverse flow at the operational points DP, TS and NS on S8 and S9, are presented in Figures 4.39 and 4.40 respectively. For S8, we observe the positive impact of the increased degree of reaction only at NS where there is a reduction of the region of reverse flow for DOR2 in comparison with SNR. For S9, we see an improvement of the flow conditions already at the TS, where the endwall reverse flow region, despite limited for SNR, is smaller for DOR2. A strong improvement of the flow conditions in the hub region can be observed at NS for DOR2.

Figure 4.41 depicts the regions of reverse flow at the mid-clearance height of the rotors for the SNR and DOR2 configurations at the NS operating conditions. In agreement with the entropy change loss coefficient, we observe that when the mass flow is reduced, the reverse flow regions increase both in the axial and the circumferential directions. DOR2 has, for each rotor, increased regions of reverse flow when compared with SNR, and, similarly as observed in Figure 4.36 for the design point operating condition, also at the NS operating condition R9 is the rotor with smaller regions of reverse flow.

4.5.4 Assessment of different endwall profile styles

Aerofoil geometry specification is at the very heart of compressor design. The key aerofoil parameters are camber line, chord length, maximum thickness, leading and trailing edge radii, and thickness, lean, and bow distributions. The camber line distribution specifies the aerofoil geometry, as it describes the curvature and the chord-wise loading distribution of the profile. When designing a row of aerofoils, the aim is to achieve the desired turning with minimum loss and the greatest possible tolerance for incidence changes. Traditionally, the C-series or the NACA-65 series have been used in the specification of axial compressor aerofoils. As pointed out by Gallimore *et al.* [67], changing the chord-wise shape of the aerofoil sections has often been thought a way to affect the aerofoil lift distribution near endwall sections. There is indeed no doubt that profile re-design can affect the overall pressure field, but only when a significant part of the aerofoil is modified. Modifications concentrated more locally near the endwalls are likely to behave like endbends, i.e. the radial change in profile geometry is too rapid for the pressure field to adjust to the new aerofoil shape, and pressure remains mostly dictated by the mid-region, remote from the endwalls. However, Wisler [68] employed twist gradients in the stator endwall region, where vector diagrams were tailored to produce vane twist and to have a hub-strong total pressure profile produced by the rotors. This resulted in improved stator hub flow and overall compressor performance.

The improvement of the endwall performance by means of CDA section shape was first investigated by Behlke [69], showing that increasing the camber rate of the rear portion of an aerofoil can reduce the endwall losses. Wang *et al.* [70] improved the adiabatic efficiency and the total pressure of the NASA Rotor 37 by altering the camber line and thickness distributions.

More recently, Schrapp *et al.* [71] numerically investigated the efficiency influence of the camber line distribution at the rotor tip at different tip clearances in a 1.5 stage low-speed axial flow compressor. Starting from a baseline compressor, six designs were derived. For each design, the camber line at the tip section of the rotor was replaced by an analytically given camber distribution. The camber line designs ranged from extreme front load to extreme rear load. The camber line was changed at the rotor blade tip and blended into the original blade over the upper 30% of the blade height. The results indicated a slight correlation between the rotor tip camber line style and rotor losses. Additionally, the pressure increase, that occurs as the rotor tip vortex goes through the passage, remained generally unchanged with varying camber line styles.

In this section, the impact of the camber line style in the endwall region is systematically investigated by considering four different camber line styles[2]. For each camber line distribution considered, an analytical description of the geometry was imposed at the hub section and blended into the lower 30% of the span. For each configuration considered, the two stators were always modified using the same camber line distribution, whereas the rotors were maintained unchanged. The pressure ratio and the incidence of each aerofoil were kept constant across the different configurations. The effects of the camber line distribution on the overall performance, stage performance, and radial distributions as well as flow field details at the design and near-stall points were evaluated in detail.

4.5.4.1 Methodology

Figure 4.42 depicts the four alternative camber line styles employed at the hub section of the two stator vanes. As for the degree of reaction study in section 4.5.3, the original configuration is the shrouded with nominal clearance, called SNR. It is equipped with the reference camber line style, which is the typical front-loaded

[2]Part of the content of this section is based on the paper "Numerical Analysis of the Influence of Near-Endwall Camber Line Distribution on Leakage Losses of Axial Compressor Shrouded Stators", De Dominicis *et al.* [66], International Society for Air-Breathing Engines, 2022.

distribution where the majority of the flow turning along the chord happens in the first 20% of the chord length. In this section, the design changes were limited to the two stators, whereas the rotor blades are maintained unchanged.

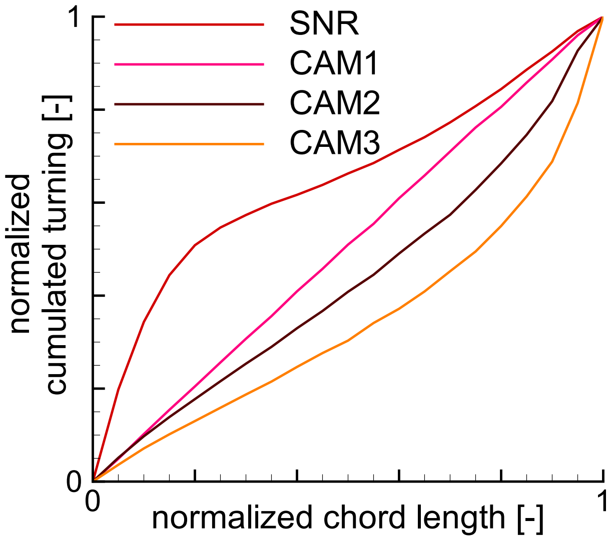

Figure 4.42: HSC, endwall profile study, camber line styles considered

The camber line distributions are defined by means of the following polynomial function:

$$g(m,x) = x * (x^m - x^{4m} + x^{3m}) \tag{4.3}$$

with a range of $x \in [0,1]$ and the parameter m varied to define the different camber lines. If the coefficient m is set to zero, the circular-arc distribution is obtained, which exhibits continuous turning of the flow. For $m > 0$ rear-loaded distributions are obtained, on which the majority of flow turning happens in the rear part of the section. Table 4.7 presents the coefficients used for each configuration considered.

Table 4.7: HSC, endwall profile study, camber line configurations considered

name	m
CAM1	0
CAM2	1
CAM3	2

To identify suitable camber line distributions, the tool MISES [72, 73] was used. MISES is a 2D blade-to-blade solver which allows designers to evaluate the aerodynamic performance of arbitrary aerofoil section geometries in a fast manner. Although the results of MISES simulations are limited to 2D flow and no secondary flow phenomena are taken into account, it is widely used in the aerofoil design process to design most of the sections of rotors and stators. A major benefit is the fast calculation time. Thus, the aim of this step is a preliminary assessment of the geometries rather than solving the 3D flow field in detail. This gives an insight into which camber line distributions are worth to be investigated though detailed and more time-consuming 3D RANS simulations.

Once the new camber line distribution was determined, a tool-kit based on Matlab and Numeca Autoblade was used to generate the new stator aerofoils. The desired camber line distribution was blended into the original aerofoil geometry over the lower 30% of the stator vane height, leaving the upper 70% of the stator unchanged. Indeed, after setting the new geometry parameters and distributions for the first section at the hub, the tool-kit for aerofoil design interpolated between the hub section and a specific section located at approximately 30% of the span, from which, further up, the original stator vane remained unchanged. The same section, section 9, was used for both stators 8 and 9. The new stator vane designs, with the changed near hub region, were then applied to the 2.5 stages of the compressor. The axial chord of all aerofoil sections was kept unchanged, and their stacking point was chosen to be the LE.

As for the degree of reaction study in section 4.5.3, an iterative process was performed to match the stage and rotor total pressure ratio, both integral and radial, and the incidence at the DP. The matching was achieved by modifying the stators exclusively. The trailing edge metal angles were adjusted in the lower 15% of the stator span and leading edge metal angles in the lower 30% of the span. The leading edge was modified in order to match the stator incidence, while the trailing edge was changed to match downstream rotor incidence. The thickness distribution was kept unchanged.

4.5.4.2 Geometry

For the different configurations considered in this section, Figure 4.43 depicts the geometry of the stator vanes at the hub sections for S8. The original geometry, which corresponds to the geometry of the reference shrouded configuration, or rather of the baseline cantilevered configuration introduced in section 4.1 with the adaptation of the thickness-to-chord ratio described in section 4.3.2, is shown in red.

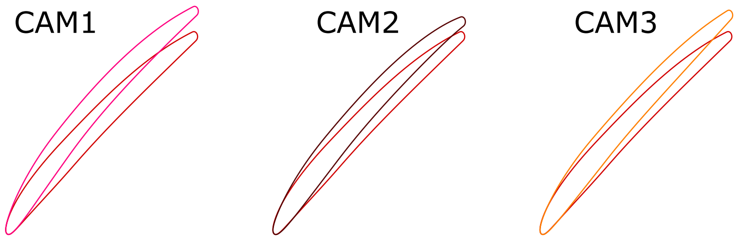

Figure 4.43: HSC, endwall profile study, sketch of the aerofoil geometries at the hub section. The original configuration SNR is shown in red

As the axial chord is kept constant, the true chord changes when different camber line styles are used. The changes are very limited close to the LE whereas they became evident moving towards the TE. Indeed, the camber line determines how the aerofoil is arched, i.e. how along the chord the turning is distributed. The camber line style has a strong impact on the aerofoil's sectional two-dimensional boundary layer and pressure distribution. All the new configurations move the loading to the rear, with CAM1 providing a continuous turning of the flow along the chord and, CAM2 and CAM3 having the majority of flow turning happening in the rear part of the aerofoil section.

4.5.4.3 Overall performance

Figure 4.44 shows the overall performance resulting from the different stator endwall camber line distributions. The performance was only predicted considering stage 8 and stage 9, but excluding R10. The position of the DP, TS and NS are highlighted. These points are used in the section 4.5.4.6 for the near-stall analysis.

At the design point, hardly any change can be observed in terms of both efficiency and total pressure ratio comparing the different configurations. Instead, moving toward the stall, all the new configurations bear a gain in efficiency in comparison to SNR. Among them, CAM1 is the configuration performing better.

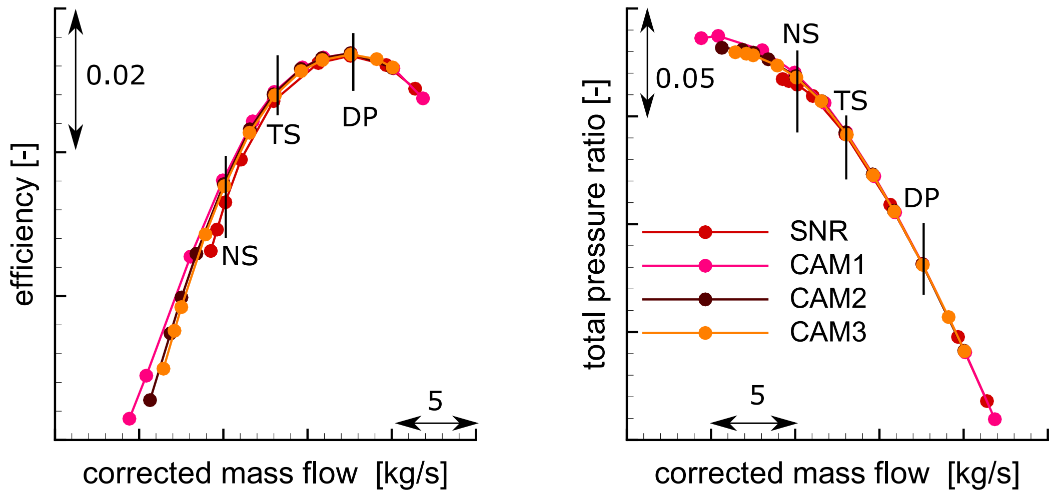

Figure 4.44: HSC, endwall profile study, overall performance

The stall margin of SNR is smaller than on all the other configurations investigated. However, the stator vanes of SNR were originally designed for a cantilevered configuration, therefore the endwall geometry was not optimised for the shrouded hub configuration.

4.5.4.4 Stage performance

The stage performance, depicted in Figure 4.45, shows a trend very similar to the one observed for the overall performance in Figure 4.44. The performance at the design point is very similar for all the configurations considered, whereas, moving towards the stall, the newly designed configurations perform better than the original one both in terms of efficiency and total pressure ratio. Despite both stages follow this trend, the beneficial effect of the new endwall sections are more visibly on stage 9. Stage 9 not only has a new stator vane geometry, but it is also affected by the upstream change of the S8 vane geometry. However, for stage 9, a very limited performance improvement can be observed at the DP.

Both for stage 8 and stage 9, CAM1 performs better in comparison with all the other configurations investigated.

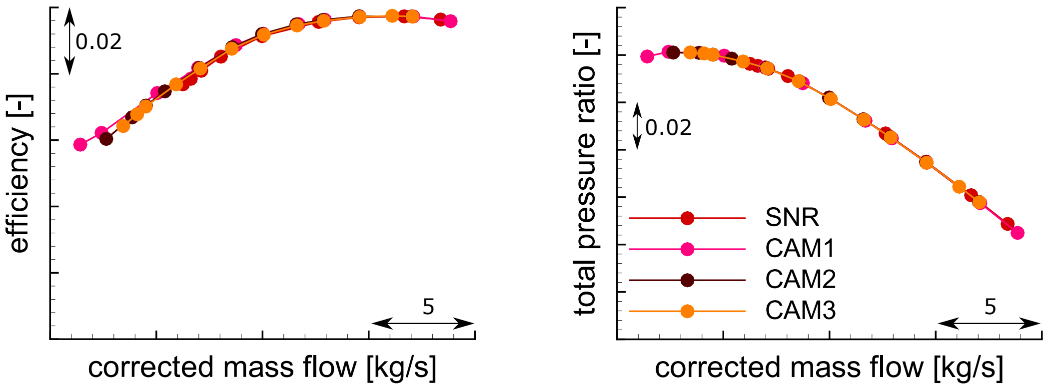

a) Stage 8

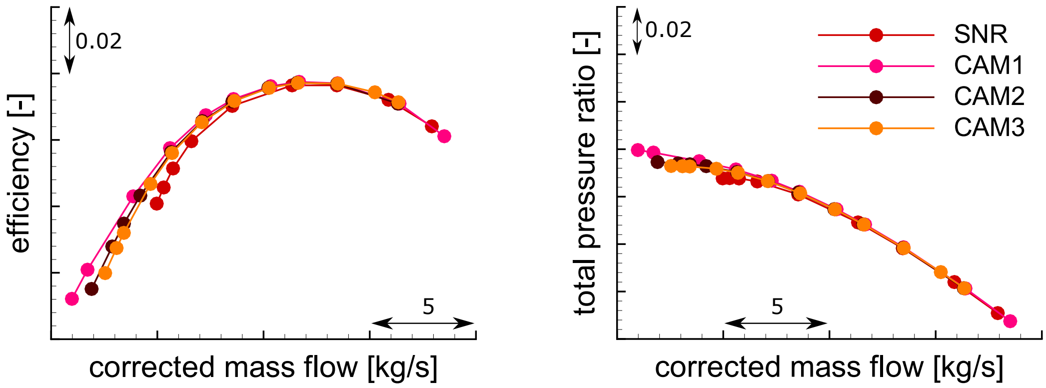

b) Stage 9

Figure 4.45: HSC, endwall profile study, stage performance

4.5.4.5 Design point analysis

The radial distributions of the entropy change loss coefficient are presented in Figure 4.46 for the four configurations with different camber line styles considered.

In general, both for the rotors and the stators, a very similar trend is observed in the hub region for all the configurations. However, some small differences such as the lower losses of the newly designed configurations for S9, between 3% and 10% of the span and the loss increase on R10 in the lower 10% of the span can be observed.

Considering the profile isentropic Mach number distributions on the stators at 5%, 20% and 50% of the span at the design point, depicted in Figure 4.47, we see local changes. Indeed, having maintained the metal angles unchanged, the effective inci-

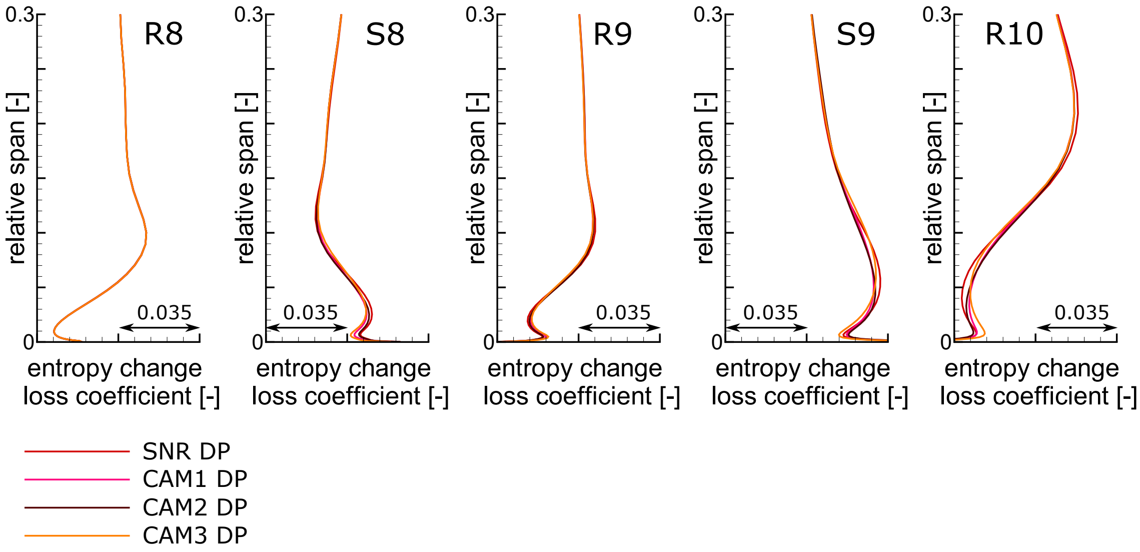

Figure 4.46: HSC, endwall profile study radial distributions of the entropy change loss coefficient at the DP operating conditions for the SNR, CAM1, CAM2 and CAM3 configurations

dence is impacted. At 5% of the span, all the newly designed configurations reduce the effective incidence, as indicated by the smaller LE suction side spikes. Among them, CAM1 is the configuration with lower effective incidence both for S8 and S9. At 20% of the span, the differences between the newly designed configurations and the original one are less marked and at 50% of the span hardly any change can be spotted in the distribution of the isentropic Mach number. This trend was expected because only the lower 30% of the stator vanes were modified and it is in agreement with the trend observed in Figure 4.46 for the radial distribution of the entropy change loss coefficient at the DP. The isentropic Mach number distributions of the rotors are presented in appendix C.1 for the sake of completeness.

4.5.4.6 Near-stall analysis

The near-stall analysis is conducted for the best endwall section configuration, CAM1, with the aim to better understand how the configuration of vane and endwall increases the efficiency at near-stall operating conditions, and how stall is delayed, thus stall margin is extended. The stall analysis for the original configuration, SNR, is conducted in section 4.5.3.

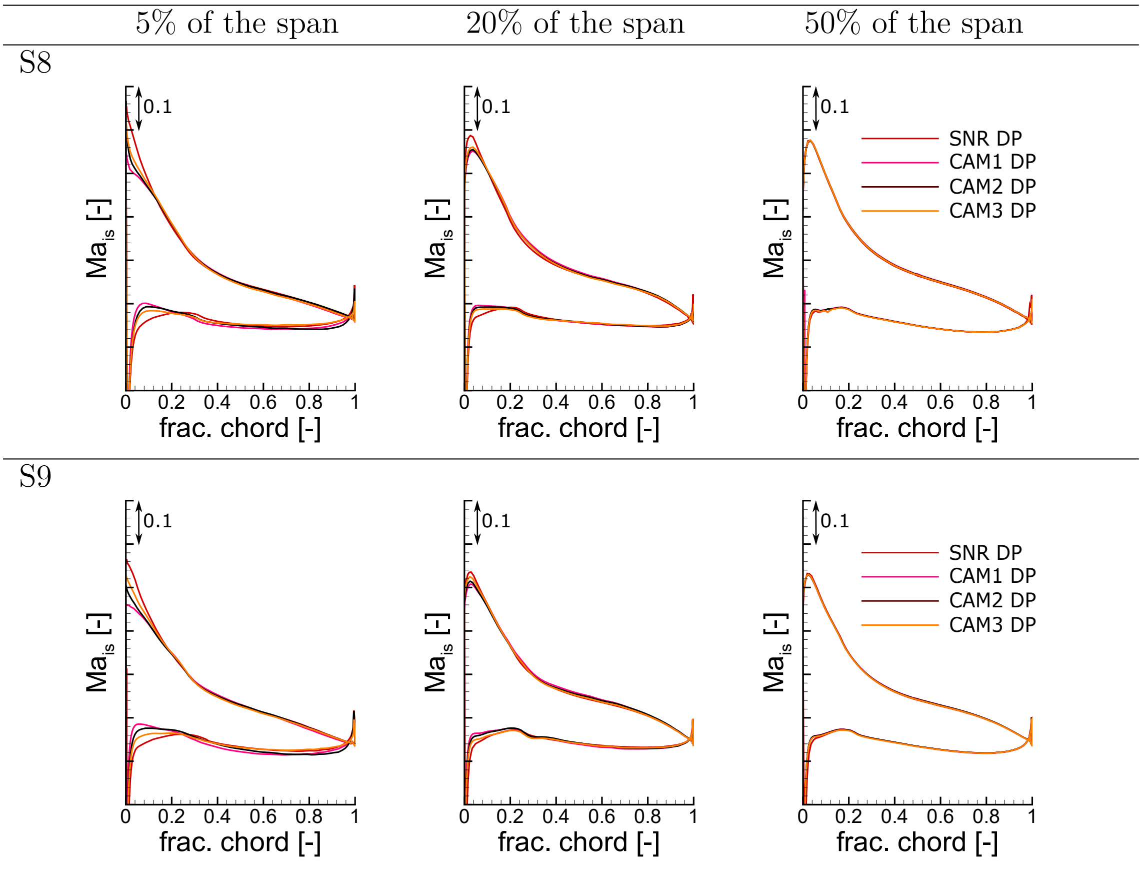

Figure 4.47: HSC, endwall profile study, profile isentropic Mach number distributions for S8 and S9 at 5%, 20% and 50% of the span at the DP operating conditions

Figure 4.48 shows, for CAM1, the radial distributions of the entropy change loss coefficient at the DP, TS and NS operating conditions, highlighted in Figure 4.44. Additionally, the SNR at the NS operating condition is shown in red. At the NS, despite the loss trend of CAM1 is very similar to the one of SNR, both S8 and S9 have lower losses at the hub. This applies especially for S9 in the region between 0% and 18% of the span. R10 inlet flow conditions are therefore improved and this delays the stall.

Figure 4.49 and Figure 4.50 show in red, for S8 and S9 respectively, the regions of reverse flow and in green, the entropy contours downstream of the stator trailing edge at the operating conditions DP, TS and NS of SNR and CAM1. For S8, hardly any change can be observed at the DP and TS between the SNR and CAM1. Instead, at NS, SNR has a region of reverse flow at the hub, which does not appear for CAM1. Thus the newly designed stator aerofoil eliminates the region of reverse flow for S8.

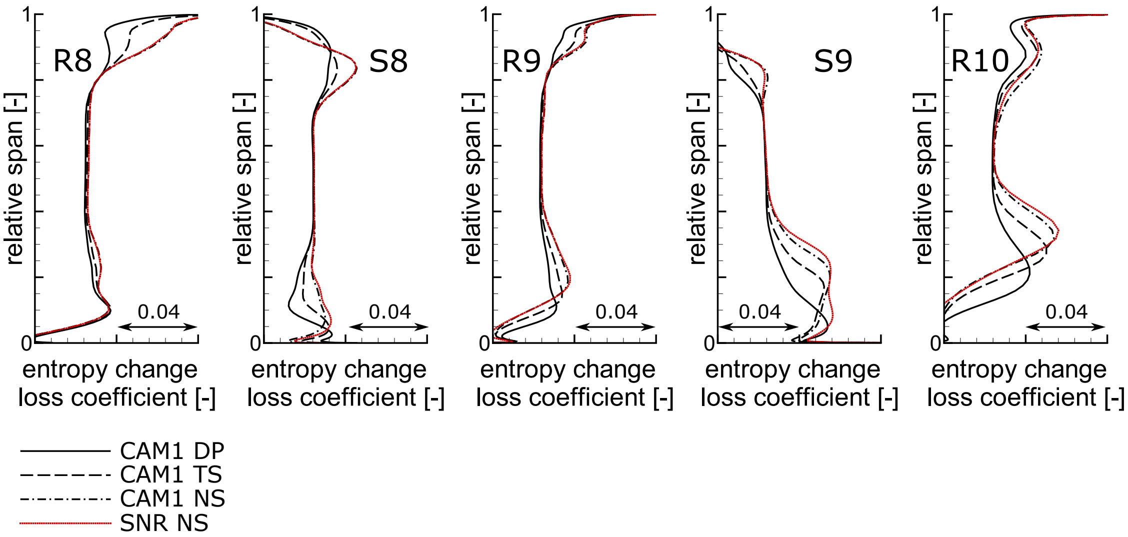

Figure 4.48: HSC, endwall profile study, radial distributions of the entropy change loss coefficient at the operating conditions DP, TS and NS for the CAM1 configuration and at the NS operating condition for the SNR configuration

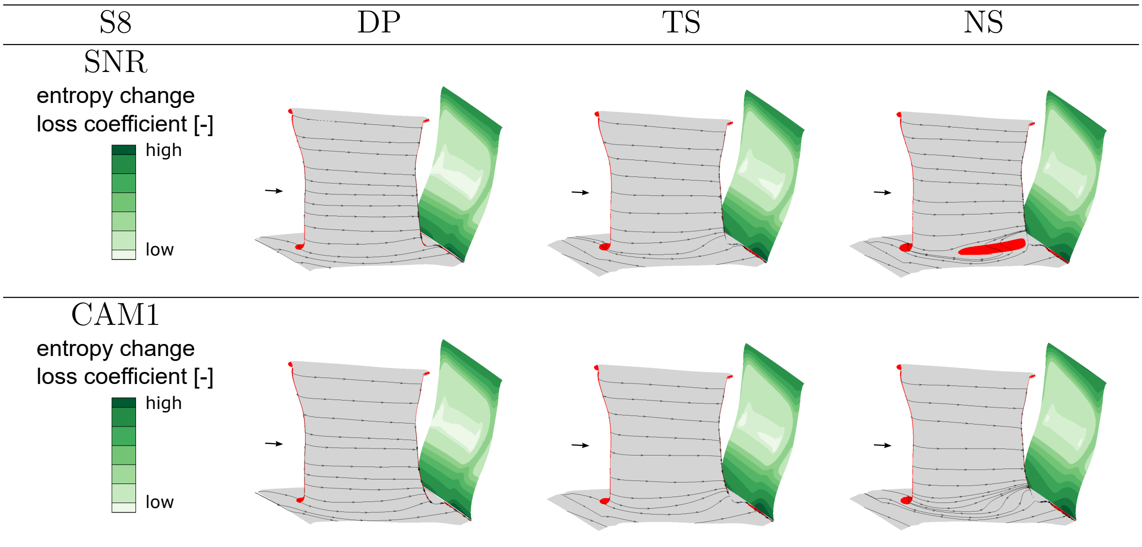

Figure 4.49: HSC, endwall profile study, near-stall for the SNE and CAM1 configurations. The regions of negative axial velocity on S8 are depicted in red and the entropy contours downstream of the stator TE are depicted in green

Considering S9, we observe some differences not only at the NS but also at the TS. As for S8, at the DP the two configurations behave very similarly. This is in agreements with the overall and stage performance. At TS, the two configurations show a small region of reverse flow close to the TE in the hub region for S9, which is very small

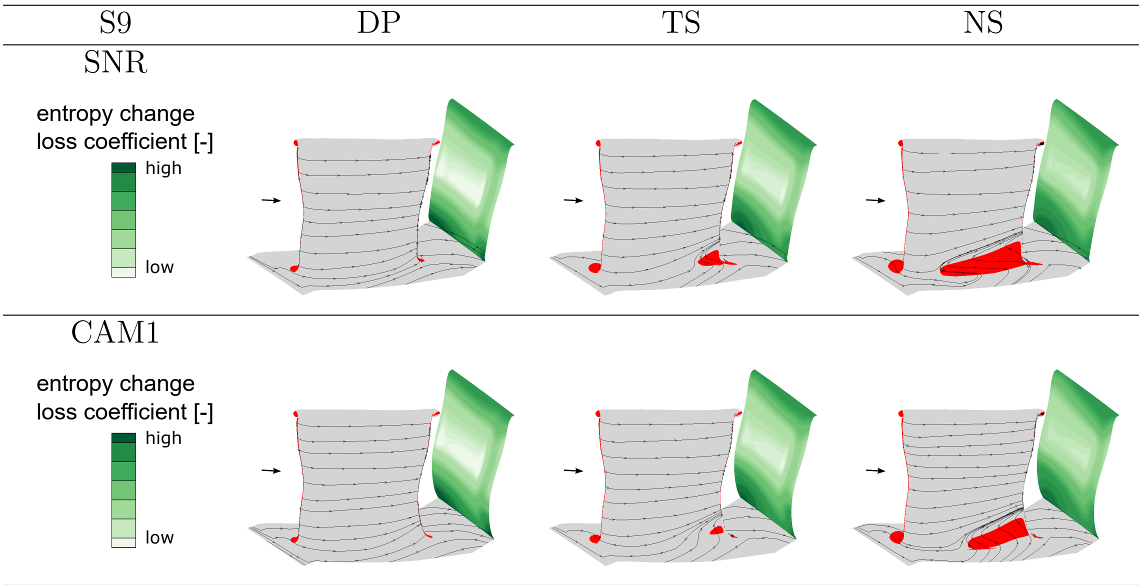

Figure 4.50: HSC, endwall profile study, near-stall for the SNE and CAM1 configurations. The regions of negative axial velocity on S9 are depicted in red and the entropy contours downstream of the stator TE are depicted in green at the operating conditions DP, TS and NS

for CAM1, whereas visibly larger for SNR. At NS, the difference between SNR and CAM1 are more evident. For S9, CAM1 is not removing the endwall reverse flow region but strongly reducing it.

4.5.5 Key Outcomes

In this section, a parametric study was performed on a reduced model of the entire 5.5-stage model to quantify the impact of selected significant design parameters. The parameters considered in the sensitivity study were the clearance levels, the degree of reaction, and the endwall stator vane geometry. The impact of the clearances was considered both for shrouded and cantilevered configurations, whereas the impact of the degree of reaction and the endwall camber line style was considered only for the shrouded configuration with nominal clearances. For these two studies, the design flow coefficient and the work coefficient were maintained constant.

The reduced model consists of stages 8, stage 9 and R10. The inlet of the reduced model coincides with the mixing plane between S7 and R8 for the entire model, whereas the outlet of the reduced model coincides with the mixing plane between R10 and S10 for the entire model. The inlet boundary conditions differ between the shrouded and the cantilevered configurations, and are derived by simulating the entire model using their respective stator hub sealing approach. Using a reduced model allowed us to perform the sensitivity study more quickly by speeding up the design process, especially when the pressure ratio and incidence need to be matched.

In the clearance study, the stator aerofoil geometry was maintained unchanged between cantilevered and shrouded vanes, except for the thickness distribution along the span. The clearances considered varied from 0.7 to 2.0 of the nominal clearances. As expected, we observed a decrease of efficiency and stall margin when the clearances were increased for both designs. Furthermore, the study of the efficiency sensitivity to the clearance size has proven, that the shrouded configuration is more sensitive to an increase of clearances. R10 has been found to be the row triggering stall of the machine, both for the shrouded and cantilevered configuration with different levels of clearance.

The impact of the degree of reaction was investigated by considering 4 different degrees of reaction for the shrouded configuration, while keeping the design flow coefficient and the work coefficient constant. Starting from the shrouded configuration with nominal clearances, two designs with a higher degree of reaction and one with a lower degree of reaction were considered. A limited increase of the degree of reaction results in very similar performance as the original model's at the design point, but with an improved efficiency at the near-stall operating conditions and with a greater stall margin. This is a consequence of the reduced hub losses for S9, which delay the stall of the machine. However, a too large increase of the degree of reaction results in a decreased stall margin and lower efficiency across most of the operational range, as the rotor tip leakage vortex grows drastically. A lower efficiency was also predicted for the configuration with a reduced degree of reaction. In this case, the losses at the rotor tips are reduced, but those in the stator hub regions increase to a larger extend, thus driving the observed performance deterioration.

To evaluate the impact of the camber line distribution of the stator vanes in the hub region near the inner shroud, four different camber line styles were considered. For each of them, the new camber line distribution was imposed in the aerofoil section at the hub and blended into the section at 30% of the span. As for the degree of reaction study, the original configuration was the shrouded configuration with nominal clearances and, the design flow coefficient and the work coefficient were kept constant. All the newly designed camber line distributions give very similar performance as the original configuration at the design point and all of them are driven to stall by the same row, R10. All of them result in a larger stall margin gained by the reduced losses occurring in the S9 hub region, which improve the inflow condition of R10. The configuration, which results in a greater stall margin, is the one with circular-arc camber line distribution.

For all the designs considered in the parametric study, R10 is the row taking the machine to stall. However, the stall margin of the machine is strongly affected by S9 loss distribution, which is strongly affected by the parameters considered in the sensitivity study. S9, being the second stator downstream, is not only directly impacted by the stator vane design changes, but it is also indirectly affected by S8 changes. The sensitivity study has revealed, that without changing the clearances and keeping the flow designs and work design constant only minor performance improvements could be achieved at the design point while considerable improvements were achieved at the near-stall operating points.

The results of this sensitivity study were eventually used in the following section 4.6 to design two improved shrouded configurations.

4.6 Improved configurations

In the previous section, a parametric study was conducted on the reduced model to understand the impact of each of the following parameters: the clearance level of the stators, the degree of reaction, and the stator near-endwall profile style at the hub. In this part of the work, the best designs resulting from the parametric analysis are combined with the aim to generate two improved configurations.

The two improved configurations differs because of their degree of reaction, but have the same stator endwall profile style. Indeed, the analysis presented in section 4.5.3 indicates the configuration DOR2 as the best one among those considered for the degree of reaction study. DOR2 has an increased stall margin and efficiency at the near-stall operating conditions when compared with the original configuration SNR, but has limited effect at the design point. Because the performance of the original configuration SNR are also very promising, both DOR2 and the baseline degrees of reaction are considered in this section. In terms of camber line distribution, CAM1, which corresponds to the circular-arc stator near-endwall profile style, is the best configuration, both in terms of efficiency and stall margin among the configurations investigated in the near-endwall profile study.

The performance of the two improved configurations are compared with that of the two reference configurations: the reference cantilevered configuration with nominal clearances and the reference shrouded configuration with reduced clearances. Indeed, as one of the main goals of the present work was to investigate the aerodynamic performance of the shrouded configuration against that of the cantilevered one, in this part of the work it was not only studied how the two improved designs enhance the flow field in comparison with the reference shrouded configuration, but also the original cantilevered design was considered. As shrouded stators generally allows smaller clearances in comparison to cantilevered stators when accounting for mechanical requirements, to fairly compare the cantilevered and the shrouded configurations the reference clearances introduced in section 4.3 are used in this section for the two stator hub configurations. Nominal clearances were set for the cantilevered configuration and reduced clearances were used for the shrouded one.

The two improved designs are investigated by considering the overall performance, the stage performance, and radial distributions as well as flow field details at the design point and near-stall. Also, a sensibility study to investigate the impact of the clearance levels on the efficiency at the design point is presented.

4.6.1 Methodology

As presented in Table 4.8, the following four configurations are considered: the reference cantilevered configuration, CNR, the reference shrouded configuration, SRR, the shrouded configuration with the circular-arc profile camber line distribution at stator hubs, OPT1, and the shrouded configuration with the same degree of reaction as DOR2 and the circular-arc profile camber line distribution at stator hubs, OPT2.

Table 4.8: HSC, improved configurations, configurations considered

name	degree of reaction	camber line	clearances
CNR	baseline	baseline	nominal
SRR	baseline	baseline	reduced
OPT1	baseline	CAM1	reduced
OPT2	DOR2	CAM1	reduced

The parameters which define the aerofoil geometries, with the exception of the thickness-to-chord ratio, were kept unchanged when the reference shrouded configuration was derived from the baseline cantilevered configuration. Consequently, both CNR and SRR have the baseline degree of reaction and the baseline stator camber line style. All the shrouded configurations are equipped with reduced clearances, equal to approximately 1.1% of the S7 span, whereas the cantilevered configuration is equipped with nominal clearances, equal to approximately 1.5% of the S7 span. The methodology used to change the degree of reaction and the camber line is presented in the section 4.5.3.1 and section 4.5.4.1, respectively.

4.6.2 Overall performance

In Figure 4.51, the overall performance of the four configurations presented in Table 4.8 are shown. The overall performance considers only stage 8 and stage 9, thus excluding R10.

When comparing the CNR and SRR configurations, we observe that the shrouded configuration has a higher efficiency across the entire operational range. In terms of total pressure ratio, the two configurations show a very similar trend, even if the shrouded configuration has a slightly higher slope resulting in a higher pressure

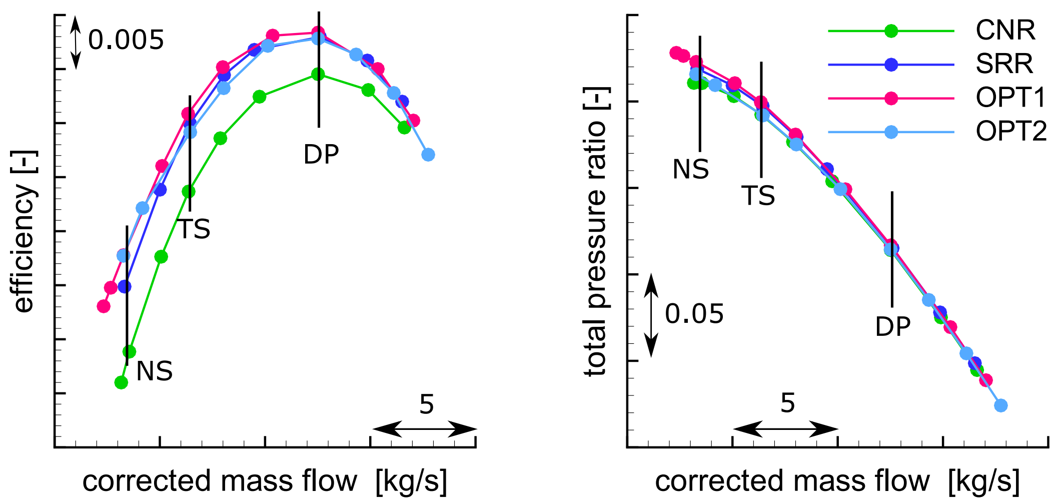

Figure 4.51: HSC, improved configurations, overall performance

ratio for lower mass flows. These results are in agreement with those of the entire model depicted in Figure 4.10 for CNE and SRE. For the reduced model, we do not observe the pressure ratio shift observed for the entire model as it was mainly caused by stage 7, which is not included in the reduced model.

The improved shrouded configuration OPT1 performs similarly to SRR for high mass flows and better, both in terms of efficiency and total pressure ratio, starting with the DP operating condition and moving towards stall. The stall margin of the OPT1 is visibly improved with respect to the other configurations considered.

Considering the improved shrouded configuration OPT2 at the design point, OPT2 and SRR have the same efficiency, whereas close to stall, OPT2 has higher efficiency, which correspond to the one of OPT1. In terms of the total pressure ratio characteristic, OPT2 rolls over earlier when compared with SRR and OPT1, and follows a similar trend as CNR.

The results show, that a combination of clearances, degree of reaction, and stator near-endwall profile style leads to non-trivial results. OPT1 shows both an improvement of the stall margin and of the efficiency across most of the operational range. Instead, in the stator near-endwall geometry study, presented in section 4.5.4, the configuration CAM1, corresponding to OPT1 with nominal clearance, only results in a larger stall margin but, except for the near-stall region, there were no visible improvements in terms of efficiency when compared with the original configuration SNR. OPT2, which combines the best degree of reaction with the best camber line distribution, results in stall margin and efficiency similar to those of the SRR configuration. Only close to the stall point, we observe a higher efficiency. The results indicate, that the change of degree of reaction reduces the improvement introduced by the change of the camber line distribution. However, the study of the best camber line distribution was limited to the baseline degree of reaction. Therefore, in order to identify the best stator near-endwall profile camber line distribution for a new degree of reaction, a dedicated parametric study should be performed.

In the next sections, the stage performance, and details of the radial distributions and the flow field at the design point and the near-stall conditions are considered. In particular, the aim of the analysis is to understand, why, when compared with the reference shrouded configuration SRR, OPT1 is slightly more efficient and OPT2 has the same stall margin.

4.6.3 Stage performance

Figure 4.52 depicts the stage performance for the four configurations considered. For stage 8, the cantilevered configuration is very inefficient compared with the three shrouded configurations. This trend is not observed for stage 9, where for high mass flows the cantilevered performs even better than the shrouded configurations. The trend of the total pressure ratio is very similar across the four configurations for both stages. These results are in agreement with the stage performance of the entire model shown in Figure 4.11.

Considering the shrouded configurations, the efficiency of the three configurations is very similar for stage 8, whereas some differences can be observed for stage 9. There OPT1 is the configuration with higher efficiency across most of the operational range, whereas the efficiency of OPT2 varies across the operational range, being lower than SRR for high mass flows and similar to OPT1 close to stall.

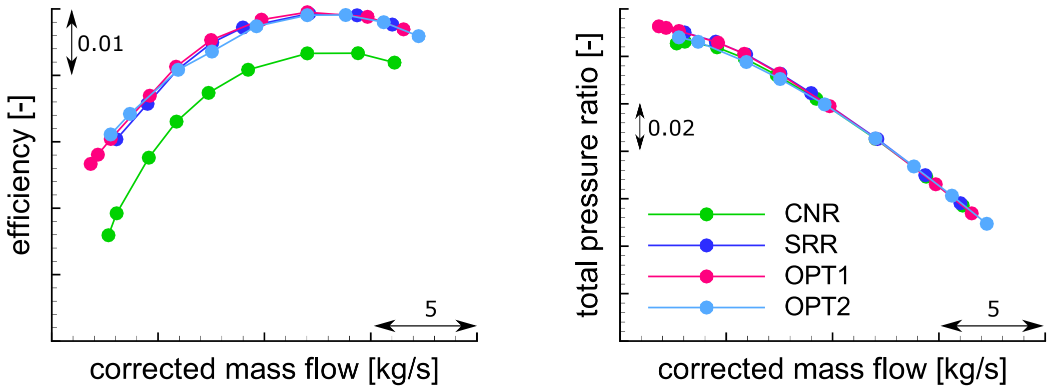

a) Stage 8

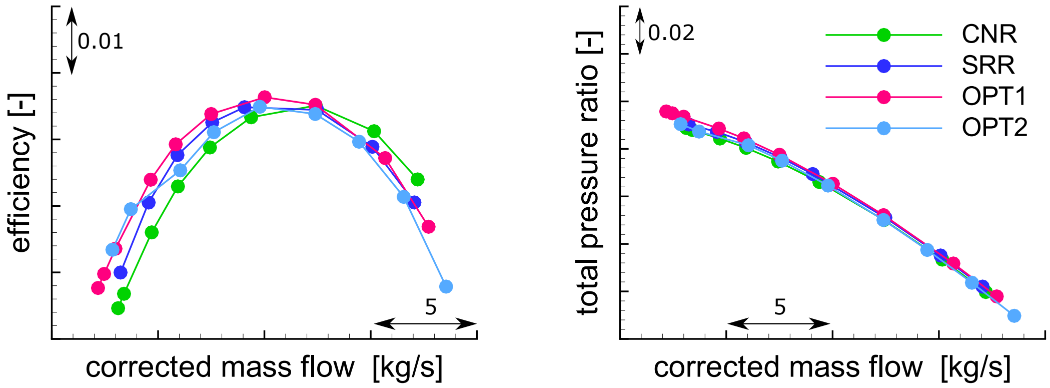

b) Stage 9

Figure 4.52: HSC, improved configurations, stage performance

4.6.4 Design point analysis

The radial distributions of the entropy change loss coefficient are presented in Figure 4.53 for the configurations CNR, SRR, OPT1 and OPT2.

The comparison of the cantilevered configuration with nominal clearance and the shrouded configuration with reduced clearance is presented, for the entire model, in the section 4.4.3. Although we observe some differences between the entire and the the reduced model, the same observation made for the entire model apply also to the reduced one.

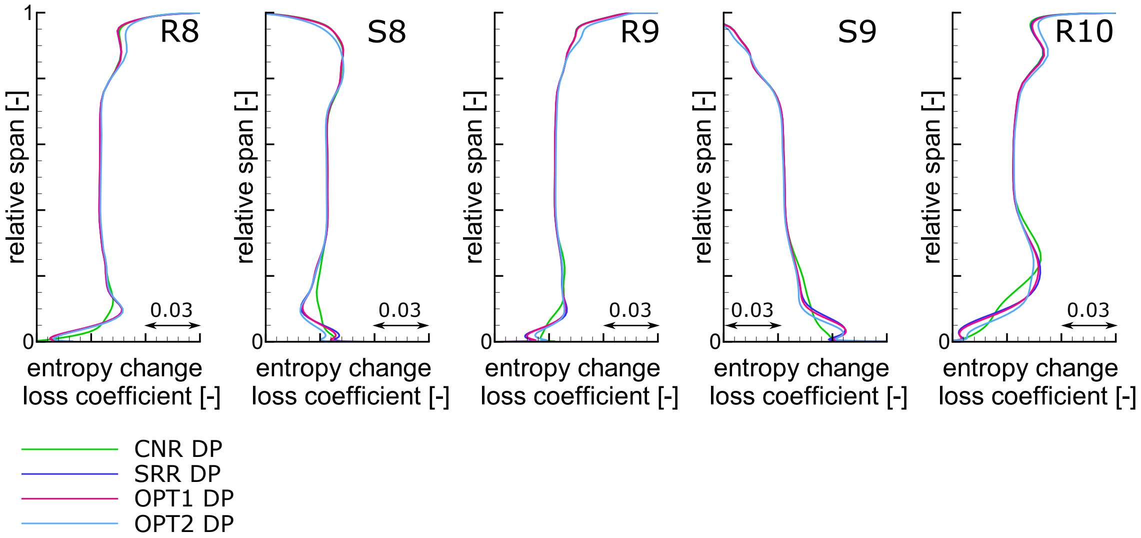

Figure 4.53: HSC, improved configurations, radial distributions of the entropy change loss coefficient at the DP operating conditions for the CNR, SRR, OPT1 and OPT2 configurations

SRR and OPT1 show only small differences, mostly limited to the hub region, both for the rotors and the stators. OPT2 instead presents higher losses at the tip for the rotors and lower losses at the hub for the stators. This trend was expected because, as observed in the section 4.5.3, the higher degree of reaction of OPT2 reduces the amount of leakage that re-circulates through the stator shroud cavity, thus reduces the associated losses across the stators, however it has the disadvantage of increasing the rotors tip leakage flow.

Despite SRR and OPT1 have a very similar losses trend, some differences can be observed. In particular, the lower losses of OPT1 for S9, between 5% and 12% of the span height, results in slightly higher efficiency of stage 9 for OPT1, which was observed in Figure 4.52. For both stage 8 and stage 9, OPT2 performs as efficiently as SRR because the positive impact of the higher degree of reaction on the stator hub losses is compensated by the negative impact of the higher rotor losses.

Considering the profile isentropic Mach number distributions of the stators in Figure 4.54, we observe consistent differences between the four configurations at 5% of the span, whereas the differences are very limited at 50% and 90% of the span, with the exception of the configuration OPT2. Indeed, OPT2 having a different degree of

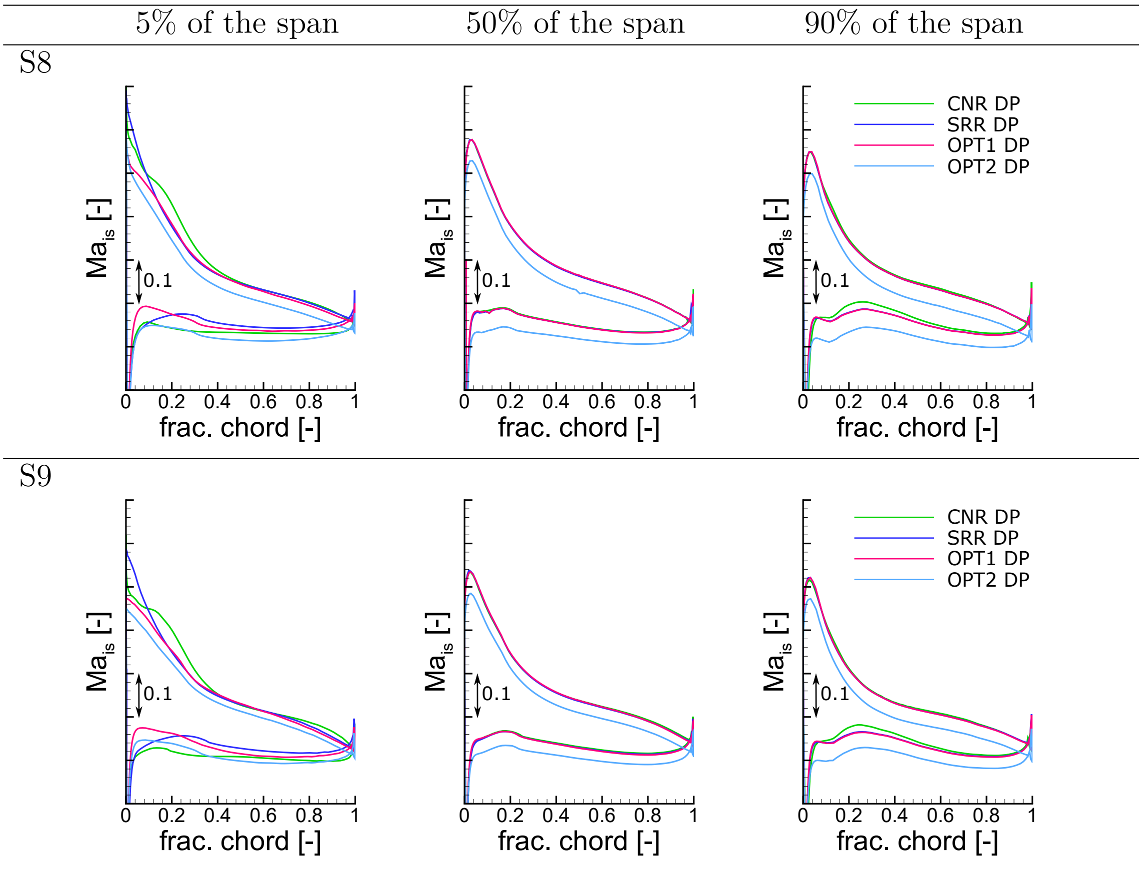

Figure 4.54: HSC, improved configurations, profile isentropic Mach number distributions for S8 and S9 at 5%, 50% and 90% of the span

reaction in comparison with the other three configurations, the flow field is affected along the entire span. At 5% of the span, SRR is the configuration with higher effective incidence for both S8 and S9. The Mach number distributions differ between the two reference configurations, CNR and SRR, because of the different stator hub configuration, thickness distribution along the chord and R8 inlet boundary conditions. The two improved configurations have the same trend for S8 and S9, with OPT2 translated towards lower values of isentropic Mach number. Only at the LE of S8 a different slope between the two configurations is to be observed. As expected, the higher degree of reaction of OPT2 results in a shift of the Mach number distribution of the stator towards lower values for all the spanwise locations considered. Instead, the change of the near-endwall profile style impacts only the lower 30% of the stator vanes. This is in agreement with the observation made in the section 4.5.4. Moreover, the rotors' profile isentropic Mach number are presented in appendix C.1 for reasons of completeness.

Configuration	R8	R9	R10
CNR	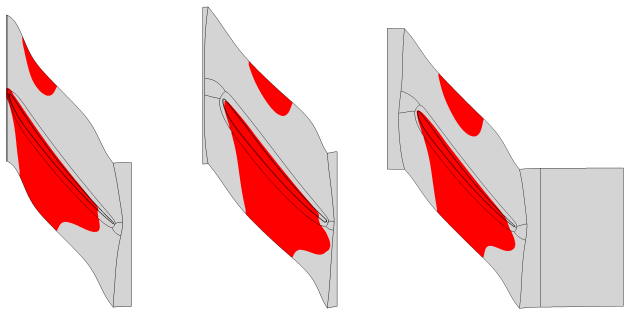		
SRR	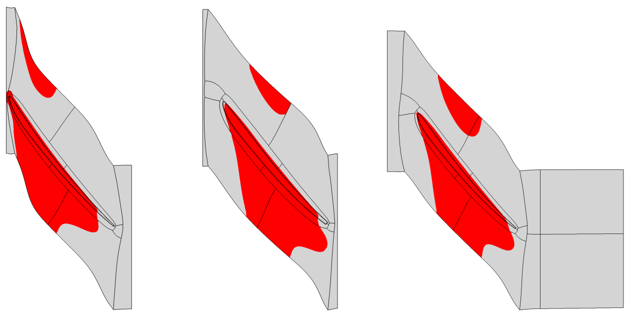		
OPT1	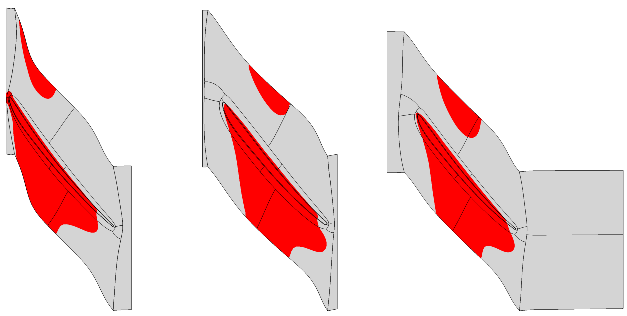		
OPT2	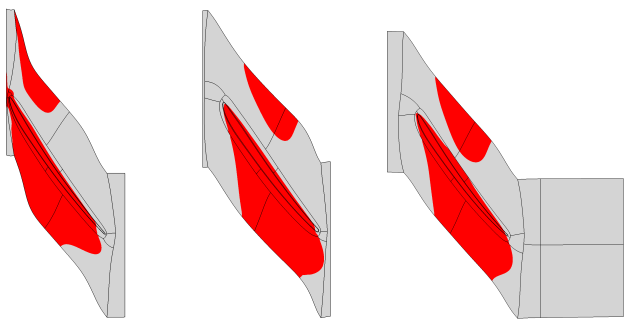		

Figure 4.55: HSC, improved configurations, regions of negative axial velocity at the mid-clearance height of the rotors for CNR, SRR, OPT1 and OPT2 at the DP operating conditions

The regions of reverse flow at the mid-clearance height of the rotors for the CNR, SRR, OPT1 and OPT2 configurations at the design point are presented in Figure 4.55. Hardly any difference can be observed between CNR, SRR and OPT1, being the changes mostly limited to the lower 30% of the vane height. More consistent differences emerges instead between OPT2 in comparison with the other three configurations. For all the three rotors, the regions of reverse flow are larger for OPT2, as consequence of the higher degree of reaction. This is in agreement the regions of reverse flow at the mid-clearance height of the rotors for the SNR and DOR2 configurations at the DP operating conditions depicted in Figure 4.36.

Efficiency vs. Clearance at the Design Point

At the design point, the four configurations presented in Table 4.8 are investigated for the different level of clearances presented in Table 4.4. The configurations C, S, O1 and O2 correspond respectively to the CNR, SRR, OPT1 and OPT2 when the clearances are varied. Thus, the OPT1 configuration is the O1 configuration with reduced clearances. As shown in Figure 4.56, when the clearances are increased, O1 and S show the same trend, with O1 having a slightly higher efficiency. This

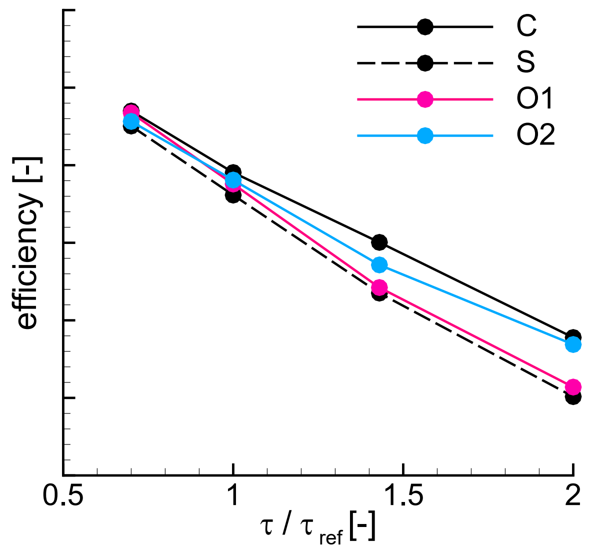

Figure 4.56: HSC, improved configurations, isentropic efficiency vs. clearance levels for the cantilevered, the shrouded and the two improved configurations O1 and O2

indicated, that O1 does not introduce a seal clearance height desensitization in the compressor block.

O2 has instead, for the larger clearances level considered, the same efficiency as C. It is markedly higher in comparison with the original shrouded design. This result is very important as it indicates that the sensitivity of the shrouded configuration to clearance changes can be improved by altering the degree of reaction and the stator near-endwall profile camber line style and, it can become similar to the one of the cantilevered.

4.6.5 Near-stall analysis

The near-stall analysis is conducted for the two improved configurations, OPT1 and OPT2, with the aim to gain more insight into the stall mechanism related to the two configurations. For CNR and SRR the near-stall analysis is reported in the section 4.5.2.3 and the section 4.5.2.4, respectively.

Figure 4.57 shows for OPT1 the radial distributions of the entropy change loss coefficient for the DP, TS and NS, highlighted in Figure 4.51. Additionally, the SRR configuration at the NS is shown in red. When the mass flow is reduced, the losses increase both on the rotors and the stators. In particular, we observe larger losses occurring on the individual rows tip, which extend across in the upper 60% of the span for R10. At the NS operating conditions, OPT1 and SRR show a similar trend. They differ at the hub for both S8 and S9, with OPT1 having lower losses. Moreover, for R10, OPT1 presents higher losses in the lower 25% of the span as well as toward the casing, and lower losses between 25% and 55% of the span.

A similar trend can be observed in Figure 4.48, where the OPT1 and SRR configurations are compared for the nominal clearances. Indeed OPT1 has the same aerofoil geometry as CAM1 but a different level of clearance. There, R10 presents similar loss distributions for CAM1 and SNR in the lower 30% of the span. The same conclusions drawn for the CAM1 analysis applies for OPT1, namely the circular-arc camber line distribution imposed in the hub section and blended into the section

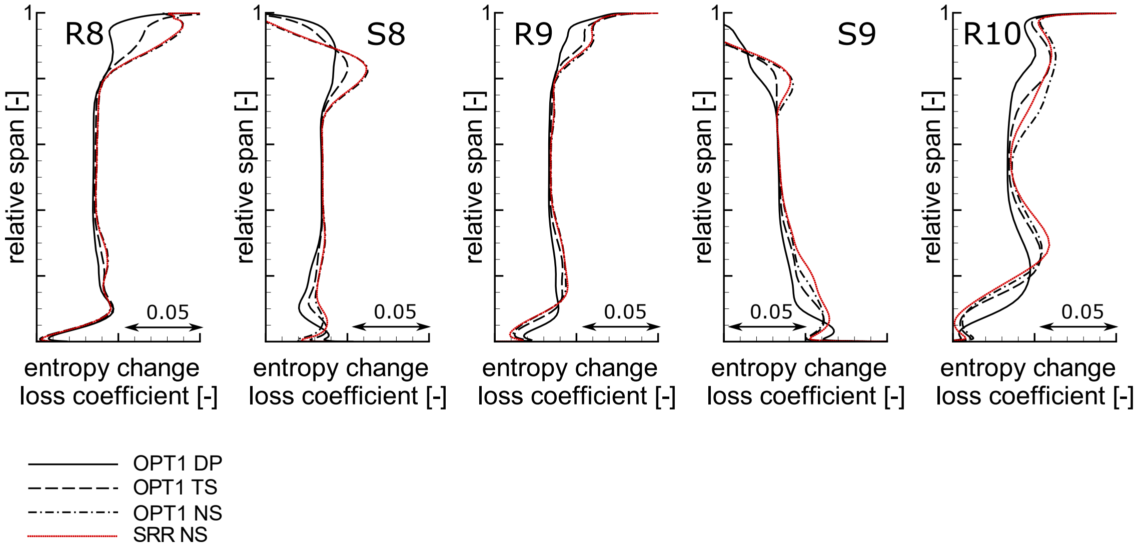

Figure 4.57: HSC, improved configurations, radial distributions of the entropy change loss coefficient at the operating conditions DP, TS and NS for the OPT1 configuration and at the NS operating condition for the SRR configuration

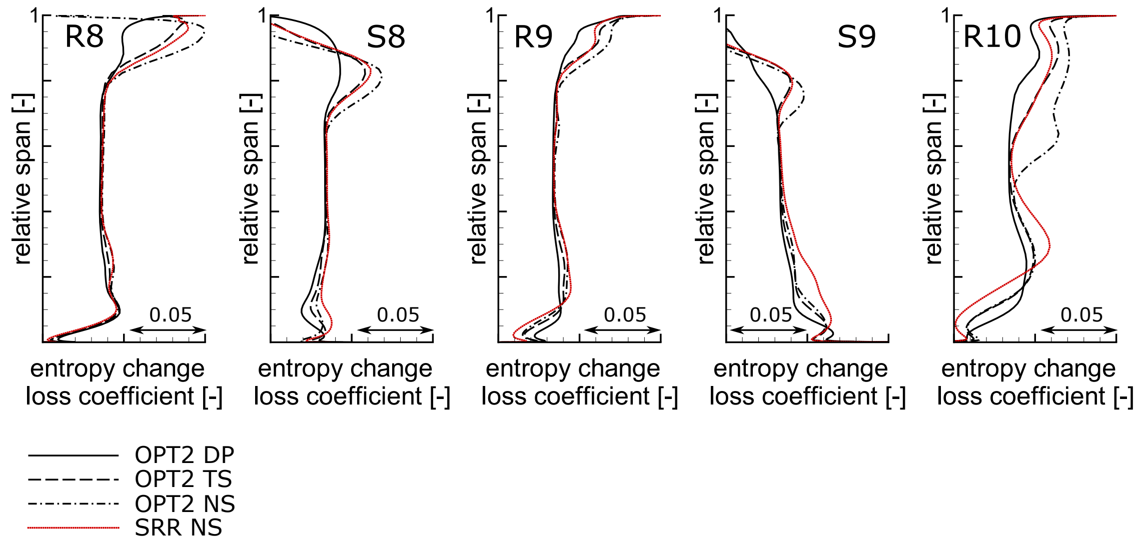

Figure 4.58: HSC, improved configurations, radial distributions of the entropy change loss coefficient at the operating conditions DP, TS and NS for the OPT2 configuration and at the NS operating condition for the SRR configuration

at 30% of the aerofoil height of the original stator geometry, reduces the amount of losses for both stators in the hub region, and results in an improved inlet flow conditions for R10, which delays the onset of stall of the machine.

Similarly to Figure 4.57 showing OPT1, Figure 4.58 shows the radial distribution of the entropy change loss coefficient at the operating points DP, TS and NS for OPT2, and at NS for SRR. OPT2 combines the best degree of reaction, DOR2, with the best camber line distribution CAM1 resulting from the parametric study. As observed for Figure 4.57, decreasing the mass flow results in higher losses especially at the tip of the rotor blades. For OPT2 the loss increase on R10 at the NS is significant and it extends from 50% of the span up to the casing. This increase of losses on R10 is causing the configuration OPT2 to stall earlier than OPT1, showing, that the increased degree of reaction has a negative impact on the stall margin of the machine. This indicates, that the study of the best camber line distribution should be customized for the specific degree of reaction considered. Indeed, it is important to understand, that the original configuration for the stator near-endwall profile study is the SNR configuration, designed with the baseline degree of reaction and the baseline camber line distribution at the hub. Therefore, the stator near-endwall geometry study was performed for the baseline degree of reaction and not for the best one, DOR2.

In comparison with SRR, OPT2 has, at the NS operating condition, higher losses in the tip regions of all the rows and lower losses at the hub for the stators. This is a direct consequence of the higher degree of reaction of OPT2.

The regions of reverse flow on S8, depicted in Figure 4.59, do not show relevant differences between the three shrouded configurations. Indeed, even at the NS operating conditions, there are no large regions of reverse flow. For S9, instead, Figure 4.60 reports a consistent difference at the NS operating points. There, the endwall region of reverse flow observed for SRR is completely removed for the two improved configurations. The CNR configuration, being equipped with a cantilevered stator hub design, follows a different trend in comparison with the shrouded configurations and the regions of reverse flow result from the hub leakage vortices originated in the radial clearances present between stator tip and the inner gaspath contour.

The regions of reverse flow at the mid-clearance height of the rotors at the NS operating conditions, depicted in Figure 4.61, are only considered for the OPT1 and OPT2 configurations. Similarly as observed for Figure 4.41 for the degree of reaction

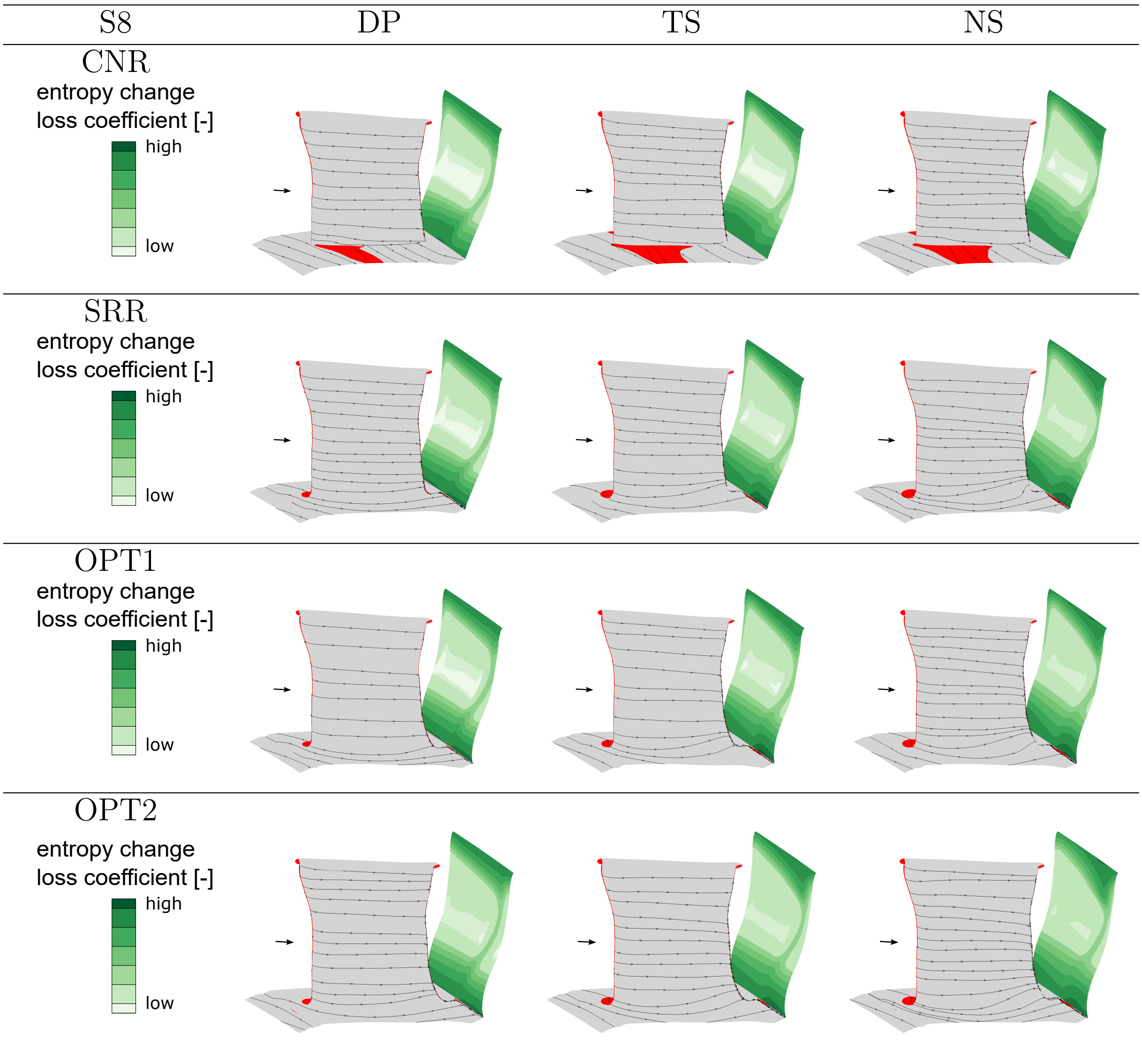

Figure 4.59: HSC, improved configurations, near-stall for the CNE, SRR, OPT1 and OPT2 configurations. The regions of negative axial velocity on S8 are depicted in red and the entropy contours downstream of the stator TE are depicted in green

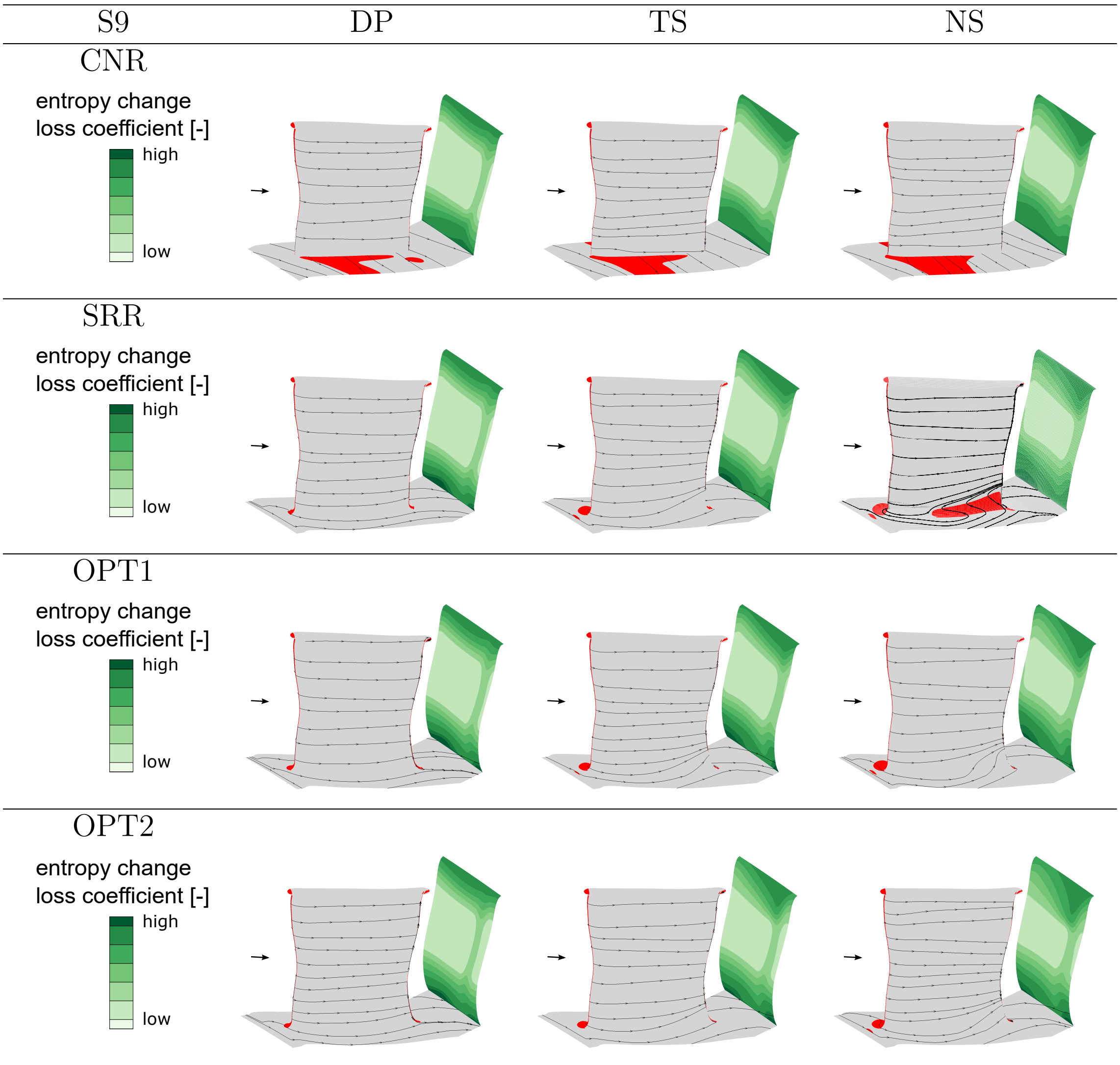

Figure 4.60: HSC, improved configurations, near-stall for the CNE, SRR, OPT1 and OPT2 configurations. The regions of negative axial velocity on S9 are depicted in red and the entropy contours downstream of the stator TE are depicted in green

study, OPT2, due to the larger degree of reaction, results in larger regions of reverse flow for all rotors, which are more expanded both in the axial and the circumferential direction. R9 and R10 are affected to a larger extend in comparison with R8.

Configuration	R8	R9	R10
OPT1	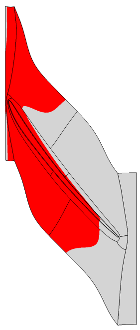	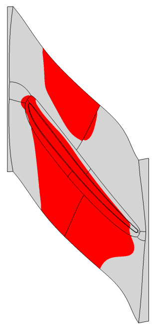	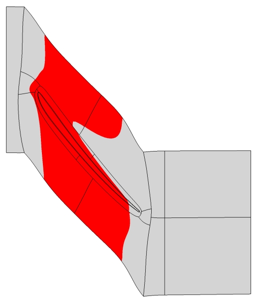
OPT2	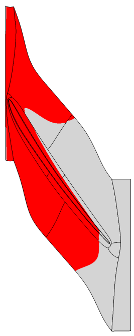	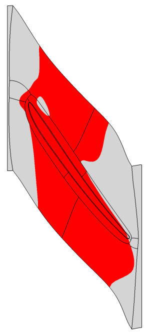	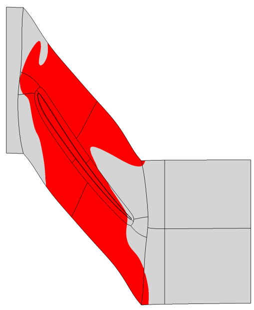

Figure 4.61: HSC, improved configurations, the regions of negative axial velocity at the mid-clearance height of the rotors for the OPT1 and OPT2 configurations at the NS operating conditions are depicted in red

4.6.6 Key Outcomes

The results of the parametric study were used to derive two improved configurations featuring shrouded stators, which combine the best results of the degree of reaction and the camber line distribution parametric study. The two improved configurations, OPT1 and OPT2, feature stators with circular-arc camber distribution profiles in the near-endwall hub region and differ because of the degree of reaction. OPT1 is the improved configuration with the baseline degree of reaction, and OPT2 has a moderate increase of degree of reaction.

In this part of the work, it was investigated not only how the two improved designs enhance the flow field compared to the reference shrouded configuration, but the work also considered the original cantilevered design, as one of the main goals of the project was investigating the aerodynamic performance of the shrouded configuration beside that of the cantilevered one. For the three shrouded configurations the reduced clearances were used, whereas for the cantilevered configuration the nominal clearances were employed. Indeed, cantilevered configurations generally require larger clearances than the shrouded ones, thus a fair comparison requires different level of clearances.

For the entire operational range, the cantilevered design with nominal clearances has lower efficiency compared to the three shrouded designs with reduced clearances. This results mainly from the lower efficiency at stage 8 of the cantilevered configuration. The same trend was observed for the 5.5-stage model in section 4.4. The radial distributions of the entropy change loss coefficient showed, that the major losses of the cantilevered design happen mostly at S8, in the region between 5% and 25% of the span.

OPT1 showed both an improvement of the stall margin and the efficiency across most of the operational range when compared with the two reference configurations and OPT2. OPT1, having the baseline degree of reaction and the near-endwall circular-arc camber line distribution, corresponds to the configuration CAM1 studied in section 4.5.4, in which the reduced clearances are employed instead of the nominal ones. The configuration CAM1, when compared against SNR, resulted in a larger stall margin but the efficiency was only improved at the near-stall operating conditions and remained almost unchanged at the design point. Indeed, in comparison with the reference shrouded configuration SRR, OPT1 showed slightly higher efficiency at the design point. The two configurations mostly differ close to the stall boundary, where OPT1 performs better because of the improved flow conditions in the hub region for both S8 and S9, which delay the stall of R10.

OPT2, which combines the best degree of reaction and the best stator near-endwall camber line distribution, resulted in stall margin and efficiency similar to the reference shrouded configuration. Only close to the stall point a higher efficiency was observed, which is similar to the efficiency of OPT1. This indicates, that the change of the degree of reaction reduces the improvement introduced by the change of the camber line distribution and highlights, that a detailed study of the best camber line distribution should be performed for every degree of reaction considered, giving scope for follow-on research work. At the design point, differences between the reference shrouded configuration and OPT2 along the entire span height occurred. Indeed, OPT2 has a higher degree of reaction compared to the reference shrouded configuration, which resulted in lower losses at the hub for the stators and larger losses at the tip of the rotors. These increased rotor losses, in particular for R10, represented the main stall-trigger and therefore was the stability-limiting row in the CFD simulations carried out.

The study of the efficiency sensitivity to the clearance level revealed that OPT2 provides reduced sensitivity to the clearance size, having, for the largest clearances considered, the same efficiency at the design point as for the cantilevered design. Instead, OPT1 does not introduce any seal clearance height desensitisation in the compressor block. It follows, that the sensitivity towards clearance size can be strongly affected by the degree of reaction, and that the shrouded and cantilevered designs can have similar sensitivity even for large clearances.

The results showed that a combination of clearances, degree of reaction, and hub camber line distribution leads to non-trivial results. Therefore, for each degree of reaction considered, a dedicated parametric study should be performed to identify the best camber line distribution at the hub and, for each newly designed configuration, the impact of the clearances should be investigated.

4.7 Conclusion and design recommendations

The last 5.5 stages of a high-speed subsonic axial compressor were numerically investigated for two different stator hub configurations: cantilevered and shrouded. The machine was originally designed to be equipped exclusively with cantilevered stators, and the shrouded configuration was derived from this cantilevered baseline by changing the stator hub configuration of the first four stators. A typical labyrinth geometry was selected to seal the cavity, and the stator aerofoil design was left unchanged except for the spanwise thickness distribution, which was adapted considering the structural requirements of shrouded stator vanes. Two shrouded configurations were considered: one with the same clearances as the cantilevered configuration and one with reduced clearances. This choice is linked to the fact, that shrouded vanes generally require smaller clearances in respect to the cantilevered ones; therefore, different levels of clearance need to be used to fairly compare the two stator configurations.

Firstly, the baseline cantilevered configuration and the two shrouded configurations with different clearance levels were considered to identify how the stator hub configurations impact the flow field and to find the regions of higher losses. The shrouded configuration with reduced clearances shows greater efficiency along the entire operational range compared to the other two configurations. However, the shrouded stator design with the same clearance level as the cantilevered stator configuration results in lower efficiency than the cantilevered one, whereas the configuration with a larger stall margin is the cantilevered. The design point analysis, based on the entropy loss coefficient, has shown, that distinct changes in the loss distribution can be observed starting from S7 in the lower 30% of the span. The two shrouded configurations have a similar loss distribution, with the configuration having larger clearances resulting in larger losses. When moving downstream, the differences in loss distribution between the three configurations become larger and more expanded across the span, for both rotors and stators. Although S11 is only indirectly affected by the changes of the upstream stators and its design is also kept as cantilevered in the shrouded configurations, visible differences are observed in the loss distribution. The near-stall analysis has highlighted that, when the hub configuration of the first four stators is changed, the row taking the compressor to stall also remains unchanged, even though, for the altered stators, the flow field differs at the hub. Indeed, both configurations are predicted to stall because of S11. We have also observed, that the cantilevered configuration has a large region of reverse flow on R8 which does not appear for the shrouded design with reduced clearances.

Successively, a parametric study was performed on a reduced 2.5-stage model, derived from the entire 5.5-stage model, to quantify the impact of some significant parameters and to improve the machine towards an optimum design. The reduced model consists of stage 8, stage 9, and R10. A configuration with shrouded vanes and one with cantilevered vanes was considered. The reduced model inlet coincides with the mixing plane between S7 and R8 in the entire model, and the boundary conditions used for the cantilevered and shrouded reduced models were taken from the numerical simulation of the entire model using their relative stator hub design. Using the reduced 2.5-stage model has allowed to perform the sensitivity study more quickly and to speed up the design process.

The parameters considered in the sensitivity study were: the clearance level, the degree of reaction, and the stator aerofoil near-endwall geometry. Only for the clearance study both the cantilevered and the shrouded configurations were investigated, whereas for the degree of reaction and the stator near-endwall geometry study, the shrouded configuration was considered. When changing the degree of reaction and near-endwall profile style, the same pressure ratio and incidence as the original shrouded configuration were maintained, which was the shrouded configuration with nominal clearances. Altering the clearances has an impact on the performance at the design point and on the stall margin, which decreases when the clearances are increased. In terms of degree of reaction, it was observed, that an increased reaction can result in a larger stall margin but has very little effect at the design point. However, if the degree of reaction increase is too large or if it decreases, the machine performance deteriorates. Moreover, an excessive increase of degree of reaction results in a reduced small margin. The results of the near-endwall profile geometry study have shown, that all the new camber line styles considered have a greater stall margin compared to the reference one and similar performance at the design point. Among them, the circular-arc style is the camber line distribution with a larger stall margin.

The sensitivity study revealed, that both the best degree of reaction and the best camber line distribution improve the performance towards the stall, while leaving it almost unchanged at the design point. For all the configurations considered in the sensitivity study, the near-stall analysis indicates R10 as the row taking the machine to stall. However, S9 can also have a strong impact on the stall margin. Thus, when the clearances are not changed, reducing the losses on S9 leads to a larger stall margin but does not affect the performance at the design point.

Lastly, two improved configurations featuring shrouded vanes were generated by combining the best versions of the sensitivity study. Both, a configuration with the baseline degree of reaction, and one with a limited increase of degree of reaction were investigated. The circular-arc camber line style was selected for the improved stator near-endwall configurations. The first improved configuration, OPT1, designed with the baseline degree of reaction and circular-arc camber line distribution in the hub section, resulted in slightly greater efficiency along most of the operational range and a larger stall margin when compared with the reference shrouded configuration and the cantilevered one. Different clearances were used for the shrouded and the cantilevered configuration: the three shrouded configurations, namely the reference one, OPT1 and OPT2, were equipped with reduced clearances, whereas nominal clearances were used for the cantilevered configuration. This choice was made to fairly compare the two stator hub configurations, as cantilevered stators normally require larger clearances than shrouded stators. The second improved configuration, OPT2, with an increased degree of reaction and circular-arc camber line distribution in the hub section, performs similarly to the reference shrouded configuration in terms of stall margin, whereas the efficiency varies along the operational range, being similar to the reference shrouded configuration for high mass flows and similar to OPT1 close to stall. This indicates, that the degree of reaction change reduces the improvement introduced by the change of the stator near-endwall profile style, and highlights that a sensitivity study of the best camber line distribution should be performed for every degree of reaction investigated. Considering the sensitivity towards the clearances, OPT1 performs similarly to the reference shrouded configuration, but OPT2 is less highly sensitive towards a clearance increase compared with the configurations having the original degree of reaction. OPT2's sensitivity is similar to that of the cantilevered configuration.

This study has demonstrated, that for a multi-stage axial compressor featuring shrouded stators, it is possible to improve the stall margin and the efficiency sensitivity to increased clearances by conveniently selecting the degree of reaction and the near-endwall profile geometry of the shrouded stators. However, only slight improvements at the design point were achieved.

Based on the extensive work carried out here, using high-resolution CFD simulations, the following recommendations for compressors designers are made:

- To improve the performance of a multi-stage machine, a dedicated parametric study should be carried out, even if only limited design parameters are changed

- Non-trivial results have to be expected when combining selections of clearances, degree of reaction, and camber line distribution at the hub

- When the degree of reaction is changed, a dedicated parametric study should be performed to identify a suitable and best near-endwall profile camber line distribution for the new degree of reaction selected

- Due to the large time required to design each aerofoil of the compressor, the parametric study should be automated and an optimizer added to the process. This would not only greatly speed up the design process and save engineering time, but also will allow to derive design choices to an absolute optimum in the design space.

5 Summary and overview

This study thoughtfully analyses the impact of the stator hub configurations for both a low-speed and a high-speed multi-stage subsonic axial compressor, equipped with both cantilevered and shrouded vanes. Choosing stator hub architecture is nowadays still very complicated despite the development of high performance computers in the recent years has allowed engineers to simulate, in detail, the flow field of a turbomachine configured with shrouded stators in which the cavities are entirely resolved and their effect on aerodynamic performance is fully considered. The choice between shrouded and cantilevered stator hub configuration needs to be made in the preliminary design of an axial compressor, as the stator architecture strongly impacts aerodynamic performance as well as the mechanical arrangement within the overall component design process. Generally, for a specific section of the compressor design, this choice is based on mechanical considerations; however, many aspects, such as weight and life, also play a fundamental role. In a multi-stage axial compressor arrangement, it is well known, that the hub configuration of a specific vane affects not only the vane itself, but also the rows located downstream.

In this work, two multi-stage axial compressors were numerically investigated with two main objectives. The first objective was to give further insight into aerodynamic loss generation and propagation in a multi-stage arrangement equipped with cantilevered or shrouded stators. For both styles of the machine, the work started from the baseline configuration, in which all the stators were configured as cantilevered. For the Dresden LSRC, only the third stator was altered from cantilevered to shrouded, maintaining the aerofoil geometry unchanged, whereas the other rows were not altered. For the high-speed compressor, the hub configuration of the first four stators was changed to shrouded and the thickness distribution adapted to the new design, leaving the other aerofoil parameters unchanged. For both machines two shrouded configurations were considered, which differed in their clearance level. Indeed, as shrouded vanes normally require smaller clearances than cantilevered ones, different clearances should be used to fairly compare the two designs. However, also a shrouded configuration with the same clearance level as the cantilevered was investigated. For the two shrouded configurations, the stator shroud cavities were fully meshed and resolved. The second objective of the work was to determine the specific machine's best parameters for a multi-stage axial compressor featuring shrouded stators. A sensitivity analysis was conducted on a reduced model of the high-speed compressor to investigate the impact of some selected parameters. These were: the clearance level, the degree of reaction, and the stator near-endwall profile geometry. The results of the sensitivity study were then used to configure two improved configurations with shrouded stator vanes, and to derive indications, that designers can use to identify an optimum design of a multi-stage axial compressor with shrouded stators.

For the Dresden LSRC, experimental data was available from the measurement taken by Lange [29]. These experimental results were compared to the numerical results of the compressor gained here in order to validate and prove the numerical results in those planes for which traverse data was available, thus verifying, that the CFD is able to correctly predict the dominant phenomena of the flow for both cantilevered and shrouded configurations. Then, the numerical data was used to further investigate the stator hub configuration's effects in those regions of interest for which experimental data could not be gathered or was simply not available. Considering the polytropic efficiency and the absolute total pressure ratio at the design flow for each compressor stage, we observed, that the first two stages were only slightly influenced by changing the third stator hub configuration. For the third stage, the shrouded configuration with greater clearances is less efficient compared to the other two configurations, whereas the absolute total pressure ratio is similar for the three configurations. The differences between the three configurations on stage three are a consequence of the altered hub design on the third stator. The fourth stage is the first stage downstream of the altered stator. There, large differences were observed between the three configurations, both in terms of efficiency and absolute total pressure ratio. The shrouded configurations with reduced clearances have greater efficiency and a higher total pressure ratio compared with the other two configurations. The cantilevered, however, has lower efficiency and a total pressure ratio similar to the shrouded configuration with larger clearance. The radial distributions of the deviation and the diffusion factor as well as radial distributions and the 2D contour plots of the total pressure loss coefficient explain the observed trend of the polytropic efficiency and the absolute total pressure ratio, and give further detailed insight to the secondary flow phenomena. They show, that the impact of the third stator hub configuration alteration on the aerodynamic performance is markedly high on the fourth rotor and unexpectedly low on the downstream stator, while being limited to the lower 50% of annulus height for both rows of the downstream stage.

Similarly to what was considered on the Dresden LSRC, the investigation of the 5.5-stage high-speed compressor was firstly focused on the regions of higher losses, their generation and their transmission in the multi-stage arrangements on both, the cantilevered and the two shrouded stator hub configurations. Because the 5.5-stage high-speed compressor included three bleeds, at S8, S9, and S11, and the bleed on S8 was moved from the gaspath hub surface to the bottom of the stator shroud cavity when the stator hub configuration was changed from cantilevered to shrouded, the efficiency based on the output power was used to physically correctly account for the bleeds in the compressor study. Comparing the overall performance of the three configurations, it was found, that the shrouded design with reduced clearances has higher efficiency across the entire operational range. However, when the clearances are increased to match those of the cantilevered configuration, efficiency decreases and is, at the same mass flow, lower than that achieved with the cantilevered design. The cantilevered design results in the configuration with a larger stall margin. The analysis at the design point has shown, that the loss distributions given on the three configurations differ for all rows except R7, with changes limited to 30% of the span. In general, the loss distributions of the two shrouded configurations follow a similar trend, with the shrouded configuration with larger clearances having larger near-endwall losses. Loss differences between the three configurations become larger and more expanded across the span when moving downstream. In particular, the loss distributions on S11 strongly react to the configurational change, although S11 remained cantilevered for all the configurations considered. The stall analysis has highlighted, that both the cantilevered and the shrouded configuration with reduced seal clearances stall because of a large suction side corner separation in the S11 hub region. Thus, although the flow field differs in the hub region when the stator hub design is modified, the present CFD analysis predicted, that the row triggering stall of the compressor remains unchanged.

Thereafter, the impact of some selected design parameters were investigated on a reduced model of the 5.5-stage original model. The parameters investigated were the radial gap/sealing clearance, the degree of reaction, and the stator near-endwall profile geometry. The reduced model, which consists of stage 8, stage 9, and rotor 10, has allowed to consistently speed up the design process. This applies in particular for the study of the degree of reaction and the stator near-endwall profile geometry, for which the flow coefficient and the work coefficient across the different designs considered were kept unchanged. For these two studies all the stators were configured as shrouded. On the reduced model, the clearance level was varied for both, the cantilevered and shrouded stator vane hub configurations. The cantilevered and the shrouded reduced models have been given individual inlet boundary conditions, derived from the respective 5.5-stage entire model configured with the shrouded or cantilevered stator hub architecture. The results of the sensitivity study were then used to identify two improved configurations, and to derive general recommendations for choosing improved parameters of a multi-stage axial compressor featuring shrouded stator vanes.

The clearance study was conducted by considering four different gap/sealing stator clearances ranging from 0.7 to 2.0 of the nominal clearances. For each configuration, the clearances of all the stators were equal, whereas the clearances of the rotors were left unchanged. An increase of clearances resulted in an efficiency and stall margin decrease for both the shrouded and the cantilevered configurations. At the design point operating conditions, the cantilevered configuration always performs better than the shrouded one if the same clearance level is used. Furthermore, the shrouded configuration is more sensitive to an increase of sealing clearance size compared to the cantilevered one. In the degree of reaction study, four different sets of blading were considered: the original one, which is the shrouded configuration with nominal clearances, two configurations with an increased degree of reaction, and one with a reduced degree of reaction. The study revealed, that the stall margin was slightly improved by increasing the degree of reaction, but the design point efficiency is only affected in a very limited manner. However, if the degree of reaction increase is too large, the stall margin is negatively affected. Additionally, a too large degree of reaction results in lower efficiency across most of the operational range, the efficiency being similar to that achieved with a decreased degree of reaction. The configuration with decreased degree of reaction shows lower efficiency across the entire operational range. The stator near-endwall profile geometry study was performed by identifying, using the 2D blade-to-blade tool MISES, three camber line distributions worth to be investigated in high-fidelity RANS simulations. The selected camber lines were introduced to the hub section of the stator vanes and blended into the existing section at 30% of the span, thus leaving the upper 70% of the stator geometry unchanged. All the new stator designs considered in the stator near-endwall geometry study resulted in an improved stall margin and efficiency in the near-stall region when compared to the original configuration, and left the performance characteristics at the design point almost unchanged. The camber line distribution giving the largest stall margin and efficiency is the circular-arc distribution.

The sensitivity study revealed that, when the clearance level is maintained unchanged, conveniently selecting the degree of reaction and the stator near-endwall profile geometry can have a major positive impact on the stall margin, but the performance at the design point mostly remain unaffected. For both cantilevered and shrouded configurations, an increase of the clearances reduces the design point efficiency and the stall margin. All the configurations considered in the sensitivity study run into stall driven by R10; however, the improved inlet flow condition on S9 has a very beneficial effect on the stall margin and the efficiency at throttled operating conditions in the upper part of the characteristic.

Two improved configurations, OPT1 and OPT2, were created by combining parameters found to be best in the individual sensitivity studies. The performance of the two improved configurations was compared with that of the reference shrouded configuration with reduced clearances, and that of the reference baseline cantilevered configuration with nominal clearances. This was done to address one the main goals of the project, which is to assess and compare the aerodynamic performance of the shrouded and cantilevered configurations. For both improved configurations, the circular-arc distribution was imposed at the hub of the shrouded stators and blended in at 30% of the stator using reduced clearances. The two improved configurations differ because of the degree of reaction: OPT1 has the same degree of reaction as the baseline configuration, whereas OPT2 has an increased degree of reaction, proven to improve the stall margin according to the degree of reaction study. A larger stall margin and greater efficiency along most of the operational range was achieved when the configuration OPT1 was compared to the reference shrouded configuration and the cantilevered one. In terms of efficiency sensitivity to an increase of clearance level, OPT1 follows a trend similar to that of the reference shrouded configuration, with greater sensitivity compared to the cantilevered configuration. OPT2, instead, has a stall margin comparable to the reference shrouded configuration, but is considerably less sensitive to an increase of clearances, similar to that of the cantilevered configuration. Therefore, it has been demonstrated, that conveniently selecting the degree of reaction and the stator near-endwall profile geometry for a multi-stage axial compressor featuring shrouded stators can lead to an improved configuration with a larger stall margin or reduced sensitivity to clearances.

The results indicate, that it is non-trivial to predict the performance of a multi-stage axial compressor when clearances, degree of reaction, and stator near-endwall profile geometry are modified. Therefore, for each degree of reaction considered, an individually optimised camber line distribution is to be identified using a dedicated sensitivity study. The impact of the clearances should be investigated for each new configuration designed. Beyond the scope of this thesis, further work should address a full automation of the design process developed here and should integrate an optimiser to exploit all the improvement potential indicated by the present investigations. It would not only save engineering time, but also allow designers to investigate the aerodynamic performance impact of even a larger amount of design parameters.

6 Appendix

A Near-wall mesh resolution

The mesh introduced in section 4.2 requires the use of wall functions to model the near-wall regions. The idea of the wall functions approach is, that instead of solving the turbulence model equations close to the wall, boundary conditions are applied at some distance away from the wall [74]. The law of the wall is used as the constructive relation between velocity and surface shear stress, and the first grid cell needs to be in the log-law region to ensure accurate results. Using the log-law to define boundary layer flow allows to significantly reduce the computational effort. The wall functions approach is largely used to limit the complications and the expense of performing detailed calculations of turbulent flows in the near-wall regions. Indeed, when a numerical study is conduced, a substantial fraction of the computational effort is devoted to the near-wall region. Using the log-law to define boundary layer flow allow to significantly reduce the computational effort.

A different approach for the wall treatment is the low-Reynolds wall condition. In this case, a finer mesh resolution close to the walls is required, since the viscous sub-layer has to be properly resolved. The averaged value of the distance from the wall normalized by the viscous length scale y^+, introduced in section 4.2, should be approximately 1. The low-Reynolds approach resolves the flow field in every detail without using any empirical function. It allows for a more accurate solution, but the computational time is considerably higher in comparison with the wall functions approach.

In this appendix, we validate the wall functions mesh selected in section 4.2, by comparing the numerical results against those achieved with a mesh with low-Reynolds wall treatment.

The details of the two meshes are given in Table A.1. The number of cells needed for the low-Reynolds mesh is sensibly higher in respect to those needed for the wall functions approach. The low-Reynolds mesh requires indeed 12 M cells, circa 3 M more that the wall functions mesh, and the solid wall cell width equal to $1e-6\ m$. A larger number of cells results in a longer computational time for each simulation.

Table A.1: HSC, near-wall mesh resolution, details of the low-Reynolds and wall functions meshes

	wall functions approach	low-Reynolds approach
Number of cells	9.5 M	12 M
Solid wall cell width	$5e-5\ m$	$1e-6\ m$

Figure A.1 compares the overall performance along the entire operational range achieved with the low-Reynolds and the wall functions mesh. Both for the isentropic efficiency and the absolute pressure ratio, the two approaches follow a very similar trend. However, at the same mass flow, the performance calculated with the low-Reynolds mesh is always greater than the one calculated with the wall functions approach. This indicates that the wall functions approach, by using empirical functions to resolve the near-wall turbulence structures, calculates larger losses in the machine. The offset between the two approaches is larger for the isentropic efficiency in the design point region. In terms of operational range, the two approaches show a similar trend.

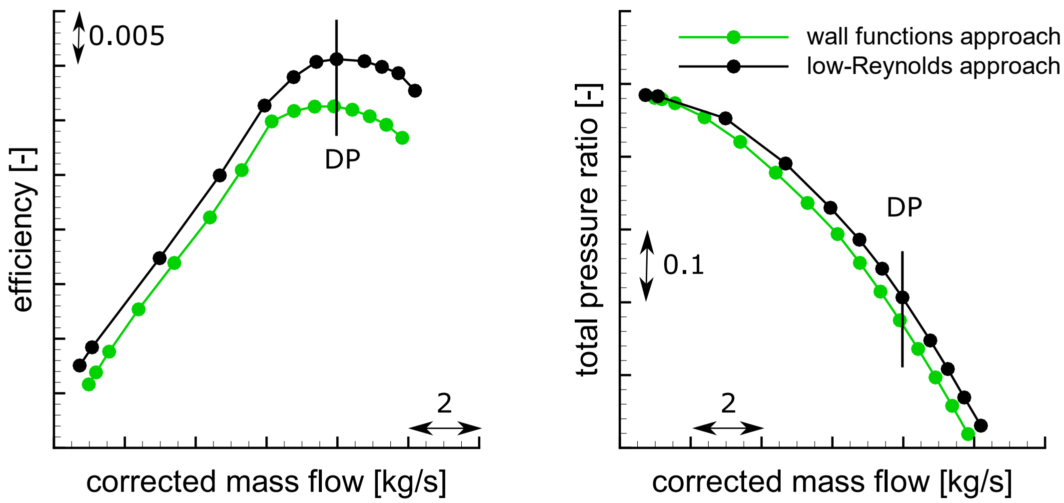

Figure A.1: HSC, near-wall mesh resolution, overall performance

Figures A.2 and A.3 depict the radial distribution of both normalized absolute total pressure ratio and axial velocity downstream of R7, S7, R8, S8, R9, S9, R10, S10, R11 and S11 at the design point. The corresponding mass-averaged value normalizes each quantity.

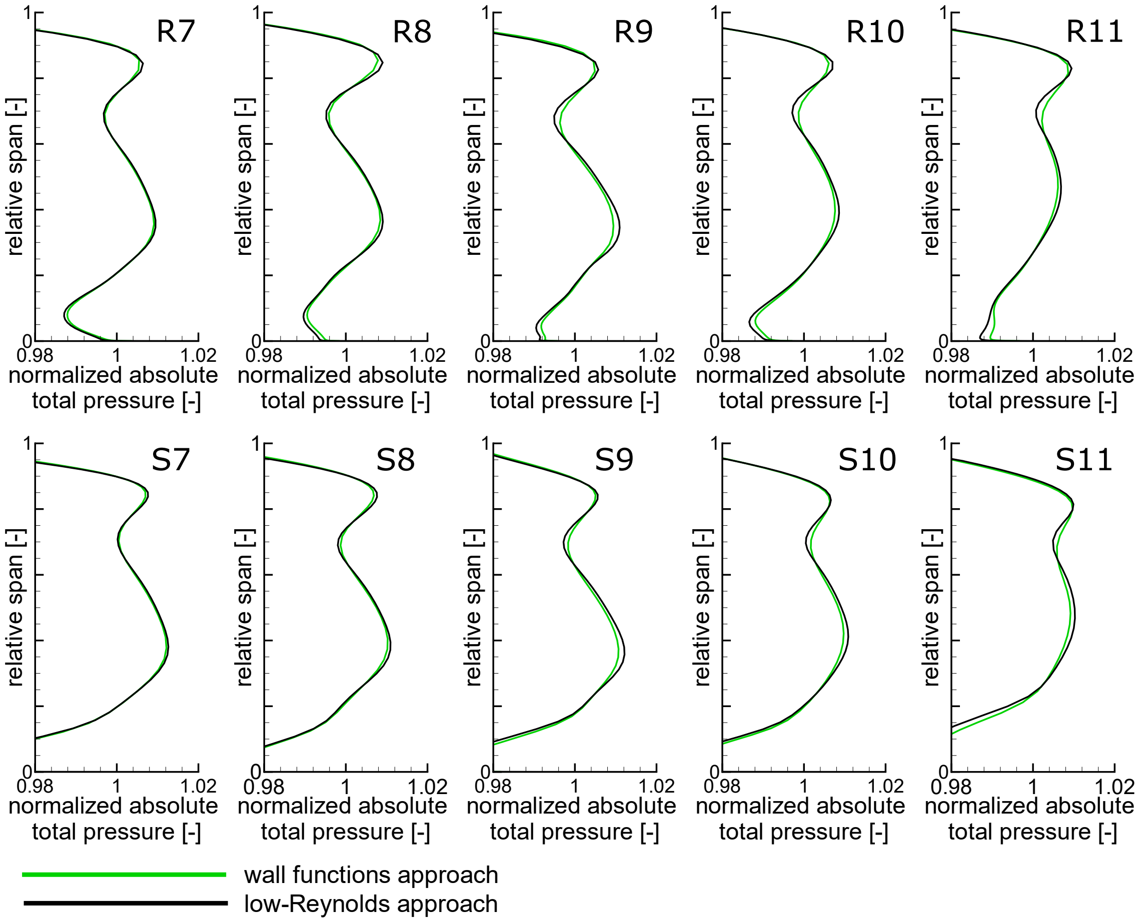

Figure A.2: HSC, near-wall mesh resolution, radial distributions of the normalized absolute total pressure at the DP operating conditions

Considering the normalized absolute total pressure, despite the trend being very similar, we observe small differences for each row. By moving downstream the differences become more evident and more expansive across the span. For both the rotors and the stators, at midspan the wall functions approach results in lower absolute pressure ratio. This is in agreement with the offset observed in Figure A.1 for the absolute total pressure ratio. However, for all the rows, the low-Reynolds approach has lower absolute total pressure ratio in the region between 60% and 80% of the span and greater absolute total pressure ratio in the region between 80% and 90% of the span. Close to the hub the wall functions mesh results, for each row, in larger absolute total pressure ratio. These differences result from the fact that the low-Reynolds resolves the flow field up to the wall, and by having a higher resolution takes into consideration more flow phenomena.

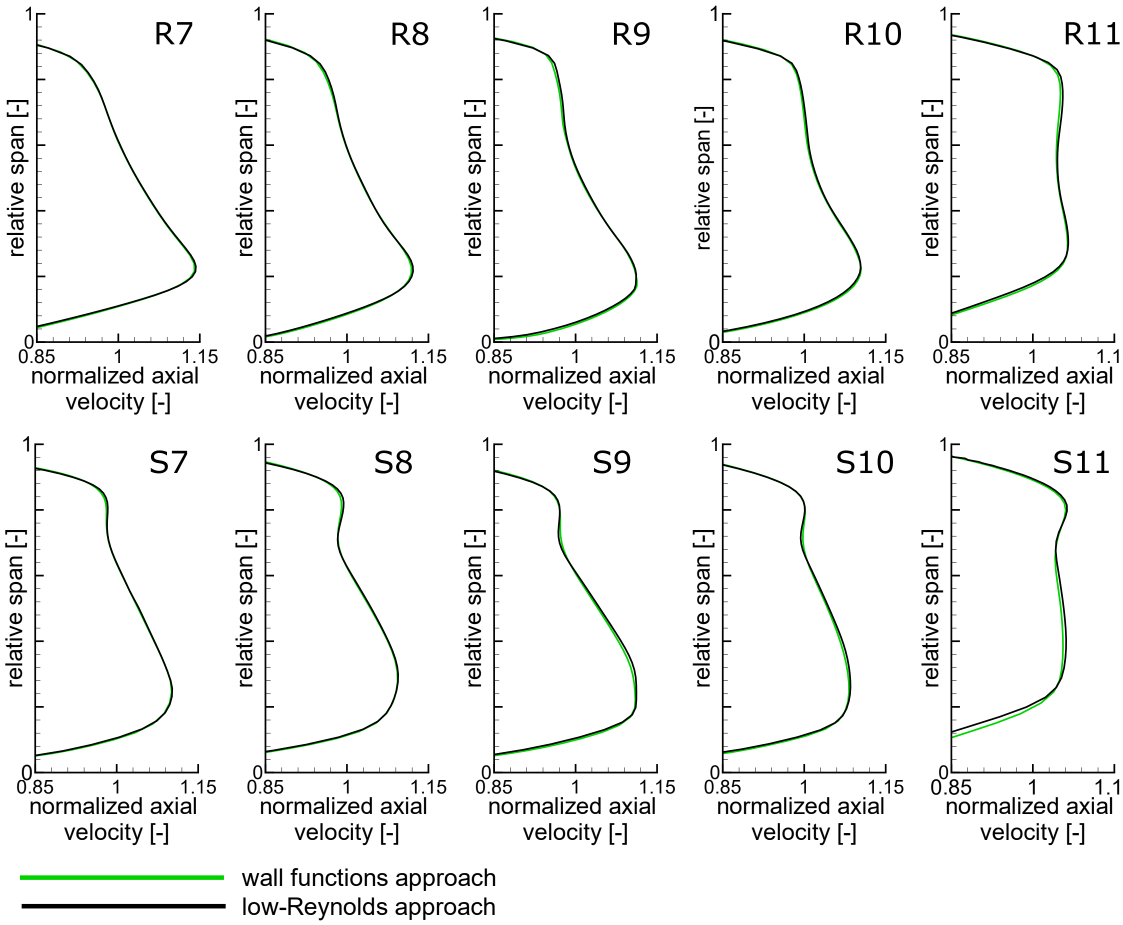

Figure A.3: HSC, near-wall mesh resolution, radial distributions of the normalized axial velocity at the DP operating conditions

In terms of normalized axial velocity, the differences are very limited for all rows and slightly larger for S11. There, in the region between 24% and 64% of the span, the axial velocity calculated with the wall function approach is lower, whereas it is higher in the region between 5% and 25% of the span.

Despite some small discrepancies, there is a very good agreement between the two approaches both for the normalized absolute total pressure ratio and the normalized axial velocity. This proves that the wall functions approach is able to capture flow phenomena sufficiently correctly, and permit to take the advantage of substantially reduced computational time.

B Near-stall analysis: shrouded configuration with nominal clearances

Figure B.1 depicts the radial distributions of the entropy change loss coefficient for each row of SNE at the three different corrected mass flow operating conditions DP, TS and NS highlighted in Figure 4.10.

In agreement with the loss distributions of CNE and SRE, depicted in Figure 4.13 and Figure 4.16 respectively, a back pressure increase from DP to NS operating conditions leads to a loss increase mostly limited to the tip region and to the hub

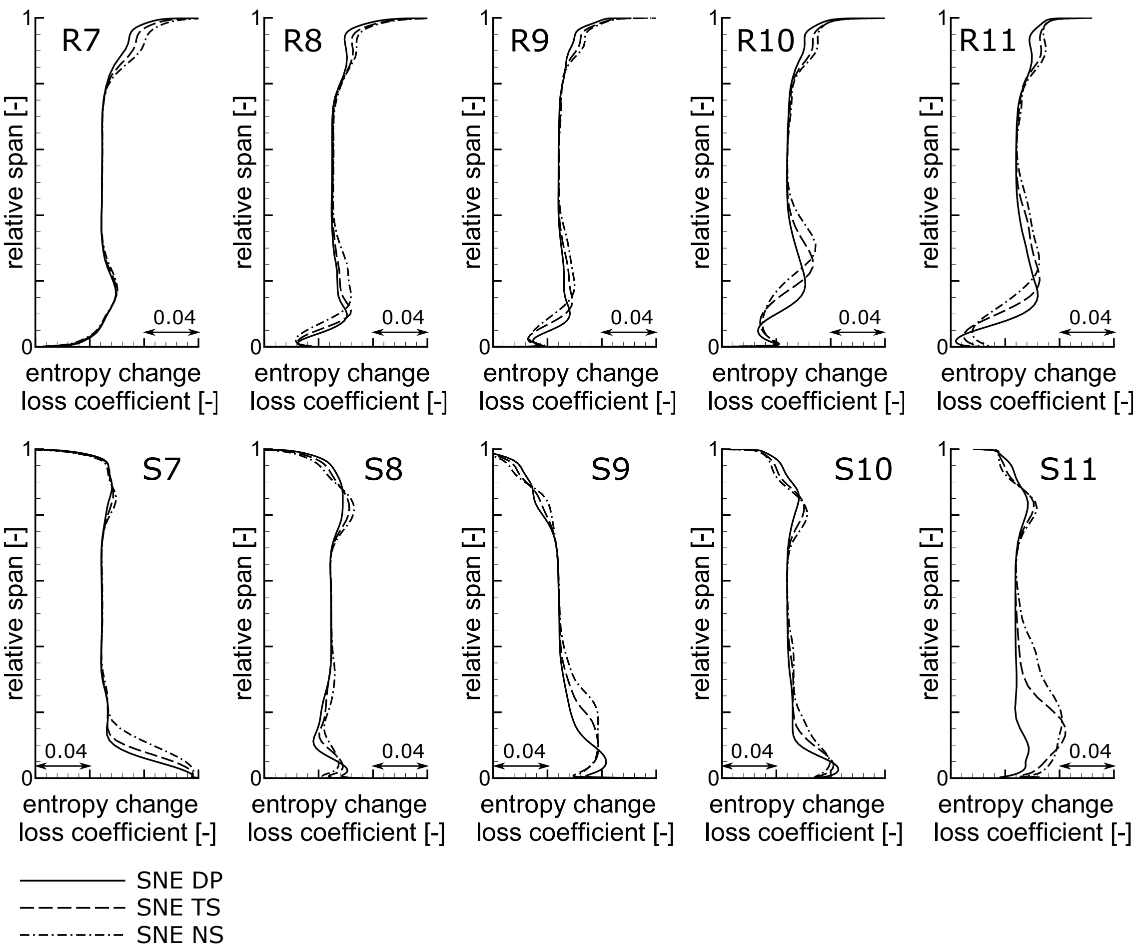

Figure B.1: HSC, entire model, radial distributions of the entropy change loss coefficient at the operating conditions DP, TS and NS for SNE region of R7 and S7. Starting with R8, there are changes both at the hub and at the tip.

On R8, between 8% and 40% of the span, a region of higher losses is observed for NS operating condition when compared with the operating conditions DP and TS. It is more extended than the one observed for SRE and results in larger losses on S8 between 18% and 36% of the span. Close to the hub, a very similar loss distributions to SRE occurs, even if the losses are visibly larger and more extended across the span. This, as seen for the design point analysis in Figure 4.12, is a consequence of the larger clearances used for SNE. The tip losses changes instead only slightly both for rotors and stators across the three configurations CNE, SRE and SNE.

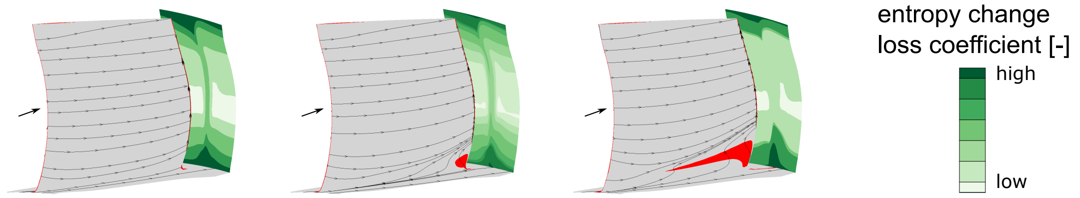

a) DP b) TS c) NS

Figure B.2: HSC, entire model, near-stall analysis for SNE. The regions of negative axial velocity on R8 are depicted in red and the entropy contours downstream of the stator trailing edge are depicted in green at the operating conditions DP, TS and NS

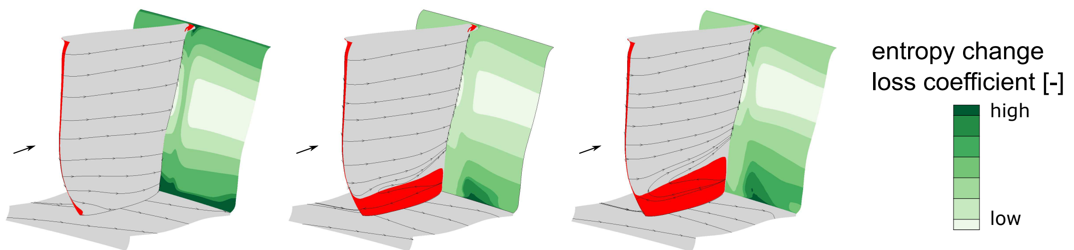

a) DP b) TS c) NS

Figure B.3: HSC, entire model, near-stall analysis for SNE. The regions of negative axial velocity on S11 are depicted in red and the entropy contours downstream of the stator trailing edge are depicted in green at the operating conditions DP, TS and NS

Similarly as for CNE and SRE, also for SNE the loss distributions of S11 increase drastically at TS and NS operating conditions. The losses extend up to 50% of the span at TS operating condition and 60% of the span at NS operating condition. The maximum value of losses is very close for both TS and NS operating conditions, and corresponds to the value of maximum loss for CNE and SRE.

The regions of reverse flow indicating separation, and the entropy contour distributions at the DP, TS and NS operating conditions are presented in Figure B.2 and in Figure B.3. For R8, depicted in Figure B.2, the reverse flow region at the NS operating condition is larger than the one observed for the SRE in Figure 4.17 but is still smaller that the one observed for CNE in Figure 4.14. At the near-stall operating condition, the region of reverse flow affects more than half of the chord length, however its extension towards the span is limited. In Figure B.3, S11 shows similar regions of reverse flow as those observed for CNE in Figure 4.15 and SRE in Figure 4.18. Therefore, the change in stator hub configuration of the first 4 stators has not changed the stall behaviour of the machine. S11 is the row taking the machine to numerical stall not only for the CNE and SRE configurations, but also SNE.

C Isentropic Mach number distributions of the rotors

C.1 Endwall profile study

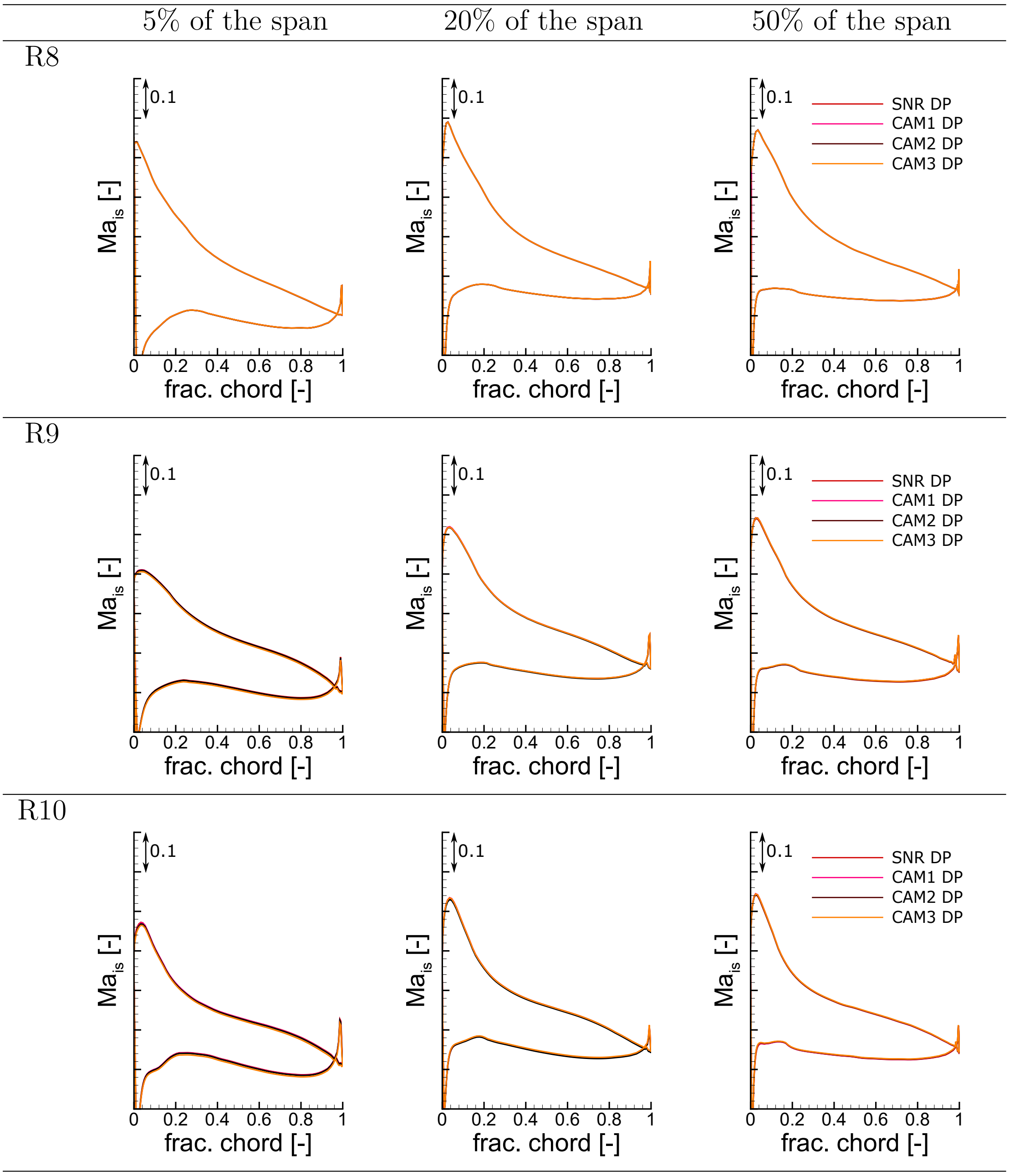

Figure C.1: HSC, endwall profile study, profile isentropic Mach number distributions for R8, R9 and R10 at 5%, 20% and 50% of the span at the DP operating conditions

C.2 Improved configurations

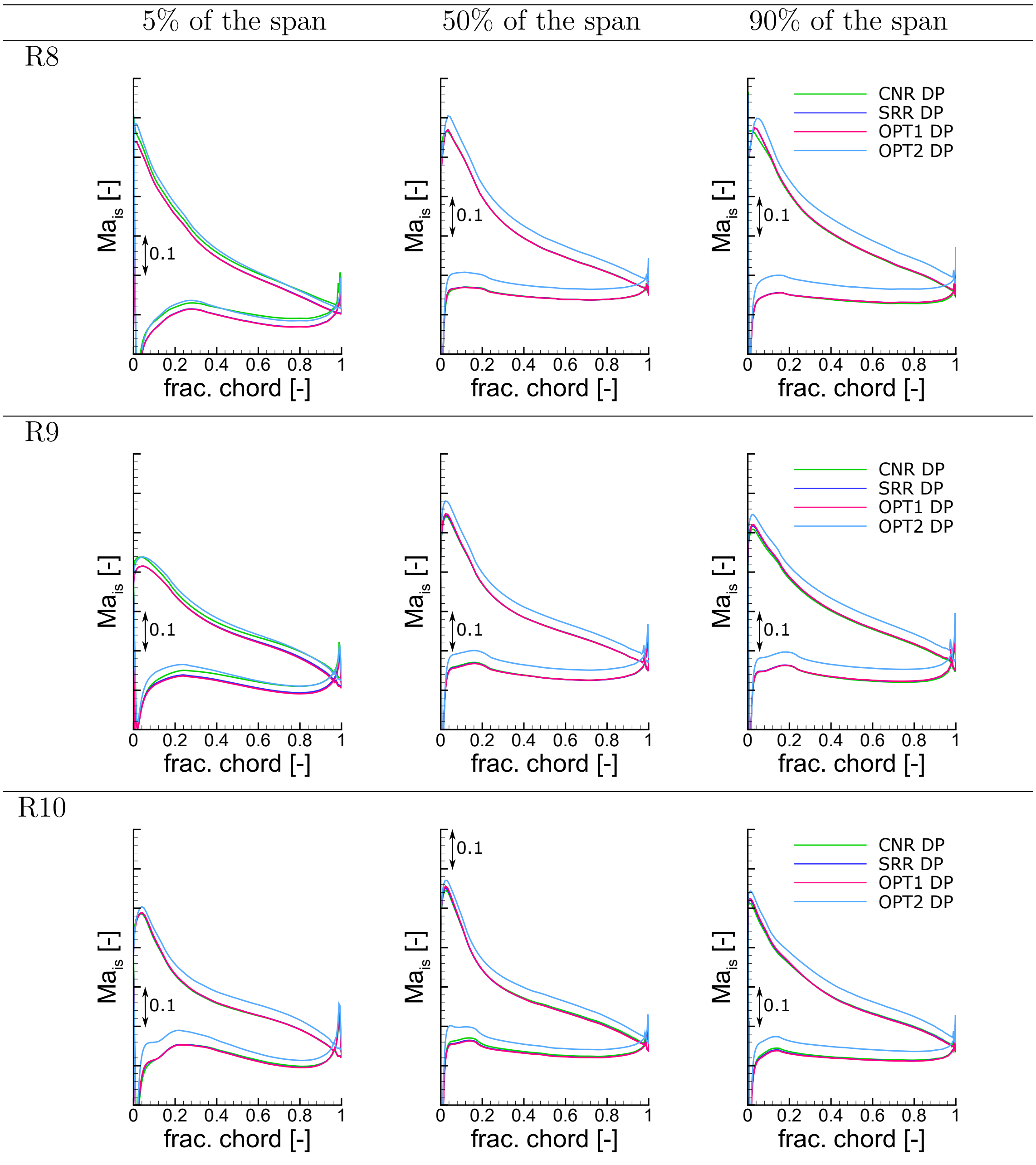

Figure C.2: HSC, improved configurations, profile isentropic Mach number distributions for R8, R9 and R10 at 5%, 50% and 90% of the span at the DP operating conditions

D Content re-use license

Marketplace™

This is a License Agreement between Ilaria De Dominicis ("User") and Copyright Clearance Center, Inc. ("CCC") on behalf of the Rightsholder identified in the order details below. The license consists of the order details, the CCC Terms and Conditions below, and any Rightsholder Terms and Conditions which are included below.

All payments must be made in full to CCC in accordance with the CCC Terms and Conditions below.

Order Date	17-May-2022	**Type of Use**	Republish in a thesis/dissertation
Order License ID	1222388-1	**Publisher**	AMERICAN INSTITUTE OF AERONAUTICS AND ASTRONAUTICS, INC.
ISSN	1533-3876	**Portion**	Chapter/article

LICENSED CONTENT

Publication Title	Journal of propulsion and power	**Publication Type**	e-Journal
Article Title	Interacting Effects in a Multistage Axial Compressor Using Shrouded and Cantilevered Stators	**Start Page**	615
Author/Editor	American Institute of Aeronautics and Astronautics.	**End Page**	624
Date	01/01/1985	**Issue**	4
Language	English	**Volume**	37
Country	United States of America	**URL**	http://www.catchword.com/rpsv/catchword/aiaa/07484658/contp1-1.htm
Rightsholder	American Inst of Aeronautics & Astronautics (AIAA)		

REQUEST DETAILS

Portion Type	Chapter/article	**Rights Requested**	Main product
Page range(s)	1-10	**Distribution**	Worldwide
Total number of pages	10	**Translation**	Original language of publication
Format (select all that apply)	Print, Electronic	**Copies for the disabled?**	No
Who will republish the content?	Academic institution	**Minor editing privileges?**	Yes
Duration of Use	Life of current and all future editions	**Incidental promotional use?**	No
Lifetime Unit Quantity	Up to 999	**Currency**	EUR

NEW WORK DETAILS

Title	Numerical Investigation of Stator Hub Configurations in Axial Flow Compressors	**Institution name**	Technical University of Munich
Instructor name	Prof. Dr.-Ing. Volker Gümmer	**Expected presentation date**	2023-03-01

ADDITIONAL DETAILS

Order reference number	N/A	**The requesting person / organization to appear on the license**	Ilaria De Dominicis

REUSE CONTENT DETAILS

Title, description or numeric reference of the portion(s)	Numerical Investigation of Stator Hub Configurations in Axial Flow Compressors	**Title of the article/chapter the portion is from**	Interacting Effects in a Multistage Axial Compressor Using Shrouded and Cantilevered Stators
Editor of portion(s)	De Dominicis, Ilaria; Robens, Sebastian; Wolfrum, Nina; Lange, Martin; Gümmer, Volker	**Author of portion(s)**	De Dominicis, Ilaria; Robens, Sebastian; Wolfrum, Nina; Lange, Martin; Gümmer, Volker
Volume of serial or monograph	37	**Issue, if republishing an article from a serial**	4
Page or page range of portion	615-624	**Publication date of portion**	2021-07-01

RIGHTSHOLDER TERMS AND CONDITIONS

Verification of copyright ownership is your responsibility. You should only submit requests for materials that are owned by AIAA. Please review the copyright statement for the source material before submitting a reprint permission request, to ensure that AIAA is the copyright owner: For AIAA meeting papers, journal papers, or books with independently authored chapters (e.g., many Progress Series volumes), look at the bottom of the first full-text page (not the cover page). There will be a footnote indicating who holds copyright. For other books, look at the copyright statement on the back of the title page. If the statement reads "Copyright by the American Institute of Aeronautics and Astronautics, Inc.," then AIAA is the copyright owner, and you may submit your request. If the statement reads otherwise, AIAA does not hold copyright, and cannot grant permission to reprint. You must seek permission from the copyright owner rather than AIAA. Preferred credit line for reprinted material: From [original title and authors]; reprinted by permission of the American Institute of Aeronautics and Astronautics, Inc. Note that the original source also should be cited in full in the reference list.

SPECIAL RIGHTSHOLDER TERMS AND CONDITIONS

Please acknowledge within the main text or a footnote that relevant sections/chapters of your thesis/dissertation are reprinted with permission (e.g., “From [paper title and authors]; reprinted by permission of the American Institute of Aeronautics and Astronautics, Inc.”). Note that the original source should be cited in full in the reference list.

CCC Terms and Conditions

1. Description of Service; Defined Terms. This Republication License enables the User to obtain licenses for republication of one or more copyrighted works as described in detail on the relevant Order Confirmation (the "Work(s)"). Copyright Clearance Center, Inc. ("CCC") grants licenses through the Service on behalf of the rightsholder identified on the Order Confirmation (the "Rightsholder"). "Republication", as used herein, generally means the inclusion of a Work, in whole or in part, in a new work or works, also as described on the Order Confirmation. "User", as used herein, means the person or entity making such republication.

2. The terms set forth in the relevant Order Confirmation, and any terms set by the Rightsholder with respect to a particular Work, govern the terms of use of Works in connection with the Service. By using the Service, the person transacting for a republication license on behalf of the User represents and warrants that he/she/it (a) has been duly authorized by the User to accept, and hereby does accept, all such terms and conditions on behalf of User, and (b) shall inform User of all such terms and conditions. In the event such person is a "freelancer" or other third party independent of User and CCC, such party shall be deemed jointly a "User" for purposes of these terms and conditions. In any event, User shall be deemed to have accepted and agreed to all such terms and conditions if User republishes the Work in any fashion.

3. Scope of License; Limitations and Obligations.

    3.1. All Works and all rights therein, including copyright rights, remain the sole and exclusive property of the Rightsholder. The license created by the exchange of an Order Confirmation (and/or any invoice) and payment by User of the full amount set forth on that document includes only those rights expressly set forth in the Order Confirmation and in these terms and conditions, and conveys no other rights in the Work(s) to User. All rights not expressly granted are hereby reserved.

    3.2. General Payment Terms: You may pay by credit card or through an account with us payable at the end of the month. If you and we agree that you may establish a standing account with CCC, then the following terms apply: Remit Payment to: Copyright Clearance Center, 29118 Network Place, Chicago, IL 60673-1291. Payments Due: Invoices are payable upon their delivery to you (or upon our notice to you that they are available to you for downloading). After 30 days, outstanding amounts will be subject to a service charge of 1-1/2% per month or, if less, the maximum rate allowed by applicable law. Unless otherwise specifically set forth in the Order Confirmation or in a separate written agreement signed by CCC, invoices are due and payable on "net 30" terms. While User may exercise the rights licensed immediately upon issuance of the Order Confirmation, the license is automatically revoked and is null and void, as if it had never been issued, if complete payment for the license is not received on a timely basis either from User directly or through a payment agent, such as a credit card company.

    3.3. Unless otherwise provided in the Order Confirmation, any grant of rights to User (i) is "one-time" (including the editions and product family specified in the license), (ii) is non-exclusive and non-transferable and (iii) is subject to any and all limitations and restrictions (such as, but not limited to, limitations on duration of use or circulation) included in the Order Confirmation or invoice and/or in these terms and conditions. Upon completion of the licensed use, User shall either secure a new permission for further use of the Work(s) or immediately cease any new use of the Work(s) and shall render inaccessible (such as by deleting or by removing or severing links or other locators) any further copies of the Work (except for copies printed on paper in accordance with this license and still in User's stock at the end of such period).

    3.4. In the event that the material for which a republication license is sought includes third party materials (such as photographs, illustrations, graphs, inserts and similar materials) which are identified in such material as having been used by permission, User is responsible for identifying, and seeking separate licenses (under this Service or otherwise) for, any of such third party materials; without a separate license, such third party materials may not be used.

    3.5. Use of proper copyright notice for a Work is required as a condition of any license granted under the Service. Unless otherwise provided in the Order Confirmation, a proper copyright notice will read substantially as follows: "Republished with permission of [Rightsholder's name], from [Work's title, author, volume, edition number and year of copyright]; permission conveyed through Copyright Clearance Center, Inc. " Such notice must be provided in a reasonably legible font size and must be placed either immediately adjacent to the Work as used (for example, as part of a by-line or footnote but not as a separate electronic link) or in the place where substantially all other credits or notices for the new work containing the republished Work are located. Failure to include the required notice results in loss to the Rightsholder and CCC, and the User shall be liable to pay liquidated damages for each such failure equal to twice the use fee specified in the Order Confirmation, in addition to the use fee itself and any other fees and charges specified.

    3.6. User may only make alterations to the Work if and as expressly set forth in the Order Confirmation. No

Work may be used in any way that is defamatory, violates the rights of third parties (including such third parties' rights of copyright, privacy, publicity, or other tangible or intangible property), or is otherwise illegal, sexually explicit or obscene. In addition, User may not conjoin a Work with any other material that may result in damage to the reputation of the Rightsholder. User agrees to inform CCC if it becomes aware of any infringement of any rights in a Work and to cooperate with any reasonable request of CCC or the Rightsholder in connection therewith.

4. Indemnity. User hereby indemnifies and agrees to defend the Rightsholder and CCC, and their respective employees and directors, against all claims, liability, damages, costs and expenses, including legal fees and expenses, arising out of any use of a Work beyond the scope of the rights granted herein, or any use of a Work which has been altered in any unauthorized way by User, including claims of defamation or infringement of rights of copyright, publicity, privacy or other tangible or intangible property.

5. Limitation of Liability. UNDER NO CIRCUMSTANCES WILL CCC OR THE RIGHTSHOLDER BE LIABLE FOR ANY DIRECT, INDIRECT, CONSEQUENTIAL OR INCIDENTAL DAMAGES (INCLUDING WITHOUT LIMITATION DAMAGES FOR LOSS OF BUSINESS PROFITS OR INFORMATION, OR FOR BUSINESS INTERRUPTION) ARISING OUT OF THE USE OR INABILITY TO USE A WORK, EVEN IF ONE OF THEM HAS BEEN ADVISED OF THE POSSIBILITY OF SUCH DAMAGES. In any event, the total liability of the Rightsholder and CCC (including their respective employees and directors) shall not exceed the total amount actually paid by User for this license. User assumes full liability for the actions and omissions of its principals, employees, agents, affiliates, successors and assigns.

6. Limited Warranties. THE WORK(S) AND RIGHT(S) ARE PROVIDED "AS IS". CCC HAS THE RIGHT TO GRANT TO USER THE RIGHTS GRANTED IN THE ORDER CONFIRMATION DOCUMENT. CCC AND THE RIGHTSHOLDER DISCLAIM ALL OTHER WARRANTIES RELATING TO THE WORK(S) AND RIGHT(S), EITHER EXPRESS OR IMPLIED, INCLUDING WITHOUT LIMITATION IMPLIED WARRANTIES OF MERCHANTABILITY OR FITNESS FOR A PARTICULAR PURPOSE. ADDITIONAL RIGHTS MAY BE REQUIRED TO USE ILLUSTRATIONS, GRAPHS, PHOTOGRAPHS, ABSTRACTS, INSERTS OR OTHER PORTIONS OF THE WORK (AS OPPOSED TO THE ENTIRE WORK) IN A MANNER CONTEMPLATED BY USER; USER UNDERSTANDS AND AGREES THAT NEITHER CCC NOR THE RIGHTSHOLDER MAY HAVE SUCH ADDITIONAL RIGHTS TO GRANT.

7. Effect of Breach. Any failure by User to pay any amount when due, or any use by User of a Work beyond the scope of the license set forth in the Order Confirmation and/or these terms and conditions, shall be a material breach of the license created by the Order Confirmation and these terms and conditions. Any breach not cured within 30 days of written notice thereof shall result in immediate termination of such license without further notice. Any unauthorized (but licensable) use of a Work that is terminated immediately upon notice thereof may be liquidated by payment of the Rightsholder's ordinary license price therefor; any unauthorized (and unlicensable) use that is not terminated immediately for any reason (including, for example, because materials containing the Work cannot reasonably be recalled) will be subject to all remedies available at law or in equity, but in no event to a payment of less than three times the Rightsholder's ordinary license price for the most closely analogous licensable use plus Rightsholder's and/or CCC's costs and expenses incurred in collecting such payment.

8. Miscellaneous.

   8.1. User acknowledges that CCC may, from time to time, make changes or additions to the Service or to these terms and conditions, and CCC reserves the right to send notice to the User by electronic mail or otherwise for the purposes of notifying User of such changes or additions; provided that any such changes or additions shall not apply to permissions already secured and paid for.

   8.2. Use of User-related information collected through the Service is governed by CCC's privacy policy, available online here:https://marketplace.copyright.com/rs-ui-web/mp/privacy-policy

   8.3. The licensing transaction described in the Order Confirmation is personal to User. Therefore, User may not assign or transfer to any other person (whether a natural person or an organization of any kind) the license created by the Order Confirmation and these terms and conditions or any rights granted hereunder; provided, however, that User may assign such license in its entirety on written notice to CCC in the event of a transfer of all or substantially all of User's rights in the new material which includes the Work(s) licensed under this Service.

8.4. No amendment or waiver of any terms is binding unless set forth in writing and signed by the parties. The Rightsholder and CCC hereby object to any terms contained in any writing prepared by the User or its principals, employees, agents or affiliates and purporting to govern or otherwise relate to the licensing transaction described in the Order Confirmation, which terms are in any way inconsistent with any terms set forth in the Order Confirmation and/or in these terms and conditions or CCC's standard operating procedures, whether such writing is prepared prior to, simultaneously with or subsequent to the Order Confirmation, and whether such writing appears on a copy of the Order Confirmation or in a separate instrument.

8.5. The licensing transaction described in the Order Confirmation document shall be governed by and construed under the law of the State of New York, USA, without regard to the principles thereof of conflicts of law. Any case, controversy, suit, action, or proceeding arising out of, in connection with, or related to such licensing transaction shall be brought, at CCC's sole discretion, in any federal or state court located in the County of New York, State of New York, USA, or in any federal or state court whose geographical jurisdiction covers the location of the Rightsholder set forth in the Order Confirmation. The parties expressly submit to the personal jurisdiction and venue of each such federal or state court.If you have any comments or questions about the Service or Copyright Clearance Center, please contact us at 978-750-8400 or send an e-mail to support@copyright.com.

v 1.1

Bibliography

[1] M. Lange, R. Mailach, and K. Vogeler: *An experimental investigation of shrouded and cantilevered compressor stators at varying clearance sizes*. ASME Conference Proceedings, Paper No. GT2010-22106, 2010.

[2] M. T. Schobeiri: *Gas Turbine Design, Components and System Design Integration*. Springer, 2019.

[3] N. A. Cumpsty: *Compressor Aerodynamics*. Krieger Publishing Company, 2004.

[4] J. L. Jefferson and R. C. Turner: *Some shrouding and tip clearance effects in axial flow compressor*. International Ship Building Progress, Vol 5: 78–101, 1958.

[5] C. Freeman: *Effect of tip clearance flow on compressor stability and engine performance: tip clearance effects in axial turbomachines*. Von Karman Institute for Fluid Dynamics, Lecture Series 1985-05, 1985.

[6] N. J. Heidegger, E. J. Hall, and R. A. Delaney: *Stator seal cavity flow investigation*. NASA Contractor Report 198504, 1996.

[7] M. Swoboda, P. C. Ivey, U. Wenger, and V. Gümmer: *An experimental examination of cantilevered and shrouded stators in a multistage axial compressor*. ASME Conference Proceedings, Paper No. 98-GT-282, 1998.

[8] S. Yoon, R. Selmeier, P. Cargill, and P. Wood: *Effect of the stator hub configuration and stage design parameters on aerodynamic loss in axial compressors*. Journal of Turbomachinery, 137(9):091001, 2015.

[9] D. C. Wisler: *Advanced compressor and fan systems*. GE Aircraft Engine, 1985.

[10] M. S. Campobasso, A. Mattheiss, U. Wenger, A. Amone, and P. Boncinelli: *Complementary Use of CFD and Experimental Measurements to Assess the Impact of Shrouded and Cantilevered Stators in Axial Compressors*. ASME Conference Proceedings, Paper No. 99-GT-208, 1999.

[11] L. Beermann, J. Wilhelm, C. Höfler, and H. Bauer: *Experimental investigation of the sealing performance of a new adaptive seal system*. Proceedings of GPPS Forum 18, Paper No. 5, 2018.

[12] J. D. Denton: *Loss mechanisms in turbomachines*. Journal of Turbomachinery, 115(4): 621-656, 1993.

[13] L. H. Smith: *Wake dispersion in turbomachines*. Journal of Fluids Engineering, 88(3): 688-690, 1966.

[14] J. Denecke, K. Dullenkopf, S. Wittig, and H. J. Bauer: *Experimental investigation of the total temperature increase and swirl development in rotating labyrinth seals*. ASME Conference Proceedings, Paper No. GT2005-68677, 2005.

[15] C. A. Meyer and J. A. Lowrie: *Leakage thru straight and slant labyrinths and honeycomb seals*. Journal of Engineering for Gas Turbines and Power, 97(4): 495-501, 1975.

[16] G. K. Arora and M. P. Proctor: *JTAGG II brush seal test results*. NASA Technical Memorandum 107448, 1997.

[17] I. R. Delgado and M. P. Proctor: *Continued investigation of leakage and power loss test results for competing turbine engine seals*. NASA Technical Memorandum 214420, 2006.

[18] L. S. Andrés, J. Baker, and A. Delgado: *Measurements of leakage and power loss in a hybrid brush seal*. Journal of Engineering for Gas Turbines and Power, 131(1): 012505, 2009.

[19] S. R. Wellborn and T. H. Okiishi *Effects of Shrouded Stator Cavity Flows on Multistage Axial Compressor Aerodynamic Performance.* NASA Contractor Report 198536, 1996.

[20] N. J. Heidegger, E. J. Hall, and R. A. Delaney: *Parameterized study of high-speed compressor seal cavity flow.* AIAA, Paper No. 96-2807, 1996.

[21] S. R. Wellborn and T. H. Okiishi: *The influence of shrouded stator cavity flows on multistage compressor performance.* Journal of Turbomachinery, 121(3): 486-497, 1999.

[22] A. A. J. Demargne and J. P. Longley: *The aerodynamic interaction of stator shroud leakage and mainstream flows in compressors.* ASME Conference Proceedings, Paper No. 2000-GT-0570, 2000.

[23] D. W. Sohn, T. Kim, and S. J. Song: *Influence of the leakage flow tangential velocity on the loss generation and leakage flow kinematics in shrouded axial compressor cascades*, ASME Conference Proceedings, Paper No. GT2006-90979, 2006.

[24] H. K. Ozturk, P. R. N. Childs, A. B. Turner, J. M. Hannis, and J. R. Turner: *A three dimensional computational study of windage heating within an axial compressor stator well.* ASME Conference Proceedings, Paper No. 98-GT-119, 1998.

[25] J. W. Kim, S. J. Song, and T. Kim: *Streamwise evolution of loss in a shrouded axial compressor cascade passage.* Journal of Propulsion and Power, 27(4), 2011.

[26] M. Lange, R. Mailach, and K. Vogeler: *An experimental investigation of shrouded and cantilevered compressor stators at varying clearance sizes.* ASME Conference Proceedings, Paper No. GT2010-22106, 2010.

[27] D. Flores and J. R. Seume: *Selecting cavity geometries for improving the aerodynamic performance of an axial compressor.* ASME Conference Proceedings, Paper No. GT2014-25328, 2014.

[28] I. De Dominicis, S. Robens, N. Wolfrum, M. Lange, and V. Gümmer: *Interacting effects in a multistage axial compressor using shrouded and cantilevered stators.* Journal of Propulsion and Power, 37(4):615-624, 2021.

[29] M. Lange: *Strömungsmechanische Untersuchungen an Axialverdichter-Statoren mit und ohne Deckband bei großen Spaltweiten.* Doctoral thesis, TUDpress, Volume 7, 2014.

[30] R. Müller, R. Mailach and I. Lehmann: *The design and construction of a four-stage low-speed research compressor.* Proceedings of the IMP '97 Conference on Modelling and Design in Fluid-Flow Machinery, 1997.

[31] P. Boos, H. Möckel, J. M. Henne, and R. Selmeier: *Flow measurement in a multistage large scale low speed axial flow research compressor.* ASME Conference Proceedings, Paper No. 98-GT-432, 1998.

[32] H. Bernhard, T. Biesinger, P. Boos, H. Sauer, W. Bernstein and H. Möckel: *Konstruktion, Fertigung und Aufbau eines Verdichterprüfstandes und Aufnahme des Versuchsbetriebes an einem Niedergeschwindigkeits-Axialverdichter in Dresden.* Abschlussbericht zum BMBF-Vorhaben 0326758A, 1996.

[33] D. Nürnberger, F. Eulitz, S. Schmitt, and A. Zachcial: *Recent progress in the numerical simulation of unsteady viscous multistage turbomachinery flow.* ISOABE, Paper No. 2001-1081, 2001.

[34] S. B. Pope: *Turbulent Flows.* Cambridge University Press, 2000.

[35] D. C. Wilcox: *Reassessment of the scale-determining equation for advanced turbulence models.* AIAA Journal, 26(11):1299–1310, 1988.

[36] D.C. Wilcox: *Turbulence modeling for CFD.* DCW Industries, 2006.

[37] *TRACE User Guide, TRACE version 9.0.444.* DLR, 2017.

[38] F. Eulitz, K. Engel, D. Nuernberger, S. Schmitt, and K. Yamamoto: *On recent advances of a parallel time-accurate navier-stokes solver for unsteady turbomachinery flow.* Proceedings of the 4th European Computational Fluid Dynamics Conference, 1:252–258, 1998.

[39] K. Engel: *Numerische Simulation der instationären strömung in Turbomaschinenkomponenten.* Doctoral thesis, DLR-Forschungsbericht 97-19, 1997.

[40] D. Nürnberger: *Implizite Zeitintegration für die Simulation von Turbomaschinenströmungen.* Doctoral Thesis, Ruhr-Universität Bochum, Universitätsbibliothek, 2004.

[41] E. Kügeler: *Numerisches Verfahren zur genauen Analyse der Kühleffektivität filmgekühlter Turbinenschaufeln.* Doctoral Thesis, Ruhr-Universität Bochum, Universitätsbibliothek, 2005.

[42] A. Harten and J. M. Hyman: *Self adjusting grid methods for one-dimensional hyperbolic conservation laws.* Journal of Computational Physics, 50(2):235-269, 1983.

[43] P. L. Roe: *Approximate Riemann solvers, parameter vectors, and difference schemes.* Journal of Computational Physics, 43(2):357-372, 1981.

[44] J. E. Fromm: *A method for reducing dispersion in convective difference schemes.* Journal of Computational Physics, 3(2):176-189, 1968.

[45] N. Wolfrum: *Trace/gmc user's guide.* MTU Aero Engines Report, 2016.

[46] M. B. Giles: *Nonreflecting boundary conditions for Euler equation calculations.* AIAA Journal, 28(12):2050–2058, 1990.

[47] A. P. Saxer and M. B. Giles: *Quasi-three-dimensional nonreflecting boundary conditions for Euler equations calculations.* Journal of Propulsion and Power, 9(2):263–271, 1993.

[48] P. J. Roache: *Verification of codes and calculations.* AIAA Journal, 36(5):696–702, 1998.

[49] G. G. Jr. Adkins and L. H. Jr. Smith: *Spanwise Mixing in Axial-Flow Turbomachines.* Journal of Engineering for Gas Turbines and Power, 104(1):97–110, 1982.

[50] T. Fröebel, H.-P. Kau, C. Groth, and V. Gümmer: *Numerical investigation of unsteady flow phenomena in an hp axial flow compressor incorporating stator shroud cavities.* AIAA, Paper No. 2010-6532, 2012.

[51] I. De Dominicis, S. Robens, and V. Gümmer: *Numerical Evaluation of Losses in Shrouded and Cantilevered Stators of a Multi-Stage Axial Compressor.* ASME Conference Proceedings, Paper No. GT2021-58388, 2021.

[52] H. Yang, D. Nuernberger, E. Nicke, and A. Weber: *Numerical Investigation of Casing Treatment Mechanisms with a Conservative Mixed-Cell Approach.* ASME Conference Proceedings, Paper No. GT2003-38483, 2003.

[53] F. R. Menter, M. Kuntz, and R. Langtry: *Ten Years of Industrial Experience with the SST Turbulence Model Turbulence Heat and Mass Transfer.* Proceedings of the 4th International Symposium on Turbulence, Heat and Mass Transfer, 625-632, 2003.

[54] W. Rodi and G. Scheuerer: *Scrutinizing the κ-ϵ turbulence model under adverse pressure gradient conditions.* Journal of Fluids Engineering, 108(2): 174-179,

1986.

[55] D. A. Johnson and L. S. King: *A mathematically simple turbulence closure model for attached and separated turbulent boundary layers*. AIAA Journal, 23(11):1684-1692, 1985.

[56] F. R. Menter: *Performance of popular turbulence models for attached and separated adverse pressure gradient flows*. AIAA Journal, 30(8):2066-2072, 1992.

[57] P. Bradshaw, D. H. Ferriss, and N. P. Atwell: *Calculation of boundary-layer development using the turbulent energy equation*. Journal of Fluid Mechanics, 28(3):593-616, 1967.

[58] D. C. Wilcox: *Reassessment of the scale-determining equation for advanced turbulence models*. AIAA Journal, 26(11):1299-1310, 1988.

[59] W. P. Jones and B. E. Launder: *The prediction of laminarization with a two-equation model of turbulence*. International Journal of Heat and Mass Transfer, 15(2):301-314, 1972.

[60] J. B. Cazalbou, P. R. Spalart, and P. Bradshaw: *On the behavior of two-equation models at the edge of a turbulent region*. Physics of Fluids, 6(5):1797–1804, 1994.

[61] L. P. Ludwig and R. C. Bill: *Gas path sealing in turbine engines*. NASA Technical Memorandum 73890, 1978.

[62] S. L. Dixon and C. A. Hall: *Fluid mechanics and thermodynamics of turbomachinery*. Butterworth-Heinemann, 2013.

[63] M. V. Casey: *Mean line prediction method for estimating the performance characteristic of an axial compressor stage*. IMechE Conference Proceedings, 273-285, 1987.

[64] J. Ortmanns: *Numerical investigation of axial compressor stages with differing degrees of reaction*. ASME Conference Proceedings, Paper No. GT2014-25642, 2014.

[65] S. Giannini: *Numerical Investigation of the effects of the degree of reaction in a low speed axial compressor stage*. Master thesis at the Technical University of Munich, Chair of Turbomachinery and Flight Propulsion, 2020.

[66] I. De Dominicis, A. Šimunović, S. Robens, and V. Gümmer: *Numerical Analysis of the Influence of Near-Endwall Camber Line Distribution on Leakage Losses of Axial Compressor Shrouded Stators*. ISABE, Paper No. 2021-113, 2022.

[67] Simon J. Gallimore, John J. Bolger, Nicholas A. Cumpsty, Mark J. Taylor, Peter I. Wright, and James M.M. Place: *The use of sweep and dihedral in multistage axial flow compressor blading-Part 1: University research and methods development*. Journal of Turbomachinery, 124(4):521-532, 2002.

[68] D. C. Wisler: *Loss reduction in axial-flow compressors through low-speed model testing*. Journal of Engineering for Gas Turbines and Power, 107(2):354-363, 1985.

[69] R. F. Behlke: *The development of a second generation of controlled diffusion airfoils for multistage compressors*. Journal of Turbomachinery, 108(1):32-40, 1986.

[70] X. Wang, S. Wang, and W. Han: *Multi-objective aerodynamic design optimization based on camber line and thickness distribution for a transonic compressor rotor*. ASME Conference Proceedings, Paper No. IMECE2008-66345, pp. 25-32, 2009.

[71] H. Schrapp, D. Fischer, J. Ortmanns, M. Goller, and B. Power: *Numerical investigation of the influence of the camber distribution at the rotor tip on the efficiency at different tip clearances*. CEAS Aeronautical Journal, 6:39–47, 2015.

[72] R. Stiegele: *Numerical Investigation of the Influence of the Camberline Distribution on the Hub Leakage Losses of a Multistage Axial Compressor*. Master thesis at the Technical University of Munich, Chair of Turbomachinery and Flight Propulsion, 2021.

[73] A. Šimunović: *Numerical Study of the Influence of the Camber Line Distribution on the Hub Leakage Losses of a Multistage Axial Compressor with Shrouded Stators*. Master thesis at the Technical University of Munich, Chair of Turbomachinery and Flight Propulsion, 2021.

[74] H. K. Versteeg and W. Malalasekera: *Introduction: Computational Fluid Dynamics The Finite Volume Method*. Pearson Education, 2006.